AD-A127 324 ELECTRON LOSSES FROM THE MAGNETOSPHERE(U) AIR FORCE INST OF TECH WRIGHT-PATTERSON AFB OH SCHOOL OF ENGINEERING R S DEWEY MAR 83 AFIT/GNE/PH/83M-4 1/2

UNCLASSIFIED F/G 8/14 NL

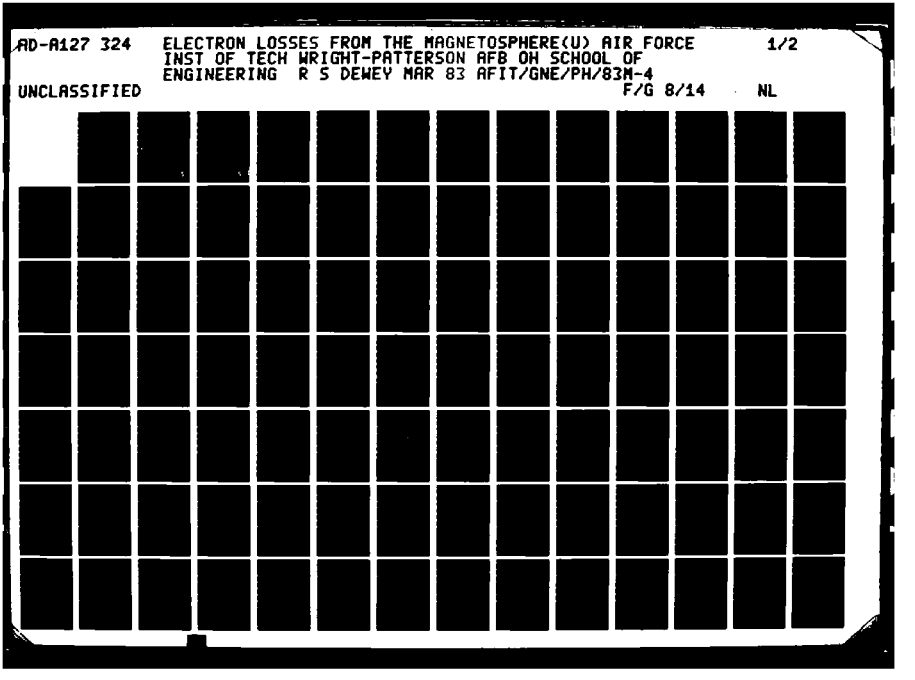

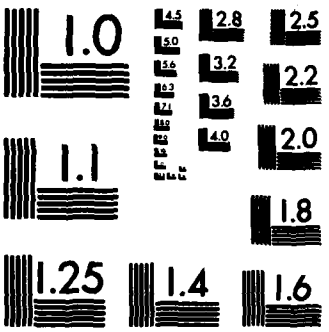

ELECTRON LOSSES FROM THE MAGNETOSPHERE

THESIS

AFIT/GNE/PH/83M-4 Roger S. Dewey
LCDR USN

DEPARTMENT OF THE AIR FORCE
AIR UNIVERSITY (ATC)
AIR FORCE INSTITUTE OF TECHNOLOGY
Wright-Patterson Air Force Base, Ohio

AFIT/GNE/PH/83M-4

ELECTRON LOSSES FROM THE MAGNETOSPHERE

THESIS

AFIT/GNE/PH/83M-4 Roger S. Dewey
LCDR USN

AFIT/GNE/PH/83M-4

ELECTRON LOSSES FROM THE MAGNETOSPHERE

THESIS

Presented to the Faculty of the School of Engineering
of the Air Force Institute of Technology
Air University
in Partial Fulfillment of the
Requirements for the Degree of
Master of Science

by

Roger S. Dewey, B.S.
LCDR USN
Graduate Nuclear Effects
March 1983

Approved for public release; distribution unlimited.

ACKNOWLEDGEMENTS

Dr. Joseph F. Janni of the Air Force Weapons Laboratory sponsored this study. I am greatly indebted to him for his continuing counsel, for his forbearance, and for making available such tremendous computer support at AFWL.

Deserving of special thanks are Mr. Harry Murphy and Mr. John Burgio of AFWL and Miss Cherise Jarrett of Computer Sciences Corporation for their outstanding programming support, without which this study would have been impossible.

A strong debt of gratitude is owed to Tsgt. George Radke of AFWL, whose advice was invaluable, and who kept me mathematically honest.

Particular thanks is also due to my faculty advisors, Majors Robert Davis and James Lange. Their cogent advice and timely direction kept me from going too far astray.

Thanks is extended to Miss Casey Anglada of AFWL and Mrs. Antoinette Aguilar of Tetra Corporation for word-processing the text and equations in final form, and to Mrs. Cindy McDonald for typing a preliminary version of this report in spite of my handwriting.

Finally, I wish to thank my wife, Helen, for her continued encouragement and for putting up with my extended sojourns in Albuquerque.

Roger S. Dewey

CONTENTS

LIST OF FIGURES

LIST OF TABLES

ABSTRACT

A semi-empirical method for modelling the loss of electron fluxes in the earth's magnetosphere was developed. An equation for the integral-energy omnidirectional electron flux as a function of time and magnetic field strength was derived from pitch-angle diffusion theory.

This flux equation was the basis for a computer data-fitting program written at the Air Force Weapons Laboratory (AFWL) to fit the AFWL Trapped Electron Data Base. The program utilized a least-squares fit and incorporated random variations of the characteristic exponential loss times about their initial values. An improved table of initial loss times was compiled for use with the program.

The derived flux model showed substantial agreement with the empirical data base. Representative plots of computed flux over raw data are shown for L-values of 2.3 and 2.4.

I. INTRODUCTION

Objective

Modern technology, both civilian and military, depends greatly on the use of satellite systems. It is thus important to the Department of Defense to understand and predict the environment in which satellites may operate, in order to determine survivability and vulnerability requirements. One part of that environment is the electron fluxes which may exist in the trapping regions of the earth's magnetosphere. Such fluxes may arise from natural sources or from injection by high-altitude nuclear bursts. Because such fluxes have great capability for inflicting damage to sensitive satellite components, even at great distances from a burst, understanding their behavior is vitally important.

There are a large number of theoretical treatments in the literature which describe various electron loss mechanisms from the earth's magnetosphere. However, the empirical calculations of actual electron losses are often conflicting, and frequently are restricted in their areas of coverage.

Since the cessation of high altitude nuclear testing in 1962, loss studies have been limited to electrons injected into the magnetosphere by natural magnetic disturbances such as solar storms. Thus, much of the theory which has been developed since 1962 has had restricted opportunity for empirical testing.

The objective of this study is to produce an improved algorithm to calculate losses of electrons from the magnetosphere. The algorithm is semi-empirical, because it utilizes the Air Force Weapons Laboratory (AFWL) Trapped Electron Data Base (Ref. 37) measurement of electron fluxes (following the old high altitude nuclear bursts) to determine the characteristic loss times of those electrons.

The loss times thus determined and the algorithm for flux "decay" will then be incorporated by AFWL into the SPECTER computer code (Ref. 7-9) for improved flux calculations of satellite environments.

Scope

This study is limited to investigation of one loss mechanism, pitch-angle diffusion, using a theoretical formalism developed principally by Shulz (Ref. 47,48). The study has also been necessarily limited to those regions of space and those energies covered by the satellites from which the data base was complied. The loss equations thus developed in this study are only implicitly functions of energy, E, and L-coordinate (explained in Chapter II).

The sheer volume of data and the limited time for this study also limited the testing of the algorithm developed to a representative subset of the entire data base.

Approach

A specific solution of the pitch-angle diffusion equation is derived using the method proposed by Shulz (Ref. 47). This solution is then fitted to the electron flux data using a least-squares fitting program written by AFWL, with the coordination of this author. The solutions are performed for integral fluxes (above threshold energy of the satellite detector) and for constant L-value. The solutions are thus explicitly functions of magnetic field strength, B, but implicitly functions of E and L .

Use of the AFWL/NTCTS computer facilities was essential to this study. Well over 72 hours of actual computer-processing time were used, and over 1000 computer-produced flux plots were examined.

Presentation

A brief Background section is presented, which covers some physical relations and terminology used in the study of space physics. This section is used to establish uniform symbol notation, and to provide a common starting point for the reader unfamiliar with the specialized language of space physics. It may be skipped by the reader more familiar with the topic.

Chapter III outlines the theory used to develop the flux equations which were fitted to the data.

Following the theory chapter is a chapter outlining the method of data analysis. Descriptions are given of the data base and of the AFWL computer codes used in this study.

Representative results of the study are presented in Chapter V, in both tabular and graphic form. Again, the sheer volume of data makes inclusion of all plots and fitted values prohibitive.

Conclusions and recommendations for improvements for further study are presented in Chapter VI.

The Bibliography includes 65 sources and provides a comprehensive summary of existing literature of relevant topics about radiation trapped in the magnetosphere and of pitch-angle diffusion.

II. BACKGROUND

The equation of motion of a charged particle in magnetic, electric, and external gravitational fields is:

$$m\frac{d^2\vec{r}}{dt^2} = m\vec{g} + q\left(\frac{d\vec{r}}{dt} \times \vec{B}\right) + q\vec{E}$$

where

$\vec{r} = \vec{r}(t, \vec{r}_0, \vec{v}_0)$; $\frac{d\vec{r}}{dt} = \vec{v}$
$m =$ particle mass,
$\vec{g} =$ gravitational constant,
$q =$ charge,
$\vec{B} =$ magnetic field,
$\vec{E} =$ total electric field (Ref. 11:23–24.)

In a uniform magnetic field, a charged particle will move in helical fashion along and around the field lines with a cyclotron radius, ρ_c, (also called gyroradius or Larmor radius) about its "guiding center". The particle's motion may thus be separated into its rotation around the field line and the motion of its center of rotation, or guiding center, along the field line (Ref. 11:24–25).

The period of cyclotron rotation, τ_c, is defined by (Ref. 39:5):

$$\tau_c = \frac{2\pi m}{qB} = \frac{2\pi\rho_c}{v_\perp}$$

where m is the relativistic mass:

$$m = m_0\gamma = m_0\left[\frac{1}{\sqrt{1-(v^2/c^2)}}\right]$$

and where $v_\perp$ is component of velocity perpendicular to $\vec{B}$. The cyclotron frequency is simply 2π over the period (Ref. 39:5):

$$\omega_c = \frac{2\pi}{\tau_c} = \frac{qB}{m}.$$

The angle between a particle's local velocity, $\vec{v}$, and the magnetic field, $\vec{B}$, is its pitch-angle, α, which is defined as:

$$\alpha = \arccos\left(\frac{v_\parallel}{v}\right) = \arcsin\left(\frac{v_\perp}{v}\right).$$

In a uniform static magnetic field, $v_\parallel$ is constant and $v_\perp$ is constant, and hence α is constant. The particle will then move with a uniform circular motion around the field line and uniform rectilinear motion along the field line, resulting in a helical motion about the line, since

$$d\vec{p}/dt = q\vec{v} \times \vec{B} = m\vec{a},$$

and

$$m\vec{a}_\parallel = q(\vec{v} \times \vec{B})_\parallel = 0.$$

$$\vec{a}_{\parallel} = 0,$$
$$v_{\parallel} = \textit{constant},$$

and

$$m\vec{a}_{\perp} = q(\vec{v} \times \vec{B})_{\perp},$$
$$a_{\perp} = (qv_{\perp}B)/m = \textit{constant},$$ which is a constant centripetal acceleration (Ref.39:4-7; Ref. 11:23-36).

The concept of the first adiabatic invariant arises naturally from the guiding center approximation. The ***first adiabatic invariant***, M, (also called the relativistic magnetic moment) is defined by:

$$M = \frac{\vec{p}_{\perp}^{\,2}}{2m_0 B} = \textit{constant}$$

where $\vec{p}_{\perp}$ is the particle's perpendicular momentum in the guiding center approximation. The assumptions implicit in calling M invariant are that the spatial variation of B is small compared to ρ_c and the time variation of B is small compared to τ_c (Ref. 39:11-23).

If a particle has a constant velocity along a field line in the guiding center frame of reference, then

$$\frac{\sin^2\alpha(s)}{B(s)} = \frac{\sin^2\alpha_i}{B_i} = \textit{constant}$$

where s is the arc length along the field line and i is any point on the field line. This assumes that the particle's kinetic energy remains constant as it follows the field line. If a particle enters the field at point B_i with pitch angle α_i, its velocity along the field line is

$$v_{\parallel}(s) = v\cos\alpha(s) = v \bullet \sqrt{1 - \frac{B(s)}{B_i}\sin^2\alpha_i}.$$

If the field is increasing in the direction of $v_{\parallel}$, then the "mirror point" of the particle, where its parallel velocity is zero, is

$$B_m = \frac{B_i}{\sin^2\alpha_i} = \frac{B(s)}{\sin^2\alpha(s)}$$

and the particle has a local pitch angle of 90° at that mirror point (Ref. 39:34-42).

When the magnetic field has a geometry like that of a dipole field, increasing at the poles and decreasing in the midpoint, then the particle is in the so-called "magnetic bottle", and is trapped between the mirror points. There is some minimum B value between the mirror points which is called B_0, the equatorial field strength. Using the guiding center approximation and approximating the earth's magnetic field by a dipole field, a particle trapped in the earth's field has three distinct motions. It circles rapidly about a field line, it bounces along the line between mirror points, and it drifts slowly in longitude around the earth. All three motions take place with different speeds, so they are distinct (Ref. 11:25; Ref. 29:34-65).

From the mirror point definition, and from the velocity equations, we see that

$$M = \frac{p_{\perp}^2}{2m_0 B_m}$$

and that

$$v_{\perp}(s) = v\sin\alpha_i\sqrt{\frac{B(s)}{B_i}} = v\sqrt{\frac{B(s)}{B_m}}.$$

Note that the particle's mirror point depends only on its "injection" point and its injection pitch angle, not on its initial energy or velocity. A mirror point is a consequence of the field alone, and all particles injected at the same point with the same pitch angle will mirror at the same point on the field line. Of course, this is only true if no external forces are acting.

The parallel velocity, $v_\parallel$, of the particle will be the maximun at B_0, where $B(s)$ is the minimum. Thus, a trapped particle spends most of its time near the mirror points, and the least amount of its time transiting the equatorial field regions (Ref. 29:34-44).

The bounce period, τ_b, of a trapped particle is generally much greater than its cyclotron period, τ_c, and is defined by:

$$\tau_b = 2\int_{s_{m_1}}^{s_{m_2}} \frac{ds}{v_\parallel(s)} = \frac{2}{v}\int_{s_{m_1}}^{s_{m_2}} \frac{ds}{\sqrt{1-(B(s)/B_m)}}$$

where s_{m_1} and s_{m_2} are the mirror points on the field line.

As a particle in a dipole field like the earth's bounces along the field line, it also drifts perpendicularly to the field line, due to external forces, field gradients, and field curvature, as well as other effects such as time-dependent field changes. This drift is slow compared to the bounce period. As the particle bounces and drifts, it traces out a surface between its mirror points and around the earth, called a drift shell (Ref. 39:9-19).

The concepts of the second and third adiabatic invariants arise from the above behavior. If the forces acting on the particle remain almost constant over its bounce period, the ***second adiabatic invariant***, J, is defined by

$$J = \oint p_\parallel \, ds = 4\int_0^{s_m} p_\parallel \, ds$$

where $p_\parallel$ is the momentum component parallel to $\vec{B}$ and ds measures arc length from the equator (Ref. 45:12; Ref. 6:3-31). If the forces acting on a particle remain almost constant over its drift period, the ***third adiabatic invariant***, Φ, which is the magnetic flux enclosed by a drift shell, is defined by

$$\Phi = \oint \vec{A}_0 \cdot d\vec{s}$$

where $\vec{A}_0$ is the magnetic vector potential and where the integration is performed over a curve, s, which lies in the drift shell. The third invariant, Φ, is defined and computed for the drift shell of the guiding center, with constant field, and not for a drift shell which a particle may physically trace out under short-term conditions (Ref. 45:12; Ref 39:76-79).

The guiding drift shell of a particle may also be referred to as an "invariant surface," which is composed of field lines which end at the mirror points. The three adiabatic invariants uniquely define an invariant surface (Ref. 6:3-31 to 3-32).

The more common set of parameters used to define a particle's position in the magnetosphere (or to define an invariant surface) is the B-L coordinate system. The B parameter is magnetic field strength, and L is the McIlwain L parameter defined by $L = r_0/R_E$ where R_E is the earth's radius ($\approx$ 6371 km) (Ref. 6:3-33) and (Ref. 39:53).

The value of L, therefore, is equal to the distance, in earth radii, of the equatorial point on a field line in a dipole field. If the field is not symmetric (not a perfect dipole), the invariant surface is not so well defined. However, for most field lines in the trapping

region of the earth's magnetosphere, L varies by less than one percent along the line, so the B-L system is adequate. The less-than-exact symmetry of the earth's dipole field and outside forces may cause particle drift to deviate from a perfect azimuthal course. This means that its L value will vary in the course of a drift period. This variation of L values is not significant below $L \doteq 3$, but may be so above that value. The average L-value of all intersecting invariant surfaces is called an *L-shell*. This L-value defines a set of surfaces along field lines, which may end at differing mirror points. The L-shells are considered to intersect the earth's surface, even though mirror points do not extend through the atmosphere to the surface (Ref. 6:3–33 to 3–35; Ref. 39:53).

The various mechanisms which operate to cause trapped particles to change L-shell or to be lost from the trapping region will necessarily violate one or more of the adiabatic invariants. For example, pitch-angle diffusion violates M or J, or both; and radial diffusion violates Φ (Ref. 45:48). These concepts are discussed further in Chapter III.

III. THEORY

While the motion of particles trapped in a magnetic field is well understood, the mechanisms of losses from magnetic fields such as the earth's magnetosphere are less well understood. It is generally agreed, however, that pitch-angle diffusion into the loss cone is one of the predominant mechanisms for removal of charged particles for mid-range L-values. The loss cone angle is the lower limit of pitch angle for trapped particles. Any particles with smaller pitch angles will mirror in the sensible atmosphere and will be lost by atmospheric scattering.

Roberts (Ref. 41) has noted that a pitch-angle scattering mechanism must be extant for pitch-angle diffusion to occur. Such a mechanism would necessarily violate one or more of the adiabatic invariants.

It is not the purpose of this study to ascertain the true source mechanism of pitch-angle diffusion. Such a study is beyond the scope of this paper. Indeed, the search for this mechanism has been going on for decades. Roberts (Ref. 41) has postulated that the "perturbation forces" causing such diffusion may result from turbulent ambient electric or magnetic fields or from collisions with other trapped or non-trapped particles. Lyons (Refs. 20–28) has formulated extensive theory based on resonant interactions of so-called "whistler" VLF waves with the trapped-particles' gyrofrequencies: "cyclotron-resonance". Regardless of the actual physical mechanism behind pitch-angle diffusion, its general treatment is mathematically the same, and the physical results are the same. (Ref. 41:308) This study follows the methods of Roberts (Ref. 41), Shulz and Lanzerotti (Ref. 45) and Shulz (Ref. 47) in *assuming* that pitch-angle diffusion is an operative process. One of the purposes of this study is the formulation of the equations necessary to validate that assumption against experimental data, and to perform that experimental validation.

It should be emphasized that, while pitch-angle diffusion is assumed in this paper to be the dominant loss mechanism for L-values and altitudes considered, it is not the only loss mechanism. Several investigators have formulated radial diffusion (cross-L) theories (for example, Walt (Ref. 58) or Tomassian (Ref. 54)), coulombic or collision-scattering-diffusion theories (for example, Wentworth (Ref. 60)) and multiple diffusion theories, such as combinations of pitch-angle, energy, and/or radial diffusion (for example, Walt (Ref. 58) and Lyons (Ref. 26)), all of which show some agreement with experimental data. In particular, atmospheric scattering is obviously a dominant force at very low L values (Ref. 30).

The introduction of multiple loss-mechanisms makes explicit solutions of any diffusion equation extremely difficult. To simplify the problem and render it amenable to the method of Shulz (Ref. 47), this study assumes that "as a rule, radial diffusion enables the radiation belts to become populated from an external source (or rearranges particles injected by an internal source), while pitch angle diffusion causes particle loss to an atmospheric sink" (Ref. 45:48).

Pitch-angle diffusion, while simple in concept, is complicated in detail. Roberts' (Ref. 41:307-337) treatment of the general mechanism is particularly descriptive:

At the magnetic equator, a particle's pitch angle, α_0, is determined by

$$(1) \qquad x = \cos\alpha_0 = \frac{P_{\parallel_0}}{\sqrt{(P_{\parallel_0}{}^2 + P_{\perp_0}{}^2)}} = \sqrt{1 - \left(\frac{B_0}{B}\right)}$$

where $P_{\parallel_0}$ and $P_{\perp_0}$ are the parallel and perpendicluar components of the particle's momentum with respect to the field line at the equatorial value of B_0. Roberts next defines

$$W_{\parallel_0} = \frac{P_{\parallel_0}{}^2}{2m_0}, \tag{2}$$

$$W_{\perp_0} = \frac{P_{\perp_0}{}^2}{2m_0}$$

where m_0 is the rest mass. These are defined since the first adiabatic invariant, M, is proportional to $W_{\perp_0}$:

$$M = \frac{W_{\perp_0}}{B_0} \tag{3}$$

and, if $W_{\parallel_0} \ll W_{\perp_0}$, the second adiabatic invariant, J, is approximately proportional to $W_{\parallel_0}$:

$$J \approx \frac{\tau_B W_{\parallel_0}}{\gamma} \tag{4}$$

where

τ_B = the particle's bounce period,

$$\gamma = \frac{\text{relativistic mass}}{\text{rest mass}} = \frac{m}{m_0}.$$

A particle's path may be defined by plotting its values of $W_{\perp_0}$ and $W_{\parallel_0}$ as in Figure 1.

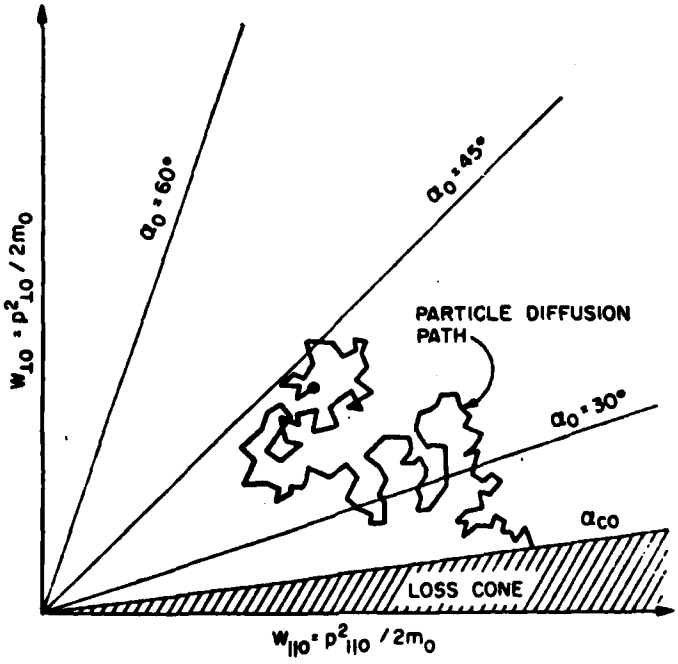

Fig. 1. Loss of a trapped particle by a random walk into the pitch-angle loss cone. (Ref. 41:306)

Note that lines of constant equatorial pitch angle pass through the origin, because

$$\tan^2 \alpha_0 = \frac{W_{\perp_0}}{W_{\parallel_0}}.$$

Any force which violates either M or J, the first or second adiabatic invariant, will produce "diffusion" of the particle's pitch angle as shown in Figure 1 as $W_{\perp_e}$ and $W_{\parallel_e}$ change with time. When a particle's equatorial pitch angle diffuses to the value of the loss cone angle,

$$z_e = \cos \alpha_e = \sqrt{1 - \frac{B_0}{B_{100}}} \tag{5}$$

where B_{100} is the value at 100 km altitude, then it is lost by atmospheric scattering. "The loss cone serves as a 'sink' for particles" undergoing pitch angle diffusion (Ref. 41:307).

Roberts makes two very important points about pitch-angle diffusion as a loss-mechanism:

(1) with no source, the entire radiation-belt would be depleted of particles,

(2) the loss cone approximation is just that, since the atmosphere is not sharply defined at 100 km. However, if *atmospheric* pitch-angle scattering is not the primary focus, the loss come approximation may be useful. "Naturally, when the loss-cone concept is used, detailed agreement between theory and experiment cannot be expected in the region near the edge of the loss cone" (Ref. 41:308).

Both Roberts (Ref. 41) and Shulz and Lanzerotti (Ref. 45) develop the pitch angle diffusion equation from the Fokker-Planck equation using a particle distribution function, $\bar{f}$.

The Fokker-Planck equation is a formalism which arose from the study of Brownian motion, and which is used frequently in transport theory (Ref. 42:308). The characteristic Fokker-Planck equation for trapped particles (which ignores radial diffusion) is:

$$\frac{\partial \bar{f}}{\partial t} = -\frac{1}{\gamma p}\frac{\partial}{\partial E}\left[\gamma p \left(\frac{dE}{dt}\right)_{\nu} \bar{f}\right] + \frac{1}{z\,T(y)}\frac{\partial}{\partial z}\left[z\,T(y)\,D_{zz}\,\frac{\partial \bar{f}}{\partial z}\right]_E + \frac{1}{\gamma p}\frac{\partial}{\partial E}\left[\gamma p\, D_{EE}\,\frac{\partial \bar{f}}{\partial E}\right]_z$$

where the first term, subscripted ν, represents non-stochastic (mean) energy loss to the atmosphere, the second term represents pitch-angle diffusion, and the third term represents range-straggling (energy diffusion). The term $T(y)$ is defined below, and the D_{EE} and D_{zz} terms are the characteristic diffusion coefficients; γ is relativistic mass ratio (Ref. 45:55–58).

Roberts uses a distribution of particles in a "tube" of force about a field line, and Shulz and Lanzerotti use a *phase-space density distribution* function which is essentially equivalent to Roberts'. Since this study follows the methods of Shulz (Ref. 41) and Shulz and Lanzerotti, a discussion of phase space is necessary (Ref. 45:15–22).

Any moving particle can be described by specifying its three position coordinates and its three canonical momentum components. This completes a six-dimension "phase-space" in which a particle can travel in time.

If there exists a system of a large number of particles in phase-space, the system can be described by a six-dimensional distribution function $f(\vec{p}_i, \vec{q}_i, t)$ where

$\vec{p}_i$ $(i = 1, 2, 3)$ are canonical momentum components,
$\vec{q}_i$ $(i = 1, 2, 3)$ are position coordinates, and $\vec{t}$ is time.

Thus, $\int d^3\vec{P}d^3\vec{q}$ is the number of particles instantaneously occupying 6-D volume $d^3\vec{P}d^3\vec{q}$. According to Liouville's theorem, the phase-space volume containing the system of particles moves incompressibly through phase-space.

Since $\vec{P}$ is an awkward quantity to deal with physically, Shulz and Lanzerotti note that $\vec{P}$ transforms to the more familiar $\vec{p}$ as

$$\vec{P} = \vec{p} + \left(\frac{q}{c}\right)\vec{A} \tag{6}$$

where $\vec{A}$ is the electromagnetic vector potential.

Hence, $f(\vec{P},\vec{q},t) = f(\vec{p},\vec{r},t)$ since $\vec{q} = \vec{r}$ and the $\vec{P}$ to $\vec{p}$ transformation has a unit Jacobian. The position-momentum distribution function $f(\vec{p},\vec{r},t)$ defines the particles occupying the 6-D volume $d^3\vec{p}d^3\vec{r}$ at any given t. The pitch angle diffusion equation is given in terms of a phase-space distribution function which is numerically equal to the more easily-definable position-momentum distribution function (Ref. 45:15–22). At constant energy and L-shell, and under the action of some source $\bar{S}$, the diffusion equation in phase-space can be written

$$\frac{\partial \bar{f}}{\partial t} = \frac{1}{x\,T(y)}\frac{\partial}{\partial x}\left[x\,T(y)\,D_{xx}\frac{\partial \bar{f}}{\partial x}\right] + \bar{S} \tag{7}$$

where $T(y)$ is the quarter-bounce integral path length function of $y = \sqrt{1-x^2}$ where $x = \cos\alpha_0$. The quarter bounce integral gives the length of the trajectory of a particle (in units of R_0, the distance to the equatorial crossing) from the equator to the mirror point. The exact definition of T is

$$T = \int_0^{s_m} \frac{ds}{\cos\alpha}$$

where s is the distance along the field line and α is the local pitch angle (Ref. 10:4029–4030).

D_{xx} is the bounce-averaged diffusion coefficient as a function of x (Ref. 41 and Ref. 45). The boundary conditions are that $\bar{f} = 0$ at $x = x_c$ (some cutoff value) and $\bar{f}(x = 0)$ is finite.

Shulz and Lanzerotti (Ref. 45:162) rewrite the above as

$$\frac{\partial \bar{f}}{\partial t} = \frac{1}{x}\frac{\partial}{\partial x}\left[x\,D_{xx}\frac{\partial \bar{f}}{\partial x}\right]_E - \frac{x}{y}\,D_{xx}\,\frac{T'(y)}{T(y)}\left[\frac{\partial \bar{f}}{\partial x}\right]_E + \bar{S} \tag{8}$$

and further approximate that the second term is negligible for $x \ll 1$ since $x^2 + y^2 = 1$. If $T(y) \approx T(1)$, the second term disappears and the equation is a diffusion equation in cylindrical coordinates. (These approximations are *not* used in this work. This development is used to aid in understanding the exact solutions which follow from Shulz (Ref. 47)). If D_{xx} and $\bar{S}$ are then independent of x, and if $\bar{f}(x,t) = X(x)\,T(t)$, the eigenfunctions of (8) are Bessel functions of order zero. The general solution to (8) would then be

$$\bar{f}(x,t) = \bar{f}_\infty(x) + \sum_n a_n(t)\,J_0\left(\kappa_n\frac{x}{x_c}\right) \tag{9}$$

where $\bar{f}_\infty$ is the steady-state solution

$$\bar{f}_\infty(x) = \left(\frac{\bar{S}\,x_c^2}{4\,D_{xx}}\right)\left[1 - \left(\frac{x}{x_c}\right)^2\right] \tag{10}$$

The κ_n are the zeroes of J_0 ($n = 1, 2, \ldots$) and the $a_n(t)$ vary as $e^{-(t/\tau_n)}$, where $\tau_n = z_c^2/(D^2\kappa_n^2)$. Thus, the pitch angle distribution (and hence the directional or omnidirectional flux) is shown to be the sum of a steady state and higher order eigenmodes (Ref. 45:160–168).

The steady state can be thought of as the "normal" or "quiet-time" value of flux which exists in equilibrium with the source $\bar{S}$. An "injection" of particles would then result in a perturbed distribution function with several eigenmodes, each with a characteristic decay-time τ_n. The higher order modes decay faster, and eventually only the fundamental mode would remain, which would decay exponentially to reach the steady state (after "infinite" time) (Ref. 41 and 45). There is ample evidence that such a process does indeed occur. Roberts (Ref. 41) cites Explorer XV data for the 28 October 1962 Russian explosion as an example. Rosen and Sanders (Ref. 43) also note that decay is faster immediately after solar magnetic storm activity than during quieter periods. The similarities in Figures 2 and 3 illustrate the way in which a decay of higher eigenmodes (Figure 2) can approximate the temporal evaluation of an actual electron distribution (Figure 3).

The primary difficulties with the above discussion arise from the approximations that:

(1) $T(y) = T(1) = constant$
(2) $z^2 \ll 1$ (*or* $y \approx 1$)
(3) D_{zz} varies little (or not at all) with z.

Roberts (Ref. 41:311) uses the argument that the full spiral path (and hence $T(y)$) varies only by a factor of 1.4 as z varies from 0 to 0.9 and by 1.9 as z varies from 0 to 1. Shulz and Lanzerotti (Ref. 45:163) use the simplifying assumptions that $T(y) \equiv T(1)$ and D_{zz} is *independent* of z. Both use the assumption that $z^2 \ll 1$.

The present study *requires* that z be allowed to vary from 0 to z_c (up to near 1) in order to adequately examine the AFWL trapped electron data base (Ref. 37). In addition, if z is not small, the approximation that $T(y) \equiv T(1)$ is a poor one, since y is not close to 1.

The function $T(y)$ can be shown, within 0.57% to be approximated as (Ref. 10:4030)

$$T(y) \approx T(0) - [T(0) - T(1)]y^{3/4} \tag{11}$$

where $T(0) = 1 + \left[\left(\ln(2+\sqrt{3})\right)/\left(2\sqrt{3}\right)\right] \approx 1.3802$ and $T(1) = \left(\pi\sqrt{2}\right)/8 \approx 0.7405$ (Ref. 45:19).

Obviously, if z approaches 1, y approaches 0 and the $T(y) \equiv T(1)$ approximation becomes invalid.

The three limiting approximations are removed in the treatment of Shulz (Ref. 47) by introduction of a new "canonical" variable z such that:

$$z = Z(y) = \int_0^z z'\,T(y')\,dz' = \int_y^1 y'\,T(y')\,dy' \tag{12}$$

and a corresponding diffusion coefficient

$$D_{zz} = [z\,T(y)]^2\,D_{zz}. \tag{13}$$

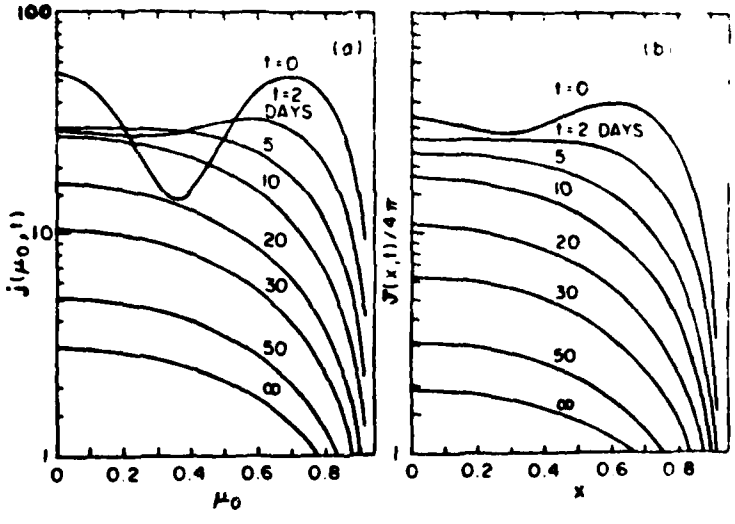

Figure 2. Postulated Decay of Higher Flux Eigenmodes to the Steady State by Pitch-Angle Diffusion (Ref. 41:313).

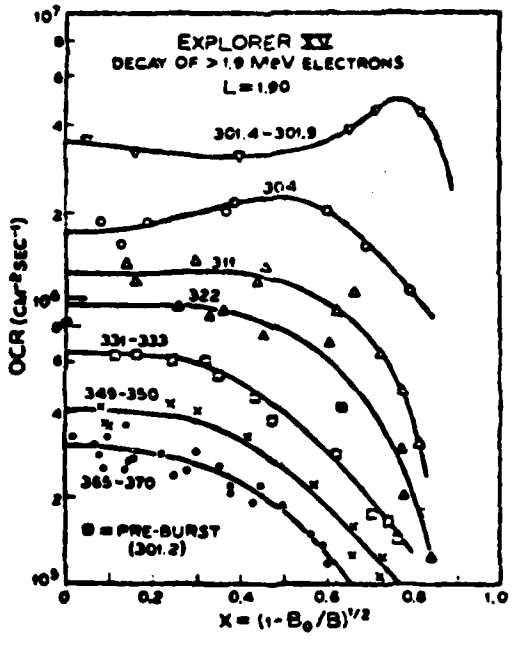

Figure 3. Temporal evolution of 1.9 Mev Electrons from the Russian 3 Burst (Ref. 41:319).

Using (11) in (12) and performing the integration:

$$z \approx \int_y^1 y' \left[T(0) - [T(0) - T(1)] y'^{3/4} \right] dy'$$

$$\approx \int_y^1 \left[T(0) y' - [T(0) - T(1)] y'^{7/4} \right] dy'$$

$$\approx \frac{1}{2} T(0) y'^2 - \frac{4}{11} [T(0) - T(1)] y'^{11/4} \Big|_y^1$$

$$z \approx \frac{T(0)(1 - y^2)}{2} - \frac{4[T(0) - T(1)][1 - y^{11/4}]}{11} \tag{14}$$

where $Z(0) = 16/35$ and $Z(1) = 0$ (Ref. 46:5213).

Using (7), (12) and (13), the diffusion equation becomes:

$$\frac{\partial \bar{f}}{\partial t} = \frac{\partial}{\partial z} \left[D_{zz} \frac{\partial \bar{f}}{\partial z} \right] + \bar{S}. \tag{15}$$

Shulz (Ref. 47:6) states that (15) is a "canonical" diffusion equation in that there is no Jacobian factor which fails to commute with D_{zz} as was the case in (7).

The assumptions which now must be made are:

(1) D_{zz} is some "suitably simple function of z" (Ref. 47:6) so that *exact* eigenfunctions $g_n(z)$ may be specified,

(2) $\bar{S}$, the distributed natural environment source, is independent of z.

Assumption (1) is the limiting assumption, since if the function of z is very complex, the diffusion equation becomes extremely difficult to solve. Assumption (2) is both simple and reasonable, however. The source of the natural environment must be close to constant in order to be the "driver" of quiet-time equilibrium. It must also be distributed fairly closely to the steady-state quiet time distribution for the same reason.

Shulz (Ref. 47:7) states that even if D_{zz} is not of a functional form to yield exact eigenfunctions, there may be a $\hat{D}_{zz}$ which resembles D_{zz} "closely enough" and for which exact eigenfunctions $\hat{g}_n(z)$ (resembling $g_n(z)$) are known.

The following derivation of the exact eigenfunctions and the corresponding omnidirectional differential-energy flux arises directly from Shulz (Ref. 47).

The first assumption by Shulz is that

$$D_{zz} = \left(\frac{z}{z_e} \right)^\sigma D_{zz_e} \tag{16}$$

where σ is some number, not necessarily an integer, less than 2, and where D_{zz_e} is the value of D_{zz} at some $z_e < 16/35$ where f vanishes. Roberts (1969) also uses this assumption.

This form of D_{zz} allows a basis set of orthogonal eigenfunctions to be shown for the interval of interest: $0 \leq z \leq z_e$. Following the notation above, we seek some D_{zz} and

eigenfunctions $g_n(z)$ which "closely resemble" the true functions and which satisfy

$$\frac{d}{dz}\left[\bar{D}_{zz}\frac{d\bar{g}_n(z)}{dz}\right]+\bar{\lambda}_n\bar{g}_n(z)=0 \tag{17}$$

for

$$\bar{D}_{zz}=\left(\frac{z}{z_c}\right)^{\sigma}\bar{D}_{zz_c}$$

with the substitution

$$\bar{g}_n(z) = z^{\alpha}w(\beta z^{\xi})$$

where

$$\xi = 1-\frac{\sigma}{2},$$

$$\alpha = \frac{1-\sigma}{2}$$

and

$$\beta=\sqrt{\frac{\bar{\lambda}_n z_c{}^{\sigma}}{\bar{D}_{zz_c}\xi^2}}$$

then (17) becomes Bessel's equation. The exact eigenfunctions of (17) are given by

$$\bar{g}_n(z)=\frac{\sqrt{\frac{2-\sigma}{z_c}}}{J_{\nu}'(\kappa_{\nu n})}\left(\frac{z}{z_c}\right)^{(1-\sigma)/2}J_{\nu}\left(\kappa_{\nu n}\left(\frac{z}{z_c}\right)^{(1-(\sigma/2))}\right) \tag{18}$$

where $\kappa_{\nu n}$ are the nth zeroes of the Bessel function J_{ν} of the order ν, where

$$\nu = \frac{\sigma-1}{2-\sigma}.$$

The $\bar{g}_n$ given by (18) are normalized so that

$$\int_0^{z_c} g_n\, g_m\, dz = \delta_{nm}. \tag{18 a}$$

The eigenvalues of (18) are given by

$$\bar{\lambda}_n=\left(\frac{\kappa_{\nu n}}{2z_c}\right)^2(2-\sigma)^2\,\bar{D}_{zz_c}. \tag{19}$$

Shulz and Boucher (Ref. 48:6) state that, since particles are not lost at $z = 0$ (but rather at $z = z_c$), the diffusion current must go to zero at $z = 0$. A diffusion current at $z = 0$ would imply diffusion of pitch angles (and hence mirror points) *into* the equator, which is not reasonable. The condition of no diffusion current at $z = 0$ corresponds to $\lim_{z\to 0} D_{zz}\,\bar{g}_n'(z) = 0$.

Shulz and Boucher (Ref. 48) use the series expansion of J_{ν} from Abramowic: and Stegun (Ref. 1) to show the limit as z approaches zero. This author shows the limit directly for the special case eigenfunction $(J_{-1/2})$ which is used in this report. The derivation is shown in Appendix A.

In order to arrive at the differential-energy omnidirectional flux, Shulz (Ref. 47) assumes that $\bar{f}(x,t) \rightarrow \bar{f}_\infty(z)$ as $t \rightarrow \infty$; that is, the solution distribution function has some steady-state value. This also assumes that $\bar{S}$ is constant *in time*, but not in x or z. The $\bar{f}_\infty$ distribution is necessary in order to expand $\bar{f}$ as a series of eigenfunctions in the flux equation. To arrive at an expression for $\bar{f}_\infty$ we start by setting $\partial \bar{f}/\partial t$ to zero in (15) and integrating twice, which gives:

$$\bar{f}_\infty(z) = \int_z^{z_e} \frac{1}{D_{z'z'}} \int_0^{z'} \bar{S}(z'')\, dz''\, dz'. \tag{20}$$

Expanding $\bar{S}$ as a series of orthogonal eigenfunctions gives:

$$\bar{S}(z'') = \sum_{n=0}^{\infty} a_n\, \bar{g}_n(z'') \tag{20a}$$

and using orthogonality (18a) with (20a) gives:

$$a_m = \int_0^{z_e} \bar{S}(z''')\, \bar{g}_m(z''')\, dz'''. \tag{20b}$$

Substituting (20a) into (20) gives

$$\bar{f}_\infty(z) = \int_z^{z_e} \frac{1}{D_{z'z'}} \int_0^{z'} \sum_{n=0}^{\infty} a_n\, \bar{g}_n(z'')\, dz''\, dz'. \tag{20c}$$

Rearranging the order of summation and integration in (20c) gives:

$$\bar{f}_\infty(z) = \sum_{n=0}^{\infty} a_n \int_z^{z_e} \frac{1}{D_{z'z'}} \int_0^{z'} \bar{g}_n(z'')\, dz''\, dz'. \tag{20d}$$

Now integrating (17a) twice gives:

$$\bar{g}_n(z) = \int_z^{z_e} \frac{1}{D_{z'z'}} \int_0^{z'} \bar{\lambda}_n\, \bar{g}_n(z'')\, dz''\, dz'$$

or since $\bar{\lambda}_n$ is a constant,

$$\frac{\bar{g}_n(z)}{\bar{\lambda}_n} = \int_z^{z_e} \frac{1}{D_{z'z'}} \int_0^{z'} \bar{g}_n(z'')\, dz''\, dz'. \tag{20e}$$

Substitution of (20e) into (20d) gives:

$$\bar{f}_\infty(z) = \sum_{n=0}^{\infty} a_n \frac{\bar{g}_n(z)}{\bar{\lambda}_n}. \tag{20f}$$

Substitution of (20b) into (20f) gives:

$$\bar{f}_\infty(z) = \sum_{n=0}^{\infty} \frac{\bar{g}_n(z)}{\bar{\lambda}_n} \int_0^{z_e} \bar{S}(z')\, \bar{g}_n(z')\, dz' \tag{21}$$

where $\bar{S}(z')$ is positive (hence a source).

Shulz and Lanzerotti (Ref. 45:39–40) point out that the *directional* flux $j(E;\vec{r}) = p^2 f(p_\parallel, p_\perp; \vec{r})$ where f is the same distribution function as in this paper. Shulz (Ref. 47)

points out that j must be integrated over all angles in the unit sphere in p-space to obtain the *omnidirectional* flux J:

$$J = 4\pi p^2 \int_0^{\cos\alpha_c} \bar{j}\, d(\cos\alpha). \tag{22}$$

Since

$$\frac{\sin^2\alpha}{B} = \frac{\sin^2\alpha_0}{B_0}$$

and

$$y^2 = \sin^2\alpha\left(\frac{B_0}{B}\right),$$

it follows that

$$\cos\alpha = \sqrt{1 - y^2\left(\frac{B}{B_0}\right)}$$

and that

$$d(\cos\alpha) = \frac{-\frac{1}{2}(B/B_0)\, d(y^2)}{\sqrt{1 - y^2(B/B_0)}}.$$

Now since

$$\cos^2\alpha = 1 - \frac{B}{B_0}(1 - z^2) = 1 - \frac{B}{B_0}(y^2)$$

if $\cos\alpha = \cos\alpha_c$, $y^2 = y_c^2$; if $\cos\alpha = 0$, $y^2 = B_0/B$ and (22) becomes

$$J = 4\pi p^2 \int_{(B_c/B)}^{y_c^2} \frac{-\frac{1}{2}(B/B_0)\, \bar{j}\, d(y^2)}{\sqrt{1 - y^2(B/B_0)}}$$

which, upon combining terms and reversing the limits (-):

$$J = 2\pi p^2 \int_{y_c^2}^{(B_c/B)} \frac{(B/B_0)\, \bar{j}\, d(y^2)}{\sqrt{1 - y^2(B/B_0)}}. \tag{23}$$

Integrating (23) by parts

$$\int u\, dv = uv - \int v\, du \quad \text{where } u = \bar{j}$$

$$dv = \frac{(B/B_0)\, d(y^2)}{\sqrt{1 - y^2(B/B_0)}},$$

$$v = -2\sqrt{1 - y^2\left(\frac{B}{B_0}\right)}$$

gives:

$$2\pi p^2\left[-2\sqrt{1 - y^2\left(\frac{B}{B_0}\right)}\,\bar{j}\,\Bigg|_{y_c^2}^{(B_c/B)} + \int_{y_c^2}^{(B_c/B)} 2\sqrt{1 - y^2\left(\frac{B}{B_0}\right)}\,\frac{\partial\bar{j}}{\partial(y^2)}\, d(y^2)\right]$$

and since

$$\frac{\partial\bar{j}}{\partial(y^2)} = \frac{\partial\bar{j}}{\partial z}\,\frac{\partial z}{\partial(y^2)}$$

will give (since the definite integral evaluates to zero, because $\bar{f}$ is 0 at y_c by definition):

$$J = +2\pi p^2 \int_{y_c^2}^{(B_0/B)} 2\sqrt{1 - y^2\left(\frac{B_0}{B}\right)}\,\frac{\partial f}{\partial z}\,\frac{\partial z}{\partial (y^2)}\,d(y^2). \tag{24}$$

But, from (12), $dz = -y\,T(y)\,dy$. So

$$\frac{dz}{d(y^2)} = \frac{-y\,T(y)\,dy}{d(y^2)} = \frac{-y\,T(y)\,dy}{2y\,dy} = \frac{-T(y)}{2}.$$

Hence, (24) ultimately becomes:

$$J = -2\pi p^2 \int_{y_c^2}^{(B_0/B)} \sqrt{1 - y^2\left(\frac{B}{B_0}\right)}\,T(y)\,\frac{\partial \bar{f}}{\partial z}\,d(y^2). \tag{25}$$

Shulz then expands $\bar{f}$ as a weighted series of eigenfunctions:

$$\bar{f} = \bar{f}_\infty(z) + \sum_{n=0}^{\infty} A_n(E, L; t)\,\bar{g}_n(z). \tag{26}$$

This allows the flux J in (25) to be written:

$$J = 2\pi p^2 \left[-\int_{y_c^2}^{(B_0/B)} \sqrt{1 - y^2\left(\frac{B}{B_0}\right)}\,\bar{f}'_\infty(z)\,T(y)\,d(y^2) - \sum_{n=0}^{\infty} A_n(E, L; t) \int_{y_c^2}^{(B_0/B)} \sqrt{1 - y^2\left(\frac{B}{B_0}\right)}\,T(y)\,\bar{g}'_n(z)\,d(y^2) \right]. \tag{27}$$

The following two expressions are derived in Appendix B.

$$f'_\infty(z) = \sum_{n=0}^{\infty} \frac{\bar{g}'_n(z)}{\bar{\lambda}_n} \int_0^{z_c} \bar{S}\,\bar{g}_n(z')\,d(z'), \tag{28}$$

$$g'_n(z) = \frac{\sqrt{(2-\sigma)/z_c}}{J'_\nu(\kappa_{\nu n})} \left\{ \left(\frac{1-\sigma}{2z_c}\right)\left(\frac{z}{z_c}\right)^{-(\sigma+1)/2} J_\nu\left(\kappa_{\nu n}\left(\frac{z}{z_c}\right)^{1-(\sigma/2)}\right) + \left(\frac{z}{z_c}\right)^{(1-\sigma)/2} J'_\nu\left(\kappa_{\nu n}\left(\frac{z}{z_c}\right)^{1-(\sigma/2)}\right)\left[\frac{\kappa_{\nu n}}{z_c}\left(1 - \frac{\sigma}{2}\right)\left(\frac{z}{z_c}\right)^{-(\sigma/2)}\right] \right\} \tag{29}$$

The actual form of the flux equation awaits the choice of σ, which also determines the dependence of D_{zz} on z. Shulz uses $\sigma = 0$ for purposes of comparison of several computational methods. This choice is also attractive because it makes D_{zz} *independent* of z (see 17(b)) which was a major assumption to begin with:

$$D_{zz} = D_{zz_c}. \tag{30}$$

This choice is made in the present study for the above reasons and also for the sake of simplicity in computations.

With $\sigma = 0$, the Bessel functios within eigenfunctions become order $-1/2$, which can be simply written as:

$$J_{-1/2}(R) = \sqrt{\frac{2}{\pi R}}\,\cos(R), \tag{31}$$

$$J'_{-1/2}(R) = -\sqrt{\frac{2}{\pi R}}\sin(R) - \frac{\cos(R)}{\pi R^2\sqrt{2/(\pi R)}} \tag{32}$$

and the zeroes κ_n occur at $(2n+1)(\pi/2)$.

This simplifies (32), since the second term will always be zero if $J'_{-1/2}(\kappa_n)$ is evaluated at $\kappa_n = (2n+1)(\pi/2)$.

Equation (32) becomes

$$J'_{-1/2}(\kappa_n) = -\sqrt{\frac{2}{\pi(2n+1)(\pi/2)}}\,\sin\left((2n+1)\frac{\pi}{2}\right)$$

$$J'_{-\frac{1}{2}}(\kappa_n) = \sqrt{\frac{2}{\pi(2n+1)(\pi/2)}}\,(-1)^{n+1}. \tag{33}$$

The integral with respect to z' within (28) would thus be evaluated as:

$$\int_0^{z_c} \frac{\sqrt{2/z_c}\,\sqrt{z'/z_c}\,\sqrt{\frac{2}{\pi(2n+1)(\pi/2)(z'/z_c)}}}{-\sqrt{\frac{2}{\pi(2n+1)(\pi/2)}}\,\sin\left((2n+1)\frac{\pi}{2}\right)}\,\cos\left((2n+1)\,\frac{\pi}{2z_c}\,z'\right)dz'$$

$$= \int_0^{z_c} \frac{\sqrt{2/z_c}\,\cos\left((2n+1)(\pi/2z_c)\,z'\right)dz'}{-\sin\left((2n+1)(\pi/2)\right)}$$

$$= \frac{\sqrt{2/z_c}\,\sin\left((2n+1)(\pi/2)(z/z_c)\right)}{((2n+1)(\pi/2z_c))(-1)^{n+1}}\Bigg|_0^{z_c}$$

$$= \frac{\sqrt{2/z_c}\,\sin\left((2n+1)(\pi/2)\right)}{((2n+1)(\pi/2z_c))(-1)^{n+1}}. \tag{34}$$

The $\bar{\lambda}_n$ in (28) would be evaluated as (from (19)):

$$\bar{\lambda}_n = (2n+1)^2\left(\frac{\pi}{2z_c}\right)^2 \bar{D}_{zz_c}. \tag{35}$$

The flux equation (27), using (31), (33), (34), and (35), will then simplify to the following for $\sigma = 0$:

$$(36)\qquad J = 2\pi p^2 \left\{ \left[-\int_{y_c^2}^{(B_0/B)} \sum_{n=0}^{\infty} \frac{\tilde{S}\sqrt{(2/z_c)}\sin((2n+1)(\pi/2))}{(2n+1)(\pi/2z_c)(-1)^{n+1}} \right.\right.$$

$$\cdot \frac{\sqrt{2/z_c}}{\sqrt{\frac{2}{\pi(2n+1)(\pi/2)}}(-1)^{n+1}} \left\{ \left(\frac{1}{2z_c}\right)\left(\frac{z}{z_c}\right)^{-\frac{1}{2}} \sqrt{\frac{2}{\pi(2n+1)(\pi/2)(z/z_c)}} \cos\left((2n-1)\frac{\pi}{2}\frac{z}{z_c}\right) \right.$$

$$+\sqrt{\frac{z}{z_c}}\left(-\sqrt{\frac{2}{\pi(2n+1)(\pi/2)(z/z_c)}}\sin\left((2n+1)\frac{\pi}{2}\frac{z}{z_c}\right)\right.$$

$$\left.\left.-\frac{\cos((2n+1)(\pi/2)(z/z_c))}{\pi((2n+1)(\pi/2)(z/z_c))^2\sqrt{\frac{2}{\pi(2n+1)(\pi/2)(z/z_c)}}}\right)\right.$$

$$\left.\cdot\frac{(2n+1)(\pi/2)}{z_c}\right\}\sqrt{1-y^2\left(\frac{B}{B_0}\right)}\,T(y)\,d(y^2)\left.\right]$$

$$-\left[\sum_{n=0}^{\infty}A_n(E.L;t)\int_{y_c^2}^{(B_0/B)}\frac{\sqrt{(2/z_c)}}{\sqrt{2/(\pi(2n+1)(\pi/2))}\,(-1)^{n+1}}\right.$$

$$\cdot\left[\frac{1}{2z_c}\left(\frac{z}{z_c}\right)^{1/2}\sqrt{\frac{2}{\pi(2n+1)(\pi/2)(z/z_c)}}\cos\left((2n+1)\frac{\pi}{2}\frac{z}{z_c}\right)\right.$$

$$+\sqrt{\frac{z}{z_c}}\left(-\sin\left((2n+1)\frac{\pi}{2}\frac{z}{z_c}\right)\sqrt{\frac{2}{\pi(2n+1)(\pi/2)(z/z_c)}}\right.$$

$$\left.\left.-\frac{\cos((2n+1)(\pi/2)(z/z_c))}{\pi((2n+1)(\pi/2)(z/z_c))^2\sqrt{2/(\pi(2n+1)(z/z_c))}}\right)\right.$$

$$\left.\left.\cdot\frac{(2n+1)(\pi/2)}{z_c}\right]\sqrt{1-y^2\left(\frac{B}{B_0}\right)}\,T(y)\,d(y^2)\right]\right\}.$$

Equation (36) reduces to the following upon simplification and cancellation of terms:

$$(37)\qquad J = 2\pi p^2\left(\left[\int_{y_c^2}^{(B_0/B)}\sum_{n=0}^{\infty}\frac{\tilde{S}(2/z_c)\sin((2n+1)(\pi/2)(z/z_c))}{\tilde{D}_{zz_c}(2n+1)^2(\pi/2z_c)^2(-1)^n}\cdot\sqrt{1-y^2\left(\frac{B}{B_0}\right)}\,T(y)\,d(y^2)\right]\right.$$

$$-\left[\sum_{n=0}^{\infty}\frac{A_n(E,L;t)}{(-1)^n}\int_{y_c^2}^{(B_0/B)}\sqrt{\frac{2}{z_c}}\sin\left((2n+1)\frac{\pi}{2}\frac{z}{z_c}\right)\left((2n+1)\frac{\pi}{2z_c}\right)\right.$$

$$\left.\left.\cdot\sqrt{1-y^2\left(\frac{B}{B_0}\right)}\,T(y)\,d(y^2)\right]\right).$$

The first term in Equation (37) represents a steady state value of the flux, and the second term represents a sum of eigenmodes. Each A_n (Ref. 45:162) has the form $a_n(L)e^{-t/(\tau_n(E))}$. As n increases, the τ_n's become shorter; i.e., the higher eignmodes decay faster, so that eventually only the fundamental mode is left, which decays exponentially. At $t = \infty$, the fundamental mode has reached zero, and only the flux remaining is the steady state flux, which corresponds to the natural environment background.

The remaining substitutions in (37) are z_c, z, $T(y)$, and y_c:

$$
\begin{aligned}
y_c &= \sqrt{\frac{1}{L^3\sqrt{4-(3/L)}}}, \\
z &= Z(y) = \frac{1}{2}(1-y^2)T(0) - \frac{4}{11}[T(0)-T(1)]\left(1-y^{(11/4)}\right), \\
z_c &= Z(y_c) = \frac{1}{2}(1-y_c{}^2)T(0) - \frac{4}{11}[T(0)-T(1)]\left(1-y_c{}^{(11/4)}\right)
\end{aligned}
\tag{38}
$$

(as shown in Equation (14)) T(y) is given by Equation (11).

The variable of integration in (37) is taken as y rather than y^2 for simplicity of integration.

The preceeding derivation has explicitly followed Shulz (1981). However, Shulz did not show how the differential-energy flux related to the integral-energy flux. Shulz and Lanzerotti (Ref. 45:163) state that the integral flux "will then scale as" the differential flux, without derivation. Since the AFWL trapped electron data base (Ref. 37) exists primarily as omnidirectional fluxes integrated over broad energy bandpass, the relation must be derived.

It will be shown in the following and Lanzerotti (Ref. 45) are indeed correct: The differential-energy flux equation (37) will scale as the integral flux, and the energy dependence will be imbedded in the constants for the source and the eigenmodes.

From Roederer (Ref. 39:86), the integral energy omnidirectional flux can be written:

$$
J_{>E} = \int_E^\infty J\, dE \tag{39}
$$

where J is the differential-energy flux, as in the previous equations, and $J_{>E}$ is the integral energy flux above threshold energy E.

A principal assumption will be that energy and pitch angle are both independent variables of the flux. Thus, (26) would really look like

$$
\vec{J}(z,E) = \vec{J}_{\infty_1}(E)\ \vec{J}_{\infty_2}(z) + \sum_{n=0}^{\infty} A_n(E,L;t)\,\vec{y}_n(z) \tag{39 a}
$$

and hence in (25) $\partial\vec{J}/\partial z$ would look like

$$
\frac{\partial \vec{J}}{\partial z} = \vec{J}_{\infty_1}(E)\ \vec{J}'_{\infty_2}(z) + \sum_{n=0}^{\infty} A_n(E,L;t)\,\vec{y}'_n(z). \tag{39 b}
$$

Using (27), (39a) and (39b), Equation (39) becomes, at a given L-shell:

(40)

$$J_{>E} = -2\pi\int_E^\infty p^2 \bar{J}_{\infty_1}(E)\,dE \int_{z_1}^{z_2} \bar{J}'_{\infty_2}(z)\,dz - 2\pi\sum_{n=0}^{\infty}\int_E^\infty p^2\,dE\,A_{n_L}(E)\int_{z_1}^{z_2}\bar{g}'_n(z)\,dz$$

where $\bar{J}'_{\infty_2}(z)$ and $\bar{g}'_n(z)$ represent all of the angular-dependent functions of x, y, or z shown in (25) through (27).

Using the previously stated assumption (Ref. 45:162–163) that $A_{n_L}(E)$ are of the form $a_n(E)e^{-t/(\tau_n(E))}$, 40) becomes:

$$J_{>E} = -2\pi\int_E^\infty p^2\bar{J}_{\infty_1}(E)\,dE\int_{z_1}^{z_2}\bar{J}_{\infty_2}(z)\,dz$$

(41)

$$- 2\pi\sum_{n=0}^{\infty}\int_E^\infty p^2 a_n(E)e^{-t/(\tau_n(E))}\,dE\int_{z_1}^{z_2}\bar{g}'_n(z)\,dz$$

at a given L-shell.

To "remove" the energy dependence of the decay-time terms, the expectation value of $e^{-t/(\tau_n)}$ is computed, assuming that the second term in (41) represents a distribution-function of the energies.

(42)

$$\left\langle e^{-t/(\tau_n)}\right\rangle \approx \frac{\int_E^\infty p^2 a_n(E)e^{-t/(\tau_n(E))}\,dE}{\int_E^\infty p^2 a_n(E)\,dE}$$

Then (41) can be written, using (42):

$$J_{>E} = 2\pi\left[-\int_E^\infty p^2\bar{J}_{\infty_1}(E)\,dE\right]_L\int_{z_1}^{z_2}\bar{J}'_{\infty_2}(z)\,dz$$

(43)

$$- 2\pi\sum_{n=0}^{\infty}\left[\int_E^\infty p^2 a_n(E)\,dE\right]_L\left\langle e^{-t/(\tau_n)}\right\rangle_L\int_{z_1}^{z_2}\bar{g}'_n(z)\,dz.$$

Now since it is assumed that the energy and angular shape functions are separable, the $\bar{J}_{\infty_1}(E)$ must include only those parts of (28) which have energy dependence. The only terms in (28) which could have any energy dependence are $\bar{S}$ and $\bar{\lambda}_n$.

Shulz (Ref. 47:23) notes that, while $\bar{J}_\infty(z)$ resembles $g_0(z)$ in functional form, $\bar{J}_\infty(z)$ will coincide exactly with $g_0(z)$ only if $\bar{S}$ is directly proportional to $g_0(z)$. For simplicity, the assumption is made in this study that $\bar{S}$ is constant over the interval $0 \le z \le z_c$. In physical terms, this really corresponds to a steady-state isotropic source. It is known that the natural environment is not isotropic over either space or time, but the variations are generally small compared to the variations from an injection by a nuclear event.

Now if $\bar{S}$ and $\bar{\lambda}_n$ are the only terms in (28) which may have energy dependence, then $\bar{J}_{\infty_1}(E)$ in (43) would correspond to

$$\sum_{n=0}^{\infty}\frac{\bar{S}(E)}{\bar{\lambda}_n(E)},$$

and since the only portion of the $\bar{\lambda}_n$ which may have any energy dependence (from (19)) is $\bar{D}_{zz_c}$, then $\bar{J}_{\infty_1}(E)$ should be proportional to

$$\frac{\bar{S}(E)}{\bar{D}_{zz_c}(E)},$$

where $\bar{D}_{\alpha\alpha_0}(E)$ may be a constant in E. There may, of course, be some other functional energy-dependence included in $\bar{J}_{\infty_1}(E)$ which is yet-undetermined.

Equation (43) is generally of the same functional form as equation (37) if the terms in square brackets in (43) correspond to the combined constant terms in (37) as demonstrated above and as shown in Appendix D. Equation (43) also bears out Shulz and Lanzerotti's (Ref. 45:163) prediction that the integral flux scales with the differential flux; i.e., the "pitch-angle shape" dependence is invariant for differential- or integral-energy fluxes.

Since it is impractical to evaluate an infinite number of terms in (37), only the terms up to $n = 3$ will be shown. Shulz and Lanzerotti (Ref. 45:163) state that the higher modes vanish for $n > 2$. This in fact means that the higher modes decay so rapidly that modes higher that $n = 3$ should not be seen except at very early times. The final form of Equation (43), taken to $n = 3$, is shown in Appendix C. This is the form of the flux equation used in the data analysis, except that fewer terms were used than are shown in Appendix C.

The general solution for the differential-energy flux (which, from (43), is directly proportional to the integral-energy flux), using Bessel functions of arbitrary order and with σ-dependence explicitly shown, is given in Appendix D.

IV. ANALYSIS OF DATA

The AFWL Trapped Electron Data Base consists of a set of computer tapes of satellite counting data which have been assembled from historical archives (such as the National Space Sciences Data Center, NSSDC) (Ref. 37). The data cover injections of electrons from nine high-altitude nuclear detonations shown in Table I (Ref. 6:6-2).

The Data Base has been organized by Pfitzer into a coherent set of tapes which present, by satellite, net electron omnidirectional integral-energy (above threshold) fluxes as a function of time, B, and L-shell. The computed errors for each data point, in units of flux, are also given. The background which was subtracted to give net flux is also given (Ref. 37:11, 188–189).

Additional data have been collected by AFWL from plots published in early literature. These plots have been photographically enlarged, and the data points digitized and placed in computer files with formats similar to the Pfitzer data (Ref. 12:670–671, Ref. 31:646–468, Ref. 38:637–638).

The satellites which provided the data, and their orbital parameters, are shown in Table II (Ref. 44:41–45).

The analysis of the data base required development of three computer programs by personnel at AFWL, in coordination with this author:

(1) "Program DTABASE" to read raw data, organize it for processing, and output it into uniformly formatted files (Ref. 15).

(2) A program to plot the raw data and to plot flux curves generated by the fitting program.

(3) "Program Electrofit", a fitting program to take data points from DTABASE at a given L-shell and energy and to fit them with the theoretical model developed in this study. It also generates flux curves using the fitted functions at predetermined times to compare with the raw data (Ref. 34).

The first two programs were written with limited input from the author. The third was written under close and extensive coordination with this author, as discussed in this chapter.

The DTABASE program, written by Miss Cherise Jarrett of Computer Sciences Corporation, reads the raw data files, in various formats created by Pfitzer (Ref. 37), satellite by satellite, and stores them in a three-dimensional array. The points are then ordered (within each energy group) by increasing time since burst. To generate a file of points at a specified L-value, each data point L-value is compared to the desired L and is recorded in the output file if a match occurs. Additional points are "created" by linear interpolation of two successive data points if they fall on both sides of the desired L and if the data points differ in time by no more than a specified value. The interpolation is performed in L, B, time, flux, and error. The output file can be restricted to a specified time "window" and to a specified range of B values, if desired; however, the data were analyzed over the full range of B and over all times which existed in the Data Base. The program has the additional capability to "B-average" data points at the same L if their individual B values are within a user specified limit of each other and they are within the required time difference. This procedure has the effect of eliminating "double" points, and was used for the majority of this study with a limit of one percent. Another capability of the program is to interpolate to a specified B-value in a manner analogous to the L-interpolation described above; this capability was unused in this study (Ref. 15:1-2).

Table I. High-altitude nuclear detonations.

Event	Altitude (km)	Time (U.T.)	Date	Latitude	Longitude	Approximate L-Value of Detonation	Yield	Characteristics of Band	Approximate Decay Time
Teak	76.8	10:50:05	1 Aug 1958	17°N	169°W	1.12	MT Range	Low Altitude	~few days
Orange	42.97	10:30:08	12 Aug 1958	17°N	169°W	1.12	MT Range	Low Altitude	~1 day
Argus 1	~200	2:30:00	27 Aug 1958	38°S	12°W	1.7	1-2 KT	Narrow Band	0-20 days
Argus 2	~250	3:20:00	30 Aug 1958	50°S	8°W	2.1	1-2 KT	Narrow Band	10-20 days
Argus 3	~500	22:10:00	6 Sept 1958	50°S	10°W	2.0	1-2 KT	Narrow Band	10-20 days
Starfish	400	09:00:029	9 July 1962	16.7°N	190.5°E	1.12	1.4 MT	Wide Distribution	1-2 years
USSR 1	—	03:40:46	22 Oct 1962	—	—	~1.8	—	Wide Distribution	~30 days
USSR 2	—	04:41:18	28 Oct 1962	—	—	~1.8	—	Wide Distribution	~30 days
USSR 3	—	09:13:	1 Nov 1962	—	—	1.75	—	Narrow Band	~30 days

(Ref. 6-6 2)

TABLE II

Satellites and Their Orbital Parameters

Name	Launch Date	Failure Date	Decay Date	Period (min.)	Perigee (mi.)	Apogee (mi.)	Incl. (deg.)
Alouette 1	9-28-62	unk.	—	105.4	620	633	80.5
Alpha Upsilon 1	9-1-62	—	10-26-64	94.4	189	413	82.8
Explorer 15	10-27-62	2-9-63	—	312.0	194	10730	18.0
Injun 1	6-29-61	3-6-63	—	103.8	534	631	67.0
Traac	11-15-61	7-62	—	105.6	562	720	32.4
Telstar	7-10-62	2-21-63	—	157.8	593	3503	44.8
Explorer 4	7-26-58	10-6-58	10-23-59	110.1	163	1372	50.1

(Ref. 44:41-45)

In order to determine the optimum time difference to use for interpolation across the desired L-value, the DTABASE program was modified under direction of this author. The program now presents a summary table of the raw data points for each satellite, showing the frequency of occurance of time differences between successive data points from 0.1 minute to 5.0 minutes, by tenths of a minutes. The cumulative percentage of points with a specified time difference or less is also shown. These summaries are presented for the bursts and satellites examined as Tables III through XIII (Ref. 15:67-70). Perusal of these tables showed that the optimum time difference for interpolation was 2.2 minutes, primarily to include the maximum number of points in the Starfish Telstar file. This time difference was used for all data examined in this study.

A final capability of DTABASE is to add data points to a specified L-value file by rounding points in L to the desired value. This procedure assumes that points which are closer to the desired L than some specified limit may be considered to occur at the desired L. Within the errors in satellite measurements, this procedure is reasonable, and in fact appears (by data comparison) to have been used by Roberts (Ref. 41:310), although he does not so explicitly state. This capability exists in the program, but was not used in this study (Ref. 15).

The plotting program was developed by Mr. John Burgio of AFWL to generate all the plots of raw data and fitted curves shown in this report. The program plots raw data points beginning at a specified start time since burst (in days) and covering the time period in a specified time "window" (shown in Figure headings as "TW"). The L-value, equatorial B-value, and B-cutoff values are also shown. If the B-range of points is restricted, the minimum and maximim values of B are shown. The equatorial B value is computed from L by the relation

$$B_0 = \frac{0.308}{L^3}.$$

The B-cutoff value was initially computed by using the dipole formula (Ref. 39:55)

$$y_c = \sqrt{\frac{1}{L^3\sqrt{4-(3/L)}}} = \sqrt{(B_0/B_{cut})}.$$

However, it was later determined that this approximation might be less than optimum; so a table of L-values versus B_{cut} was used and was linearly interpolated across the tabulated L-values to find the B_{cut} value. This table (Table XIV) was prepared by AFWL from the 48-term Jensen-Cain model of the magnetosphere (Ref. 16). It was found that use of Table XIV produced B_{cut} (or y_{cut} or z_{cut}) values more indicative of the global cutoff values. This table was used thereafter in both the plotting program and the fitting program (discussed below). This procedure is reasonable in view of the use of the same Jensen-Cain model to produce the B-L coordinates for the Pfitzer Data Base (Ref. 37).

The plotting program plots flux as a function of $x = \sqrt{1-(B_0/B)}$. It also has the capability to plot flux data points versus time over all values of L and B, or flux versus energy at specified B or L. Next to the satellite name on each plot which has fitted curves is a number in square brackets which corresponds to the serial number of the run of the fitting program which prodeuced the curves.

This author's input to the plotting program was limited to supplying header information and specifying layout and format.

The third program used in data analysis is "Program Electrofit," written by Mr. Harry Murphy of AFWL with the close coordination of this author (Ref. 34). Electrofit is a least-squares fitting program which uses the functions developed by this author (Appendix C)

to fit data points which are output from DTABASE in order to compute the characteristic decay times (τ_n) and linear amplitude constants (a_n). These decay times and constants are determined at the specific energy and L-value which are input with the data.

Table III

COUNTS OF TIME DIFFERENCES BETWEEN NONZERO RAW DATA POINTS
FOR ALL CHANNELS OF SATELLITE(S): TELSTAR
FOR BURST: STARFISH

TIME BIN (MIN)		NO. DELTA TIMES IN BIN	CUMULATIVE PERCENTAGE
0.0	0.1	607	1.4
0.1	0.2	3	1.4
0.2	0.3	7	1.5
0.3	0.4	33	1.5
0.4	0.5	0	1.5
0.5	0.6	22	1.6
0.6	0.7	9	1.6
0.7	0.8	58	1.7
0.8	0.9	2	1.7
0.9	1.0	219	2.3
1.0	1.1	29	2.3
1.1	1.2	4	2.3
1.2	1.3	56	2.5
1.3	1.4	12	2.5
1.4	1.5	15	2.5
1.5	1.6	0	2.5
1.6	1.7	35	2.6
1.7	1.8	11	2.6
1.8	1.9	19	2.7
1.9	2.0	33421	81.4
2.0	2.1	178	81.8
2.1	2.2	26	81.9
2.2	2.3	8	81.9
2.3	2.4	5	81.9
2.4	2.5	1	81.9
2.5	2.6	5	81.9
2.6	2.7	0	81.9
2.7	2.8	2	81.9
2.8	2.9	2	81.9
2.9	3.0	50	82.0
3.0	3.1	6	82.1
3.1	3.2	0	82.1
3.2	3.3	3	82.1
3.3	3.4	1	82.1
3.4	3.5	1	82.1
3.5	3.6	0	82.1
3.6	3.7	2	82.1
3.7	3.8	1	82.1
3.8	3.9	5	82.1
3.9	4.0	1451	85.5
4.0	4.1	5	85.5
4.1	4.2	3	85.5
4.2	4.3	0	85.5
4.3	4.4	0	85.5
4.4	4.5	0	85.5
4.5	4.6	2	85.5
4.6	4.7	6	85.5
4.7	4.8	2	85.5
4.8	4.9	2	85.5
4.9	5.0	23	85.6
5.0<=		6115	100.0

Table IV

COUNTS OF TIME DIFFERENCES BETWEEN NONZERO RAW DATA POINTS
FOR ALL CHANNELS OF SATELLITE(S): EXPLORER4
FOR BURST: ARGUS 1 ,2 ,3

TIME BIN (MIN)		NO. DELTA TIMES IN BIN	CUMULATIVE PERCENTAGE
0.0	0.1	442	63.7
0.1	0.2	133	82.9
0.2	0.3	46	89.5
0.3	0.4	10	90.9
0.4	0.5	8	92.1
0.5	0.6	0	92.1
0.6	0.7	1	92.2
0.7	0.8	1	92.4
0.8	0.9	0	92.4
0.9	1.0	0	92.4
1.0	1.1	0	92.4
1.1	1.2	0	92.4
1.2	1.3	0	92.4
1.3	1.4	0	92.4
1.4	1.5	0	92.4
1.5	1.6	0	92.4
1.6	1.7	0	92.4
1.7	1.8	0	92.4
1.8	1.9	0	92.4
1.9	2.0	0	92.4
2.0	2.1	0	92.4
2.1	2.2	0	92.4
2.2	2.3	0	92.4
2.3	2.4	1	92.5
2.4	2.5	0	92.5
2.5	2.6	0	92.5
2.6	2.7	0	92.5
2.7	2.8	1	92.7
2.8	2.9	1	92.8
2.9	3.0	0	92.8
3.0	3.1	1	92.9
3.1	3.2	1	93.1
3.2	3.3	0	93.1
3.3	3.4	0	93.1
3.4	3.5	0	93.1
3.5	3.6	0	93.1
3.6	3.7	0	93.1
3.7	3.8	0	93.1
3.8	3.9	0	93.1
3.9	4.0	0	93.1
4.0	4.1	0	93.1
4.1	4.2	0	93.1
4.2	4.3	0	93.1
4.3	4.4	0	93.1
4.4	4.5	0	93.1
4.5	4.6	0	93.1
4.6	4.7	0	93.1
4.7	4.8	0	93.1
4.8	4.9	0	93.1
4.9	5.0	0	93.1
5.0<=		48	100.0

Table V

COUNTS OF TIME DIFFERENCES BETWEEN NONZERO RAW DATA POINTS
FOR ALL CHANNELS OF SATELLITE(S): ALLOUETTE1
FOR BURST: RUSSIAN 1

TIME BIN (MIN)		NO. DELTA TIMES IN BIN	CUMULATIVE PERCENTAGE
0.0	0.1	0	0.0
0.1	0.2	3413	72.7
0.2	0.3	0	72.7
0.3	0.4	572	84.8
0.4	0.5	180	88.7
0.5	0.6	15	89.0
0.6	0.7	105	91.2
0.7	0.8	0	91.2
0.8	0.9	46	92.2
0.9	1.0	46	93.2
1.0	1.1	1	93.2
1.1	1.2	5	93.3
1.2	1.3	0	93.3
1.3	1.4	15	93.6
1.4	1.5	4	93.7
1.5	1.6	3	93.8
1.6	1.7	5	93.9
1.7	1.8	0	93.9
1.8	1.9	12	94.1
1.9	2.0	1	94.2
2.0	2.1	1	94.2
2.1	2.2	2	94.2
2.2	2.3	0	94.2
2.3	2.4	2	94.3
2.4	2.5	1	94.3
2.5	2.6	0	94.3
2.6	2.7	3	94.4
2.7	2.8	0	94.4
2.8	2.9	0	94.4
2.9	3.0	0	94.4
3.0	3.1	1	94.4
3.1	3.2	0	94.4
3.2	3.3	0	94.4
3.3	3.4	3	94.4
3.4	3.5	0	94.4
3.5	3.6	0	94.4
3.6	3.7	0	94.4
3.7	3.8	0	94.4
3.8	3.9	1	94.5
3.9	4.0	1	94.5
4.0	4.1	0	94.5
4.1	4.2	3	94.5
4.2	4.3	0	94.5
4.3	4.4	1	94.6
4.4	4.5	0	94.6
4.5	4.6	0	94.6
4.6	4.7	0	94.6
4.7	4.8	0	94.6
4.8	4.9	0	94.6
4.9	5.0	0	94.6
5.0<=		255	100.0

Table VI

COUNTS OF TIME DIFFERENCES BETWEEN NONZERO RAW DATA POINTS
FOR ALL CHANNELS OF SATELLITE(S): EXPLORER15
FOR BURST: RUSSIAN 1

TIME BIN (MIN)		NO. DELTA TIMES IN BIN	CUMULATIVE PERCENTAGE
0.0	0.1	0	0.0
0.1	0.2	0	0.0
0.2	0.3	0	0.0
0.3	0.4	2	1.7
0.4	0.5	12	12.0
0.5	0.6	0	12.0
0.6	0.7	5	16.2
0.7	0.8	6	21.4
0.8	0.9	1	22.2
0.9	1.0	0	22.2
1.0	1.1	13	33.3
1.1	1.2	8	40.2
1.2	1.3	0	40.2
1.3	1.4	1	41.0
1.4	1.5	0	41.0
1.5	1.6	0	41.0
1.6	1.7	11	50.4
1.7	1.8	3	53.0
1.8	1.9	0	53.0
1.9	2.0	0	53.0
2.0	2.1	0	53.0
2.1	2.2	3	55.6
2.2	2.3	4	59.0
2.3	2.4	0	59.0
2.4	2.5	0	59.0
2.5	2.6	0	59.0
2.6	2.7	0	59.0
2.7	2.8	0	59.0
2.8	2.9	1	59.8
2.9	3.0	0	59.8
3.0	3.1	2	61.5
3.1	3.2	0	61.5
3.2	3.3	0	61.5
3.3	3.4	3	64.1
3.4	3.5	7	70.1
3.5	3.6	0	70.1
3.6	3.7	3	72.6
3.7	3.8	0	72.6
3.8	3.9	0	72.6
3.9	4.0	1	73.5
4.0	4.1	0	73.5
4.1	4.2	0	73.5
4.2	4.3	0	73.5
4.3	4.4	0	73.5
4.4	4.5	0	73.5
4.5	4.6	1	74.4
4.6	4.7	0	74.4
4.7	4.8	0	74.4
4.8	4.9	0	74.4
4.9	5.0	0	74.4
5.0<=		30	100.0

Table VII

COUNTS OF TIME DIFFERENCES BETWEEN NONZERO RAW DATA POINTS
FOR ALL CHANNELS OF SATELLITE(S): TELSTAR
FOR BURST: RUSSIAN 1

TIME BIN (MIN)		NO. DELTA TIMES IN BIN	CUMULATIVE PERCENTAGE
0.0	0.1	0	0.0
0.1	0.2	0	0.0
0.2	0.3	0	0.0
0.3	0.4	0	0.0
0.4	0.5	1	0.0
0.5	0.6	0	0.0
0.6	0.7	0	0.0
0.7	0.8	0	0.0
0.8	0.9	0	0.0
0.9	1.0	7	0.2
1.0	1.1	1	0.2
1.1	1.2	0	0.2
1.2	1.3	0	0.2
1.3	1.4	0	0.2
1.4	1.5	0	0.2
1.5	1.6	0	0.2
1.6	1.7	0	0.2
1.7	1.8	1	0.2
1.8	1.9	2	0.3
1.9	2.0	3637	86.6
2.0	2.1	3	86.6
2.1	2.2	3	86.7
2.2	2.3	0	86.7
2.3	2.4	0	86.7
2.4	2.5	0	86.7
2.5	2.6	0	86.7
2.6	2.7	0	86.7
2.7	2.8	0	86.7
2.8	2.9	0	86.7
2.9	3.0	6	86.8
3.0	3.1	0	86.8
3.1	3.2	0	86.8
3.2	3.3	0	86.8
3.3	3.4	0	86.8
3.4	3.5	0	86.8
3.5	3.6	0	86.8
3.6	3.7	0	86.8
3.7	3.8	0	86.8
3.8	3.9	1	86.9
3.9	4.0	134	90.0
4.0	4.1	0	90.0
4.1	4.2	0	90.0
4.2	4.3	0	90.0
4.3	4.4	2	90.1
4.4	4.5	0	90.1
4.5	4.6	0	90.1
4.6	4.7	0	90.1
4.7	4.8	0	90.1
4.8	4.9	0	90.1
4.9	5.0	5	90.2
5.0<=		413	100.0

Table VIII

COUNTS OF TIME DIFFERENCES BETWEEN NONZERO RAW DATA POINTS
FOR ALL CHANNELS OF SATELLITE(S): ALLOUETTE1
FOR BURST: RUSSIAN 2

TIME BIN (MIN)		NO. DELTA TIMES IN BIN	CUMULATIVE PERCENTAGE
0.0	0.1	45	1.1
0.1	0.2	3107	78.9
0.2	0.3	0	78.9
0.3	0.4	409	89.1
0.4	0.5	91	91.4
0.5	0.6	7	91.5
0.6	0.7	52	92.8
0.7	0.8	0	92.8
0.8	0.9	29	93.6
0.9	1.0	25	94.2
1.0	1.1	3	94.3
1.1	1.2	13	94.6
1.2	1.3	0	94.6
1.3	1.4	7	94.8
1.4	1.5	1	94.8
1.5	1.6	0	94.8
1.6	1.7	6	94.9
1.7	1.8	0	94.9
1.8	1.9	4	95.0
1.9	2.0	1	95.1
2.0	2.1	0	95.1
2.1	2.2	4	95.2
2.2	2.3	0	95.2
2.3	2.4	1	95.2
2.4	2.5	3	95.3
2.5	2.6	0	95.3
2.6	2.7	0	95.3
2.7	2.8	0	95.3
2.8	2.9	0	95.3
2.9	3.0	0	95.3
3.0	3.1	0	95.3
3.1	3.2	0	95.3
3.2	3.3	0	95.3
3.3	3.4	0	95.3
3.4	3.5	0	95.3
3.5	3.6	0	95.3
3.6	3.7	0	95.3
3.7	3.8	0	95.3
3.8	3.9	0	95.3
3.9	4.0	0	95.3
4.0	4.1	0	95.3
4.1	4.2	0	95.3
4.2	4.3	0	95.3
4.3	4.4	0	95.3
4.4	4.5	0	95.3
4.5	4.6	0	95.3
4.6	4.7	0	95.3
4.7	4.8	0	95.3
4.8	4.9	0	95.3
4.9	5.0	0	95.3
5.0<=		189	100.0

Table IX

COUNTS OF TIME DIFFERENCES BETWEEN NONZERO RAW DATA POINTS
FOR ALL CHANNELS OF SATELLITE(S): EXPLORER15
FOR BURST: RUSSIAN 2

TIME BIN (MIN)		NO. DELTA TIMES IN BIN	CUMULATIVE PERCENTAGE
0.0	0.1	0	0.0
0.1	0.2	0	0.0
0.2	0.3	0	0.0
0.3	0.4	71	2.9
0.4	0.5	264	13.8
0.5	0.6	344	28.0
0.6	0.7	142	33.9
0.7	0.8	77	37.0
0.8	0.9	31	38.3
0.9	1.0	83	41.7
1.0	1.1	65	44.4
1.1	1.2	68	47.2
1.2	1.3	64	49.9
1.3	1.4	63	52.5
1.4	1.5	115	57.2
1.5	1.6	75	60.3
1.6	1.7	125	65.4
1.7	1.8	36	66.9
1.8	1.9	11	67.4
1.9	2.0	33	68.7
2.0	2.1	12	69.2
2.1	2.2	29	70.4
2.2	2.3	32	71.8
2.3	2.4	17	72.5
2.4	2.5	42	74.2
2.5	2.6	14	74.8
2.6	2.7	26	75.8
2.7	2.8	11	76.3
2.8	2.9	16	76.9
2.9	3.0	10	77.4
3.0	3.1	10	77.8
3.1	3.2	10	78.2
3.2	3.3	7	78.5
3.3	3.4	8	78.8
3.4	3.5	22	79.7
3.5	3.6	23	80.7
3.6	3.7	45	82.5
3.7	3.8	14	83.1
3.8	3.9	18	83.8
3.9	4.0	27	84.9
4.0	4.1	15	85.6
4.1	4.2	10	86.0
4.2	4.3	6	86.2
4.3	4.4	10	86.6
4.4	4.5	4	86.8
4.5	4.6	15	87.4
4.6	4.7	10	87.8
4.7	4.8	4	88.0
4.8	4.9	14	88.6
4.9	5.0	8	88.9
5.0<=		269	100.0

Table X

COUNTS OF TIME DIFFERENCES BETWEEN NONZERO RAW DATA POINTS
FOR ALL CHANNELS OF SATELLITE(S): TELSTAR
FOR BURST: RUSSIAN 2

TIME BIN (MIN)		NO. DELTA TIMES IN BIN	CUMULATIVE PERCENTAGE
0.0	0.1	0	0.0
0.1	0.2	0	0.0
0.2	0.3	0	0.0
0.3	0.4	0	0.0
0.4	0.5	0	0.0
0.5	0.6	0	0.0
0.6	0.7	0	0.0
0.7	0.8	0	0.0
0.8	0.9	0	0.0
0.9	1.0	2	0.1
1.0	1.1	0	0.1
1.1	1.2	0	0.1
1.2	1.3	0	0.1
1.3	1.4	0	0.1
1.4	1.5	0	0.1
1.5	1.6	0	0.1
1.6	1.7	0	0.1
1.7	1.8	1	0.1
1.8	1.9	0	0.1
1.9	2.0	2244	85.6
2.0	2.1	49	87.5
2.1	2.2	1	87.5
2.2	2.3	0	87.5
2.3	2.4	0	87.5
2.4	2.5	0	87.5
2.5	2.6	0	87.5
2.6	2.7	0	87.5
2.7	2.8	0	87.5
2.8	2.9	0	87.5
2.9	3.0	3	87.6
3.0	3.1	0	87.6
3.1	3.2	0	87.6
3.2	3.3	0	87.6
3.3	3.4	0	87.6
3.4	3.5	0	87.6
3.5	3.6	0	87.6
3.6	3.7	0	87.6
3.7	3.8	0	87.6
3.8	3.9	2	87.7
3.9	4.0	100	91.5
4.0	4.1	2	91.6
4.1	4.2	0	91.6
4.2	4.3	0	91.6
4.3	4.4	0	91.6
4.4	4.5	0	91.6
4.5	4.6	0	91.6
4.6	4.7	0	91.6
4.7	4.8	0	91.6
4.8	4.9	0	91.6
4.9	5.0	0	91.6
5.0<=		221	100.0

Table XI

COUNTS OF TIME DIFFERENCES BETWEEN NONZERO RAW DATA POINTS
FOR ALL CHANNELS OF SATELLITE(S): ALLOUETTE1
FOR BURST: RUSSIAN 3

TIME BIN (MIN)		NO. DELTA TIMES IN BIN	CUMULATIVE PERCENTAGE
0.0	0.1	123	0.8
0.1	0.2	10901	74.0
0.2	0.3	45	74.3
0.3	0.4	1595	85.0
0.4	0.5	491	88.3
0.5	0.6	55	88.7
0.6	0.7	289	90.6
0.7	0.8	11	90.7
0.8	0.9	128	91.5
0.9	1.0	74	92.0
1.0	1.1	8	92.1
1.1	1.2	55	92.5
1.2	1.3	3	92.5
1.3	1.4	62	92.9
1.4	1.5	28	93.1
1.5	1.6	9	93.1
1.6	1.7	18	93.3
1.7	1.8	0	93.3
1.8	1.9	18	93.4
1.9	2.0	15	93.5
2.0	2.1	2	93.5
2.1	2.2	10	93.6
2.2	2.3	0	93.6
2.3	2.4	13	93.7
2.4	2.5	7	93.7
2.5	2.6	1	93.7
2.6	2.7	7	93.8
2.7	2.8	0	93.8
2.8	2.9	4	93.8
2.9	3.0	2	93.8
3.0	3.1	2	93.8
3.1	3.2	5	93.8
3.2	3.3	0	93.8
3.3	3.4	2	93.9
3.4	3.5	0	93.9
3.5	3.6	1	93.9
3.6	3.7	1	93.9
3.7	3.8	0	93.9
3.8	3.9	1	93.9
3.9	4.0	0	93.9
4.0	4.1	0	93.9
4.1	4.2	0	93.9
4.2	4.3	0	93 9
4.3	4.4	0	93.9
4.4	4.5	0	93.9
4.5	4.6	1	93 9
4.6	4.7	0	93.9
4.7	4.8	0	93.9
4.8	4.9	0	93 9
4.9	5.0	0	93.9
5.0<=		911	100.0

Table XII

COUNTS OF TIME DIFFERENCES BETWEEN NONZERO RAW DATA POINTS
FOR ALL CHANNELS OF SATELLITE(S): EXPLORER15
FOR BURST: RUSSIAN 3

TIME BIN (MIN)		NO. DELTA TIMES IN BIN	CUMULATIVE PERCENTAGE
0.0	0.1	46	0.3
0.1	0.2	0	0.3
0.2	0.3	77	0.8
0.3	0.4	588	4.8
0.4	0.5	1654	16.0
0.5	0.6	2144	30.5
0.6	0.7	1629	41.5
0.7	0.8	970	48.0
0.8	0.9	274	49.9
0.9	1.0	194	51.2
1.0	1.1	226	52.7
1.1	1.2	210	54.1
1.2	1.3	293	56.1
1.3	1.4	273	58.0
1.4	1.5	474	61.2
1.5	1.6	442	64.1
1.6	1.7	618	68.3
1.7	1.8	313	70.4
1.8	1.9	194	71.7
1.9	2.0	131	72.6
2.0	2.1	82	73.2
2.1	2.2	92	73.8
2.2	2.3	74	74.3
2.3	2.4	54	74.7
2.4	2.5	45	75.0
2.5	2.6	35	75.2
2.6	2.7	53	75.6
2.7	2.8	34	75.8
2.8	2.9	37	76.0
2.9	3.0	40	76.3
3.0	3.1	29	76.5
3.1	3.2	47	76.8
3.2	3.3	52	77.2
3.3	3.4	66	77.6
3.4	3.5	53	78.0
3.5	3.6	79	78.5
3.6	3.7	155	79.6
3.7	3.8	91	80.2
3.8	3.9	127	81.0
3.9	4.0	111	81.8
4.0	4.1	83	82.3
4.1	4.2	117	83.1
4.2	4.3	87	83.7
4.3	4.4	110	84.5
4.4	4.5	73	85.0
4.5	4.6	100	85.6
4.6	4.7	76	86.2
4.7	4.8	63	86.6
4.8	4.9	80	87.1
4.9	5.0	59	87.5
5.0<=		1848	100.0

Table XIII

COUNTS OF TIME DIFFERENCES BETWEEN NONZERO RAW DATA POINTS
FOR ALL CHANNELS OF SATELLITE(S): TELSTAR
FOR BURST: RUSSIAN 3

TIME BIN (MIN)		NO. DELTA TIMES IN BIN	CUMULATIVE PERCENTAGE
0.0	0.1	5	0.0
0.1	0.2	0	0.0
0.2	0.3	0	0.0
0.3	0.4	0	0.0
0.4	0.5	0	0.0
0.5	0.6	0	0.0
0.6	0.7	0	0.0
0.7	0.8	0	0.0
0.8	0.9	1	0.0
0.9	1.0	64	0.3
1.0	1.1	4	0.3
1.1	1.2	2	0.3
1.2	1.3	0	0.3
1.3	1.4	0	0.3
1.4	1.5	1	0.3
1.5	1.6	3	0.3
1.6	1.7	3	0.3
1.7	1.8	6	0.4
1.8	1.9	15	0.4
1.9	2.0	20107	82.9
2.0	2.1	121	83.4
2.1	2.2	7	83.5
2.2	2.3	6	83.5
2.3	2.4	1	83.5
2.4	2.5	0	83.5
2.5	2.6	0	83.5
2.6	2.7	0	83.5
2.7	2.8	0	83.5
2.8	2.9	0	83.5
2.9	3.0	25	83.6
3.0	3.1	1	83.6
3.1	3.2	3	83.6
3.2	3.3	1	83.6
3.3	3.4	0	83.6
3.4	3.5	0	83.6
3.5	3.6	0	83.6
3.6	3.7	3	83.6
3.7	3.8	2	83.6
3.8	3.9	9	83.7
3.9	4.0	1027	87.9
4.0	4.1	5	87.9
4.1	4.2	1	87.9
4.2	4.3	0	87.9
4.3	4.4	3	87.9
4.4	4.5	1	87.9
4.5	4.6	0	87.9
4.6	4.7	0	87.9
4.7	4.8	0	87.9
4.8	4.9	1	87.9
4.9	5.0	12	88.0
5.0<=		2929	100.0

Table XIV
Global Magnetic Cutoff Values

L-Value	B_{cutoff}
1.0949	0.23901
1.1152	.22998
1.1356	.22482
1.1559	.22288
1.1762	.22353
1.2628	.24017
1.4817	.26770
1.8331	.27573
2.3168	.29762
2.9330	.33311
3.6816	.37001
4.5626	.40274
5.5760	.43178
6.7218	.45502
8.0000	.46951

Note: The Table may be interpolated for other L-values (Ref. 16).

The overall flow for the program is as follows (see Appendix E):

(1) Use an initial guess for the fundamental decay time and the theoretical ratios of the higher-mode decay times to compute the starting decay times. The first guess at fundamental decay time is shown in Table XV as a function of L and energy. This table is interpolated in L and E for starting value.

(2) Numerically compute the integrals of the functions shown in Appendix C at each data point using the initial guessed decay times. The integration is performed by a 12-point Gauss/Legendre Quadrature at each data point for each function. Only the fundamental decay mode and two higher modes were computed.

(3) Compute the linear amplitude constants using a least-squares matrix-solving routine. Compute the standard error of the fit. The individual points are weighted by the reciprocal of their fractional errors, which have been normalized to an average value of one.

(4) Optimize the initially computed y_{cut} value by using a "Golden Section Minimim" function. This section attempts to let the data determine the "best" cutoff value. If the data are not distributed down toward the loss cone, the Golden Minimum function will provide an erroneous y_{cut} value. Hence, the function specifies that the computed y_{cut} must be within ± 10 percent of the initial input value. If, in the iteration process, the function tries to exceed these limits, the initial guess of y_{cut} is specified as the correct value.

(5) Repeat the steps (2) and (3) with the optimum y_{cut} value.

(6) To determine the best combination of decay times and amplitude constants, the decay times are changed by a "random-walk" method, either increased or decreased. The amount by which the decay times may randomly vary is determined by using a cumulative normal probability distribution about the initial value.

The standard deviation used was estimated according to this author's best guess of the accuracy of the tables and curves shown by Stassinopoulos (Ref. 53:31–32, 40–44) and West (Ref. 63:50–54). The Stassinopoulos tables do not always correlate with each other or with the Stassinopoulos curves, and the West curves do not always correlate with the Stassinopoulos in the L-regions of overlap. The initial fundamental decay times in Table XV were computed by this author by interpolation of the tables and curves in Reference 53 and by reading and extrapolation of the curves in Reference 63. The author's estimates of their standard deviations are shown in Table XVI. Of particular note is the very low confidence in decay times at high L values (above 2.2) and at high energies (above 2.0 MeV). There have been few computations of decay times in these regions, and the results vary widely (Refs. 53, 63).

The effect of using the cumulative normal probability distribution and the above standard deviations is to restrict the "random-walk" of the decay times away from their initial values. The farther away from the initial "mean value" that the random value generator places the new decay time, the greater the "push" that is created back toward the mean for the next walk. The distance away, however, is defined in terms of the standard deviation, so that τ values in which there is low confidence may vary by larger amounts than may τ values in which there is greater confidence. The τ's are also restricted by the constraint that $\tau_0 > \tau_1 > \tau_2$.

With each change of decay times, steps (2) and (3) are repeated up to 96 times, in an attempt to get a "better" fit by reducing the standard error of the fit.

Table XV

Initial Estimate of Fundamental Decay Time (days)

As a Function of *L*-shell and Energy

L-shell

Energy (Mev)	1.02	1.20	1.22	1.24	1.26	1.28	1.30	1.40	1.50	1.60	1.70	1.80	1.90	2.00	2.10	2.20	2.30	2.40	3.00	3.50	4.50	5.00	6.00
0.1	0.	160.	190.	215.	240.	275.	265.	280.	260.	250.	233.	215.	190.	150.	100.0	58.0	56.0	55.0	24.0	10.0	5.0	3.0	2.8
0.2	0.	175.	210.	240.	260.	295.	305.	325.	312.	295.	270.	245.	217.	180.	110.0	60.0	58.0	56.0	26.0	14.0	6.0	4.0	2.9
0.3	0.	180.	220.	225.	280.	308.	325.	337.	330.	312.	288.	260.	230.	185.	112.0	60.0	58.0	56.0	26.0	16.0	6.0	4.0	3.0
0.4	0.	190.	230.	250.	288.	320.	330.	350.	335.	324.	299.	270.	238.	185.	100.0	50.0	46.0	43.0	14.8	4.2	1.1	1.5	3.2
0.5	0.	195.	230.	250.	290.	325.	337.	360.	350.	330.	307.	275.	240.	170.	92.0	38.0	34.0	30.0	5.0	1.2	1.0	1.7	3.5
0.6	0.	200.	230.	260.	300.	332.	350.	363.	357.	337.	312.	280.	235.	152.	80.0	30.0	18.0	17.5	2.6	1.5	2.6	2.8	5.5
0.7	0.	200.	240.	265.	300.	337.	353.	365.	360.	340.	315.	280.	225.	88.	70.0	25.0	14.0	13.0	2.0	1.6	3.3	4.0	7.1
0.8	0.	210.	240.	270.	300.	337.	353.	370.	363.	340.	318.	275.	200.	120.	57.0	20.0	12.0	8.5	1.3	1.8	4.1	5.3	8.7
0.9	0.	210.	240.	270.	300.	337.	353.	370.	367.	345.	315.	265.	165.	100.	45.0	18.0	11.0	7.8	1.4	2.1	4.3	5.7	8.7
1.0	0.	215.	240.	275.	310.	337.	353.	370.	368.	345.	310.	250.	168.	90.	37.0	16.0	10.0	7.1	1.5	2.5	4.5	6.1	8.8
1.1	0.	220.	240.	275.	310.	337.	353.	370.	366.	340.	300.	225.	148.	75.	29.0	14.0	8.8	6.4	1.6	2.8	4.7	6.5	8.9
1.2	0.	220.	240.	275.	310.	335.	350.	370.	364.	335.	282.	203.	125.	65.	22.0	12.0	7.5	5.7	1.7	3.2	5.0	7.0	9.0
1.3	0.	215.	240.	275.	310.	333.	340.	368.	360.	330.	265.	185.	112.	45.	21.0	12.0	7.3	5.5	2.3	3.7	5.4	7.0	8.6
1.4	0.	215.	240.	275.	310.	330.	337.	363.	357.	320.	255.	170.	95.	42.	20.0	11.0	7.1	5.3	2.9	4.2	5.8	7.0	8.2
1.5	0.	215.	240.	275.	310.	325.	335.	361.	354.	312.	245.	150.	80.	39.	19.0	11.0	7.0	5.1	3.5	4.7	6.2	7.0	7.8
1.6	0.	210.	240.	275.	310.	325.	332.	358.	350.	304.	230.	142.	65.	36.	18.0	11.0	6.8	5.0	4.2	5.3	6.6	7.0	7.5
1.7	0.	210.	240.	275.	305.	325.	330.	355.	340.	290.	220.	125.	50.	35.	18.0	11.0	6.7	4.8	4.8	5.5	7.2	7.6	9.0
1.8	0.	210.	240.	275.	300.	320.	327.	352.	335.	280.	200.	115.	48.	34.	19.0	10.0	6.6	4.7	5.2	5.7	7.8	8.2	11.0
1.9	0.	205.	235.	265.	300.	315.	326.	348.	330.	272.	185.	93.	47.	32.	19.0	10.0	6.5	4.6	5.6	6.0	8.3	9.0	12.5
2.0	0.	200.	230.	265.	300.	312.	325.	345.	325.	265.	175.	80.	45.	30.	18.8	10.4	6.9	5.0	5.7	6.1	8.3	9.0	12.5
2.1	0.	200.	225.	260.	290.	310.	322.	340.	315.	250.	160.	70.	44.	29.	18.6	10.8	7.3	5.5	5.9	6.2	8.3	9.0	12.5
2.2	0.	190.	225.	250.	285.	307.	318.	335.	310.	240.	145.	60.	42.	28.	18.4	11.2	7.7	6.0	6.1	6.3	8.3	9.0	12.5
2.3	0.	180.	220.	250.	280.	303.	315.	330.	300.	233.	130.	58.	41.	27.	18.2	11.6	8.1	6.5	6.2	6.4	8.3	9.0	12.5
2.4	0.	175.	210.	240.	275.	300.	312.	326.	292.	222.	120.	55.	39.	26.	18.0	12.0	8.5	6.9	6.4	6.5	8.3	9.0	12.5
2.5	0.	170.	200.	235.	265.	300.	310.	323.	285.	215.	100.	52.	38.	25.	17.8	12.4	8.9	7.3	6.5	6.6	8.3	9.0	13.0
2.6	0.	165.	190.	225.	250.	282.	305.	320.	276.	200.	93.	50.	36.	24.	17.6	12.8	9.3	7.7	6.7	6.7	8.3	9.0	13.0
2.7	0.	155.	180.	215.	250.	275.	300.	315.	267.	191.	85.	47.	35.	23.	17.4	13.2	9.7	8.1	6.8	6.8	8.3	9.0	13.0
2.8	0.	150.	175.	200.	235.	260.	300.	310.	265.	185.	75.	45.	33.	22.	17.2	13.6	10.0	8.5	6.9	6.9	8.3	9.0	13.0
2.9	0.	140.	165.	190.	225.	250.	285.	305.	258.	174.	65.	42.	32.	21.	17.1	14.0	10.5	8.9	7.1	7.0	8.3	9.0	13.0
3.0	0.	125.	150.	180.	210.	240.	265.	300.	250.	170.	60.	40.	30.	20.	17.0	14.0	11.0	9.3	7.1	7.1	8.3	9.0	13.0

(Computed from Ref. 53 31 32, 40 11 and Ref. 63.50 54)

Table XVI

Percent Standard Deviation of Initial
Fundamental Decay Times (in Table XV)

L-Range	1.02–1.20	1.21–1.40	1.41–1.80	1.81–2.20	> 2.20
Energy Range MeV					
$E \leq 0.6$	50	30	20	35	200
$0.6 < E \leq 2.0$	30	20	20	75	100
$E > 2.0$	50	20	50	100	100

(estimated from Ref. 53:31–32, 40–44 and Ref. 63:50–54)

(7) If a better fit is found in less than 96 random walks, and if less than 32 "better" values have been found, steps (2), (3) and (6) are repeated up to 32 times, using the latest "best" decay times.

(8) Up to five repeats of steps (4) and (5) may be carried out, but only if 32 "better" fits are found. Otherwise, only the first y_{cut} optimization is performed.

(9) The program will always end at the point where 96 random-walks have failed to reduce the error of the fit from the previous "best-fit". The decay times, y_{cut}, and amplitude constants are printed for each "better" fit, with the final values being those of the "best" fit.

(10) After the best fit is found, the program uses the fitted constants and decay times to compute fluxes, at specified times, from the equator to the best cutoff value. These specified times correspond to default times plus 1/2 time window in the program which plots raw data. Thus, the computed fluxes are used to generate curves which are plotted over raw data points at approximately the same times.

Variations in the program were tried in order to study the effects of the fitting process. The principal modifications were in the random decay-time variations.

The first modification was to fix the ratios of the τ's to their theoretical values of 1:1/9:1/25 (Ref. 48:16–19). The effect of this modification is to significantly reduce the degrees of freedom available to fit the data.

The second modification was a compromise between the above and complete freedom to random walk. This variation allowed τ_0 and τ_1 to vary freely (subject to the usual contraint that $\tau_0 > \tau_1$), but τ_1 and τ_2 were fixed at their theoretical ratio of 25:9. The principal reason for this attempt was the very short time-span covered by some satellite/burst combinations. For example, the Russian 2 Burst covered only 4 1/2 days prior to the Russian 3 injection. If the data cover a time-span which is small compared to the fundamental decay constant, then the fitted value of that decay time may be suspect. However, if the time-span is not so small compared to the decay times of the higher modes, one should have more confidence in the fitted values of those decay time. Stated another way, the fit may not be sensitive to the fundamental, but may still be sensitive to the higher modes.

In this analysis, not all L-values covered by the satellite in Table II were examined. Over 1000 plots of flux versus x were examined at various L-values for the satellite/burst combinations of Tables I and II. In many cases, the satellite orbits were of such high inclination (toward polar) that data were not available close to equatorial B-values. Because of this, and because of the very large volume of data, those satellite/burst/L combinations which provided the most consistent coverage from the equator to the loss cone were chosen for study.

Generally, the data fell into three regions of x-space (with some overlap). Region I was from the equator to the point where flux dropped off sharply into the loss cone ($x = 0$ to $x \approx 0.6$ or 0.8). Region II was the area where the flux "turned the corner" from a rather "horizontal" curve to a rather "vertical" curve into the loss cone ($x \approx 0.7$ to 0.9). Region III was the loss cone region, where the flux levels dropped sharply to the cutoff value ($x \approx .9$ for a typical L-value).

Representative plots of raw data in the three regions are shown in Figures 4 through 8. These plots are typical in that data seldom cover all three regions in a short time-span. Gaps in the data appear because of satellite orbital coverage and because of lack of on-satellite recorders. When a satellite lacked a recorder, data were collected only as the satellite passed above the radio horizon of a ground tracking station. Figure 9 is an eight-hour plot of typical satellite coverage over all B-L space.

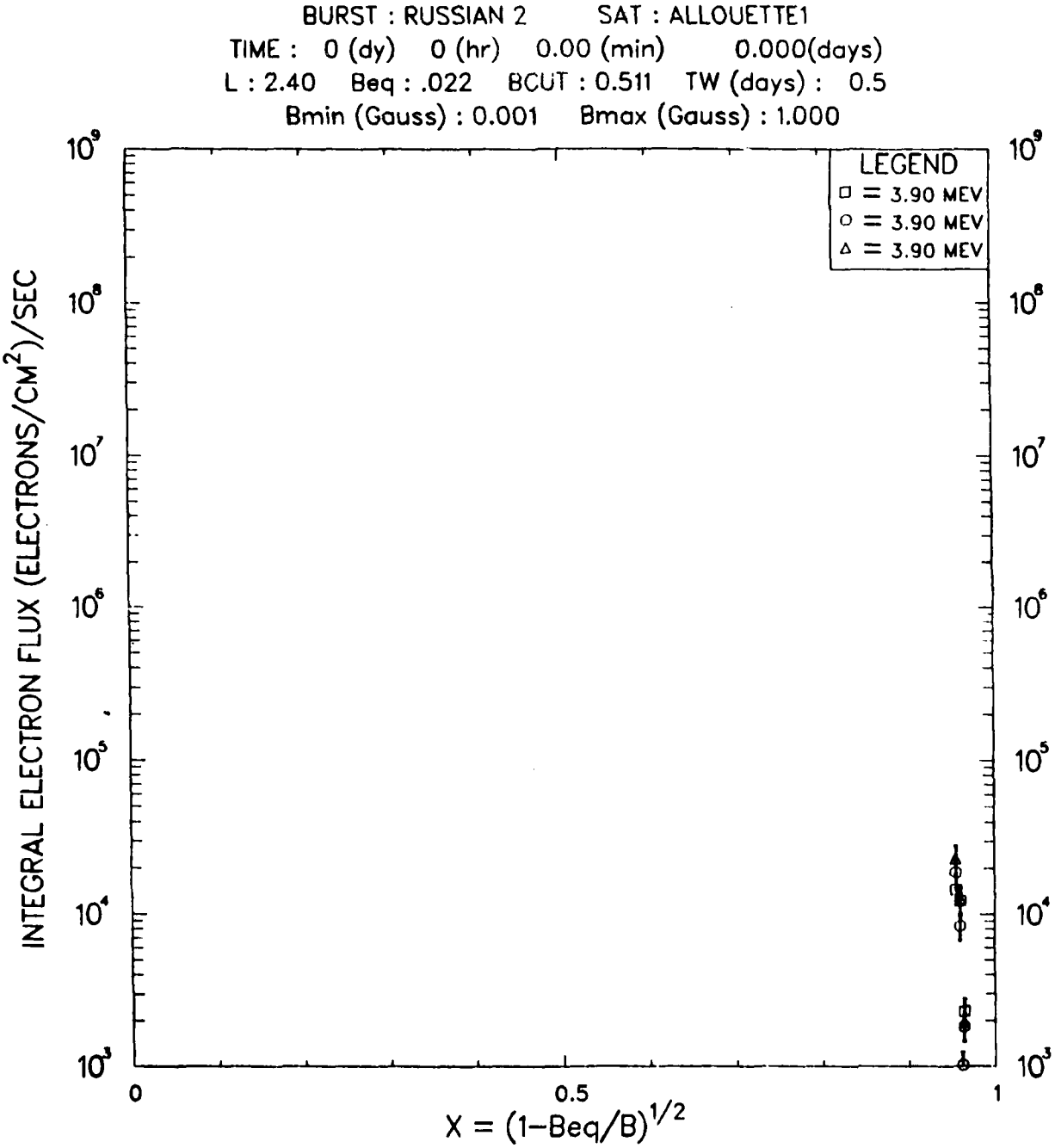

Figure 4(a). Raw Allouette Data Collected Only in Region III (at burst time).

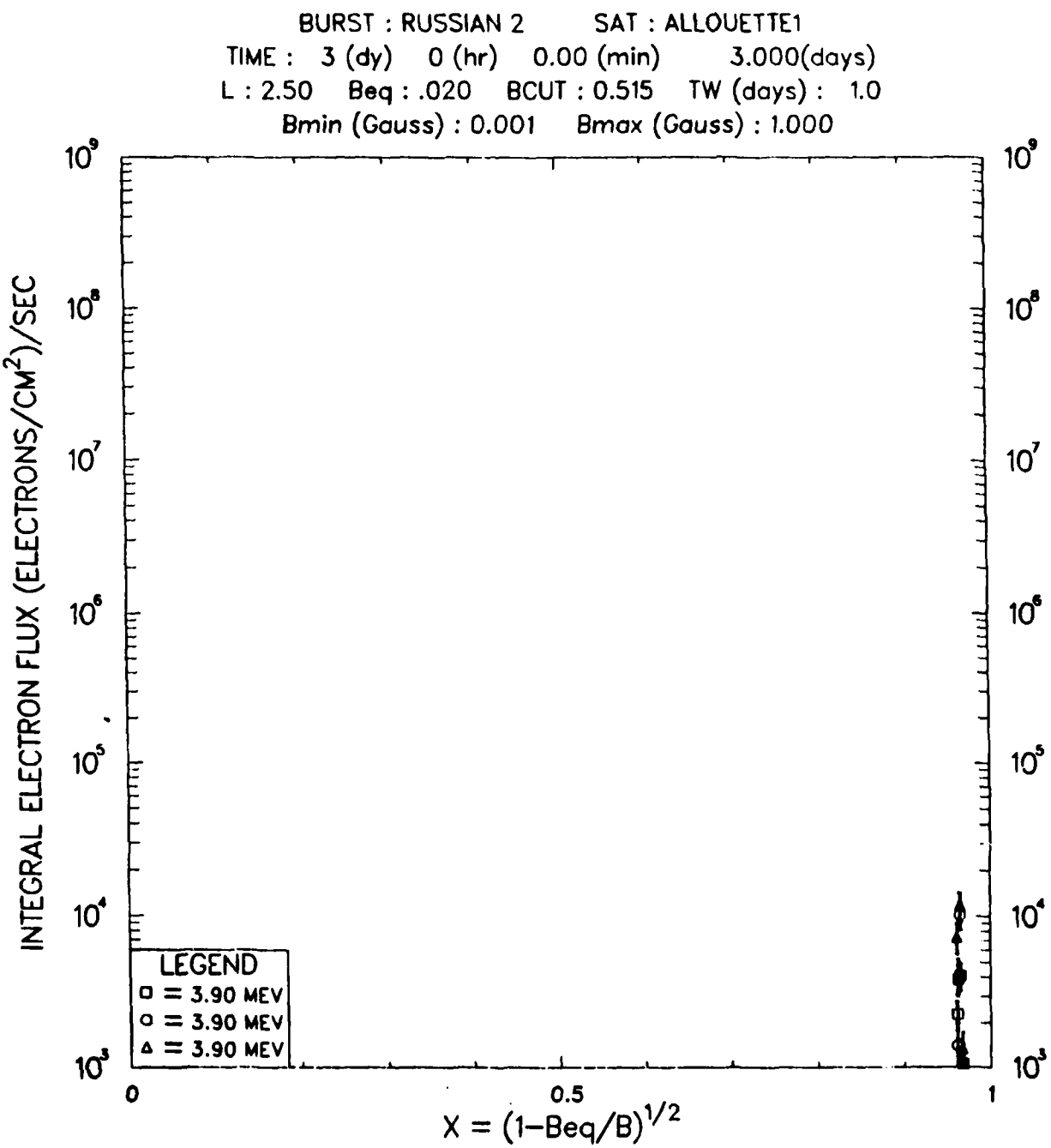

Figure 4(b). Raw Allouette Data Collected Only in Region III (3 days post-burst).

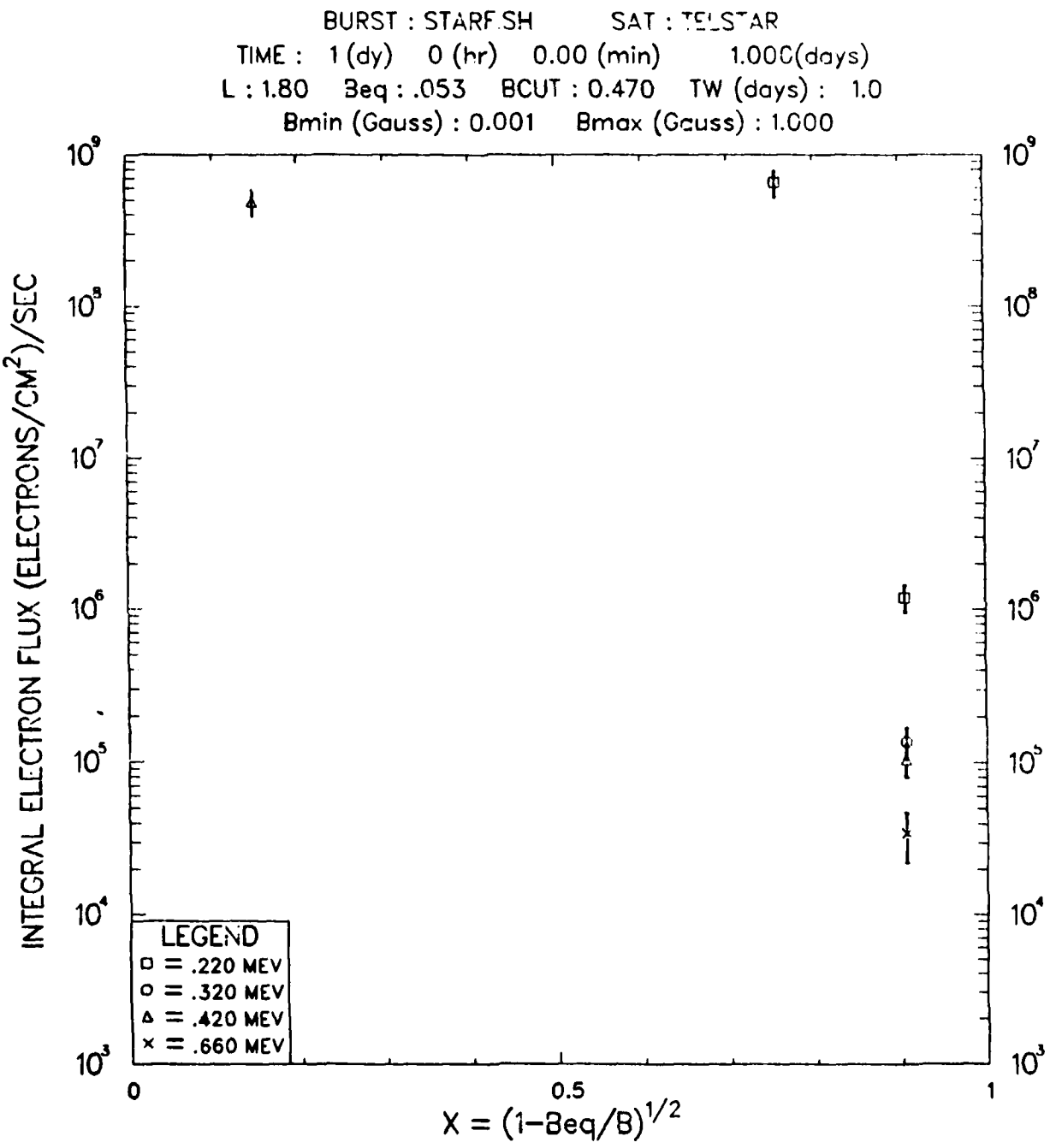

Figure 5. Raw Telstar Data Collected in Regions I and III (early time).

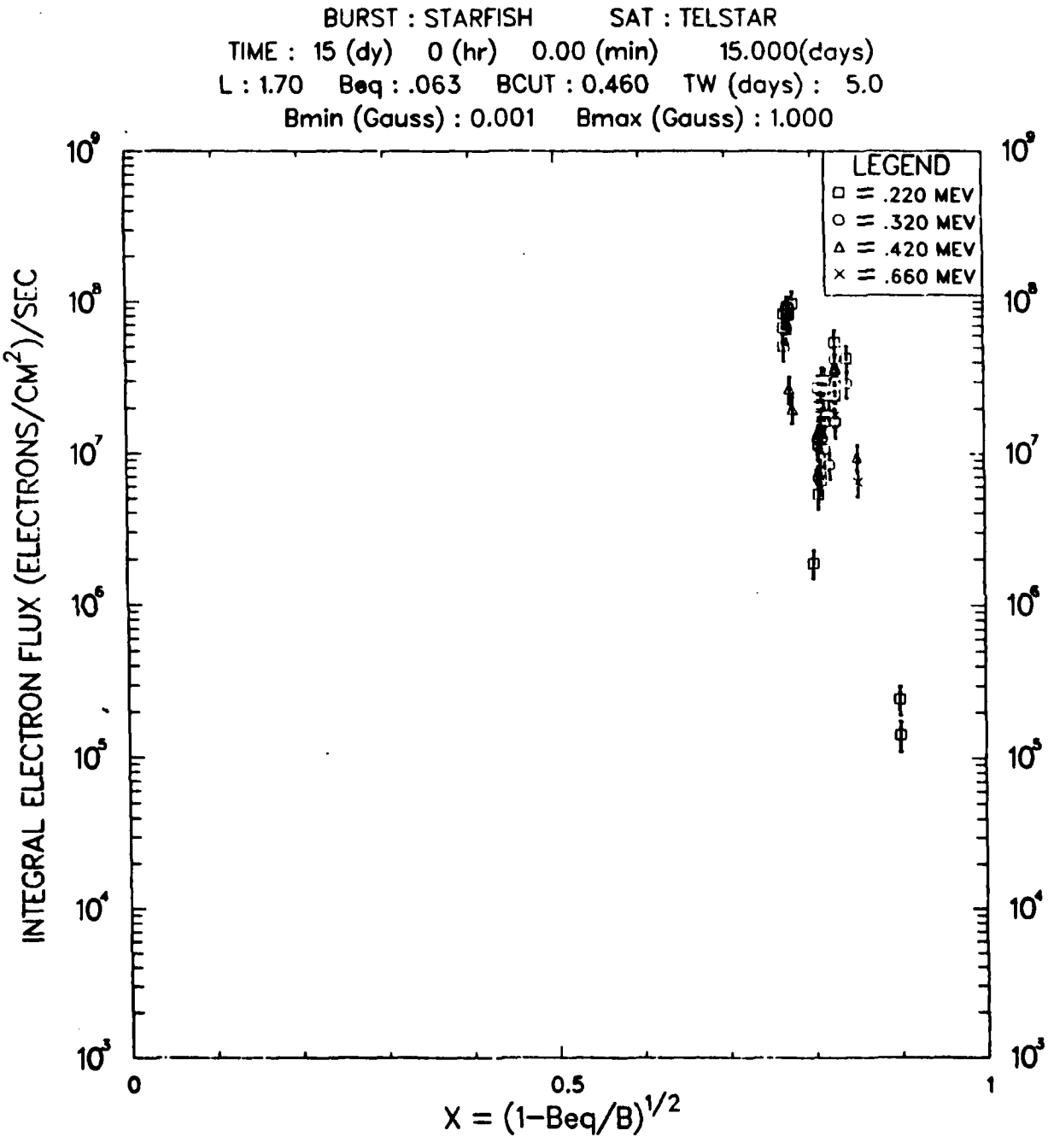

Figure 6. Raw Telstar Data Collected in Region III (mid-range time).

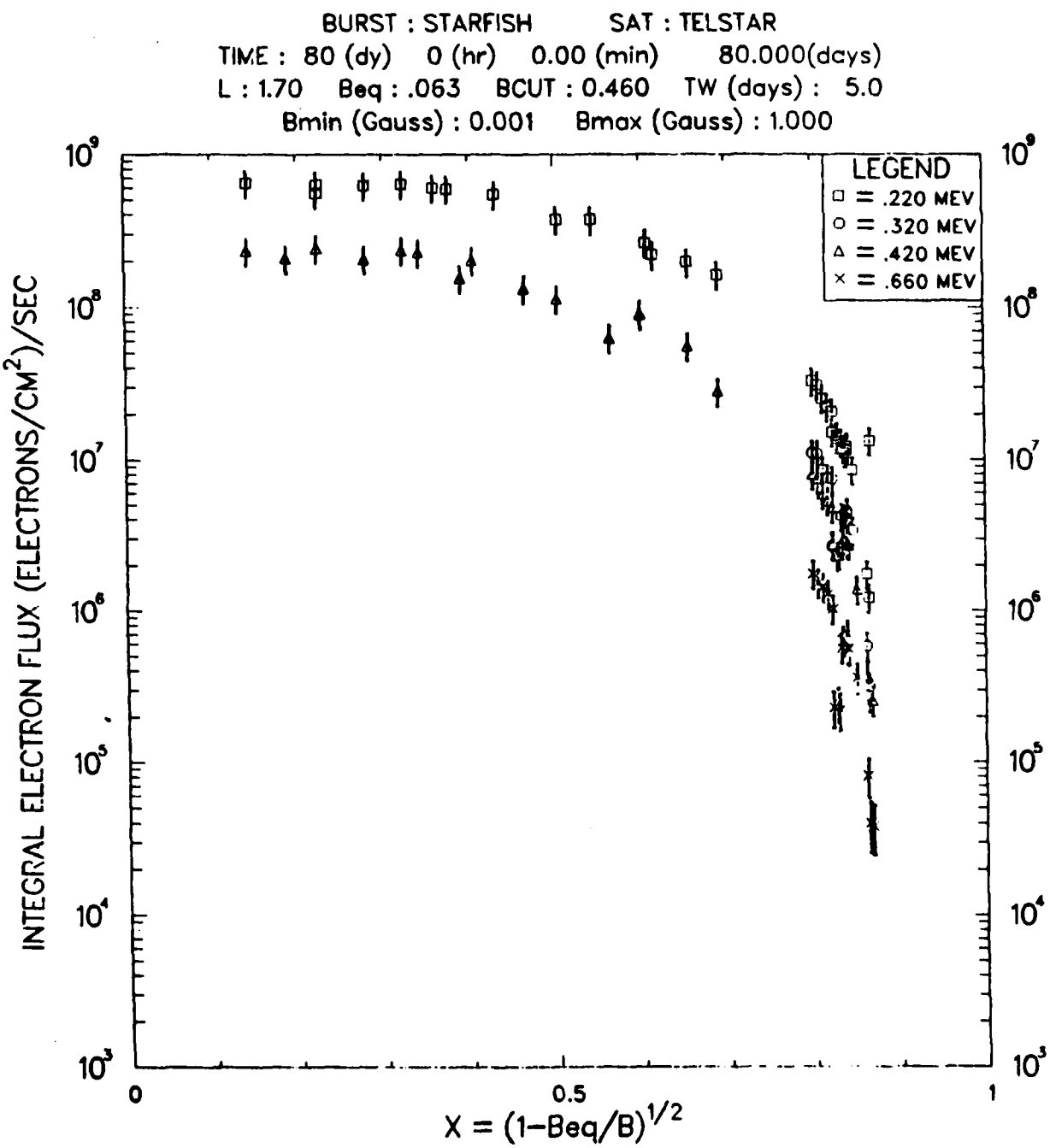

Figure 7. Raw Telstar Data Collected in Regions I, II, and III (mid-range time).

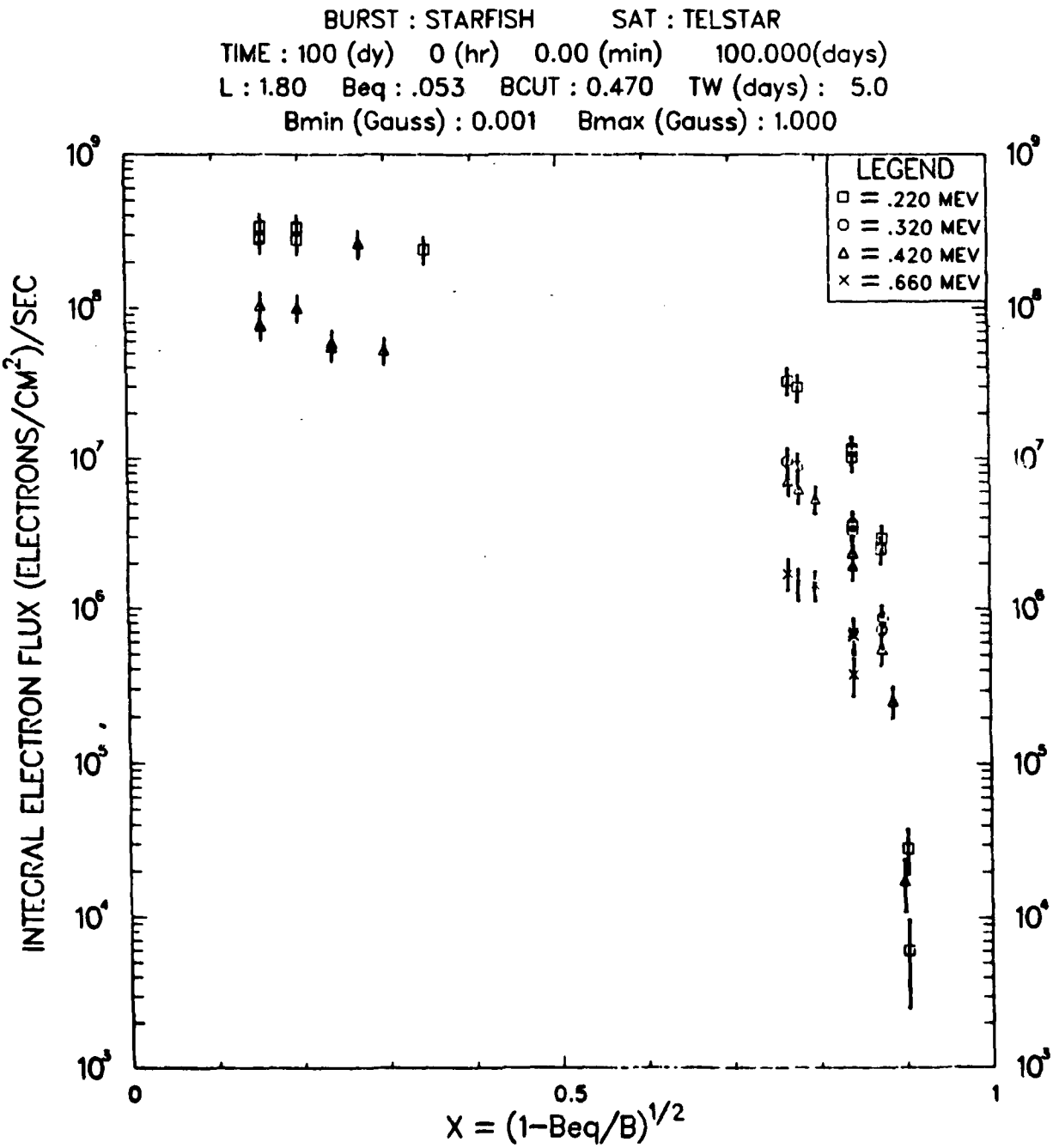

Figure 8(a). Raw Telstar Data in Regions I and II (late time).

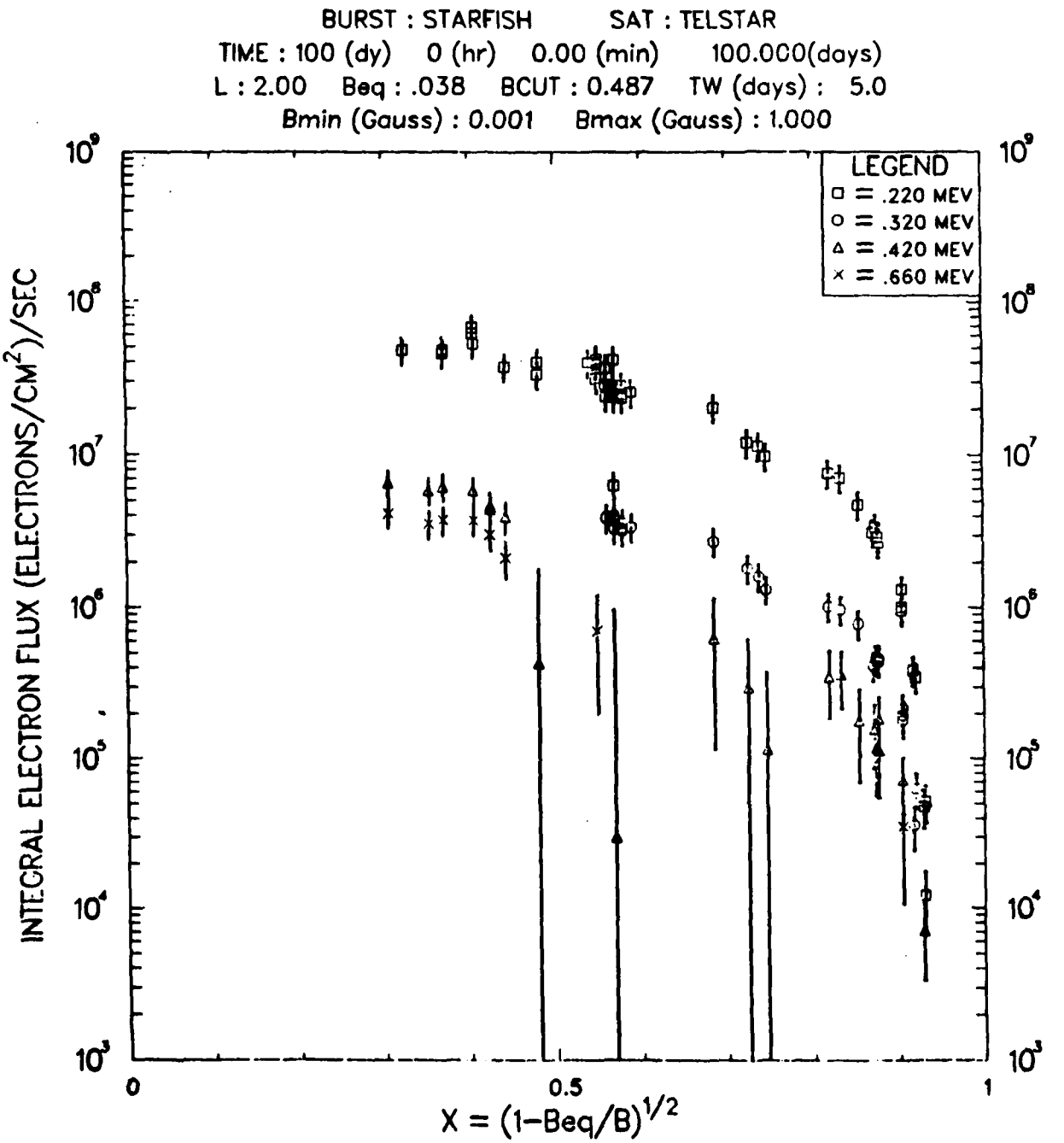

Figure 8(b). Raw Telstar Data in Regions I, II, and III (late time).

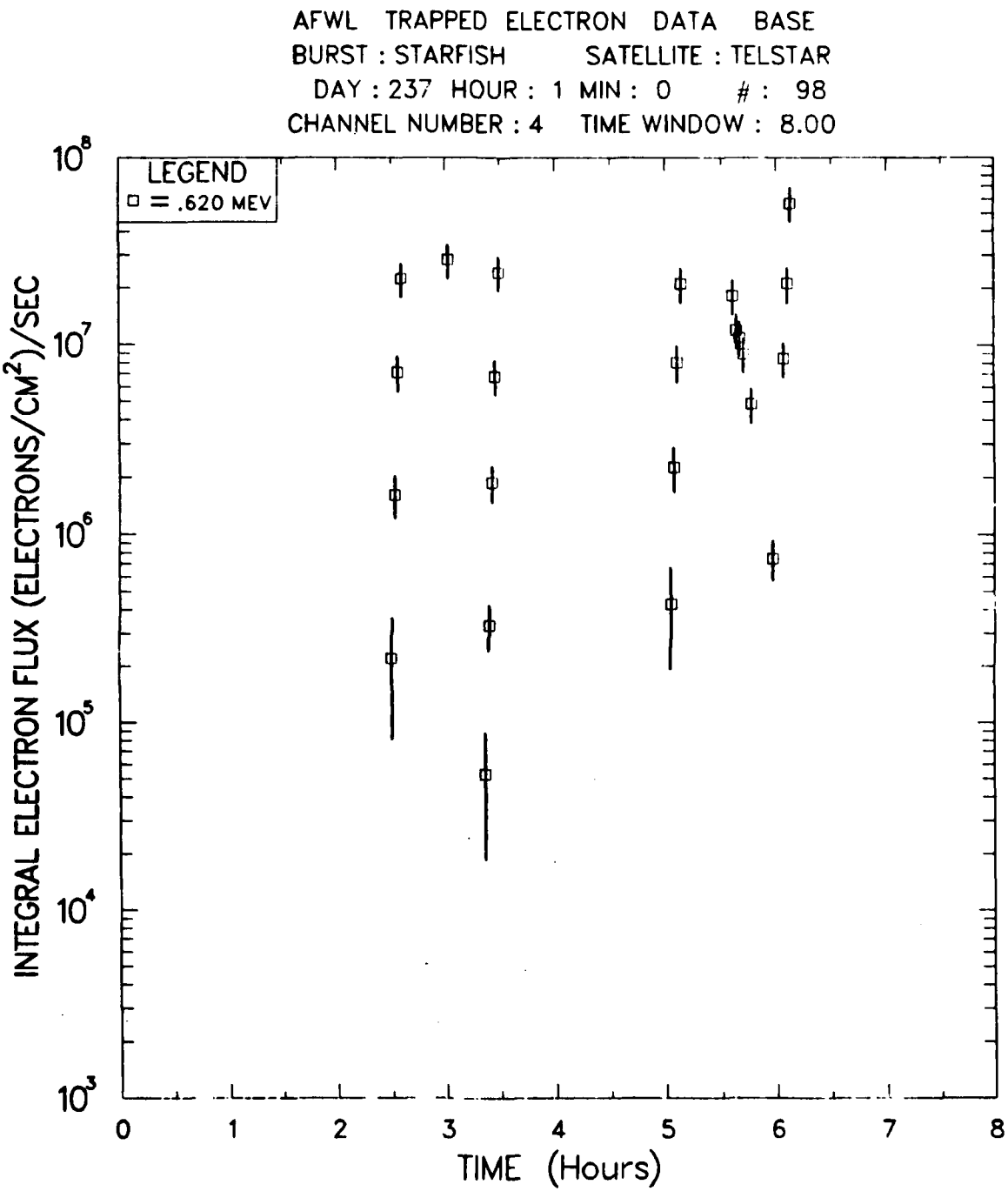

Figure 9. Typical Raw Data Coverage for 8 Hours (*B-L* values not shown).

Figures 10 (a) through (g) shows raw data from Explorer XV over the time period of the Russian 2 and 3 bursts, at times corresponding to those shown in Figure 3, for comparison. It is apparent that fewer points are plotted from the AFWL data base in Figures 10 (a) through (g) than were plotted by Roberts in Figure 3 for the 1.9 Mev electrons, even though the satellite and time periods of coverage were the same. These discrepancies are not resolved in this study, although the previously alluded-to L-rounding procedure may account for the differences.

The temporal progression of flux after one burst from one satellite (Telstar), at a typical L-value of 1.9, is shown in Figures 11 (a) through (h). Again, typical gaps in coverage of Regions I, II, and III are readily apparent over the 90 days shown.

As previously noted, only fundamental and two higher eignemodes (f_0, f_1, f_2) are used to fit the satellite data (Appendix C). The third eigenmode (f_3) is not used because Shulz and Lanzerotti (Ref. 45:163) suggest that the modes greater than two rapidly vanish. Initially, the steady-state function (f_∞) was used along with the fundamental, but this solution was found to be "competing" with the fit for the fundamental, in the sense that the linear constants tended to be roughly equal in magnitude and tended to alternate in sign. Shulz (Ref. 47:22 23) indicates that the f_∞ and f_0 functions should resemble each other in shape. Also, Pfitzer (Ref.37) has subtracted the background from all flux data, and the background should approximate the steady-state, f_∞, solution. For these reasons, the steady-state solution was not used in the data fit.

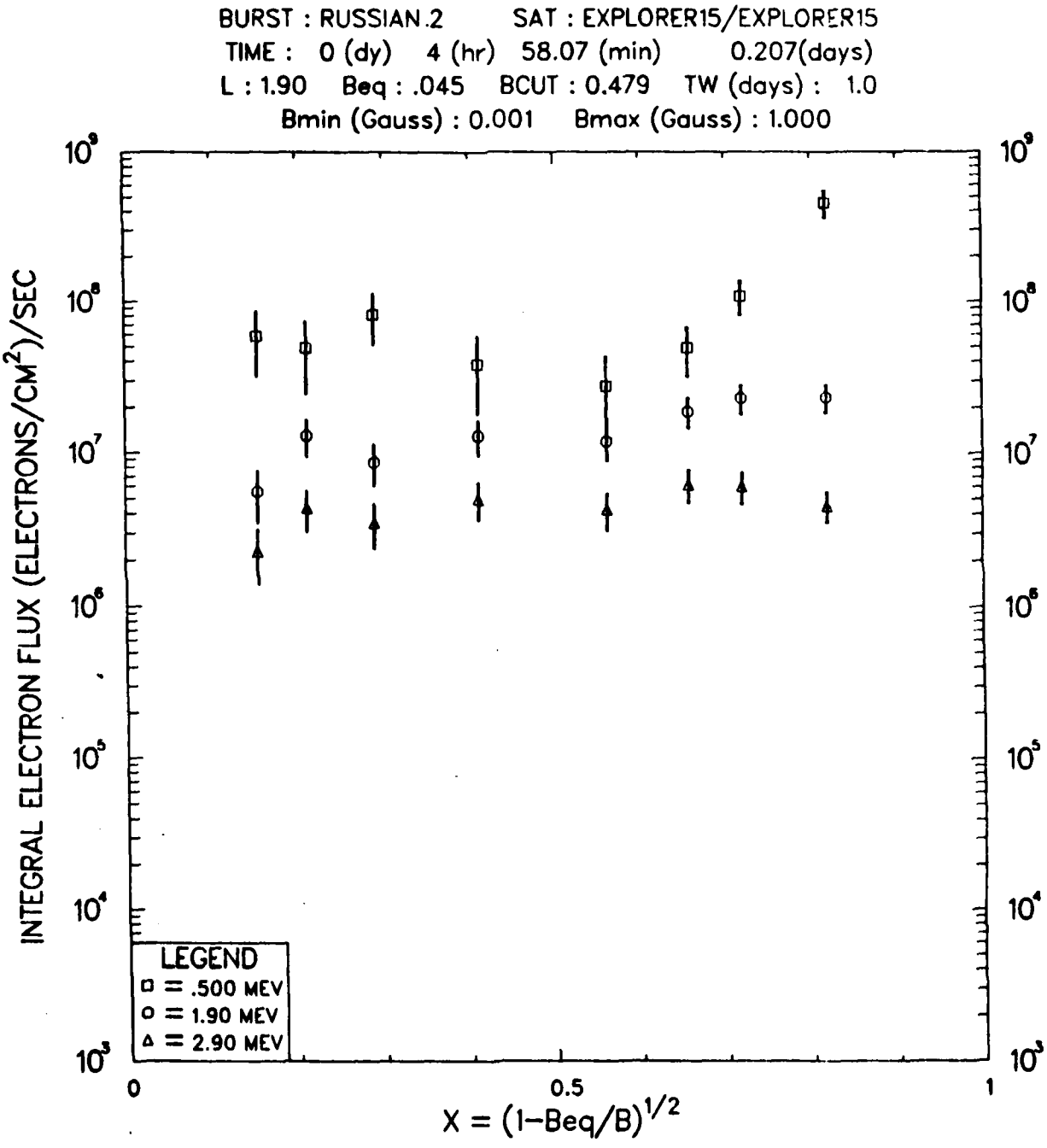

Figure 10(a). Raw Explorer 15 Data at Times Corresponding to Figure 3.

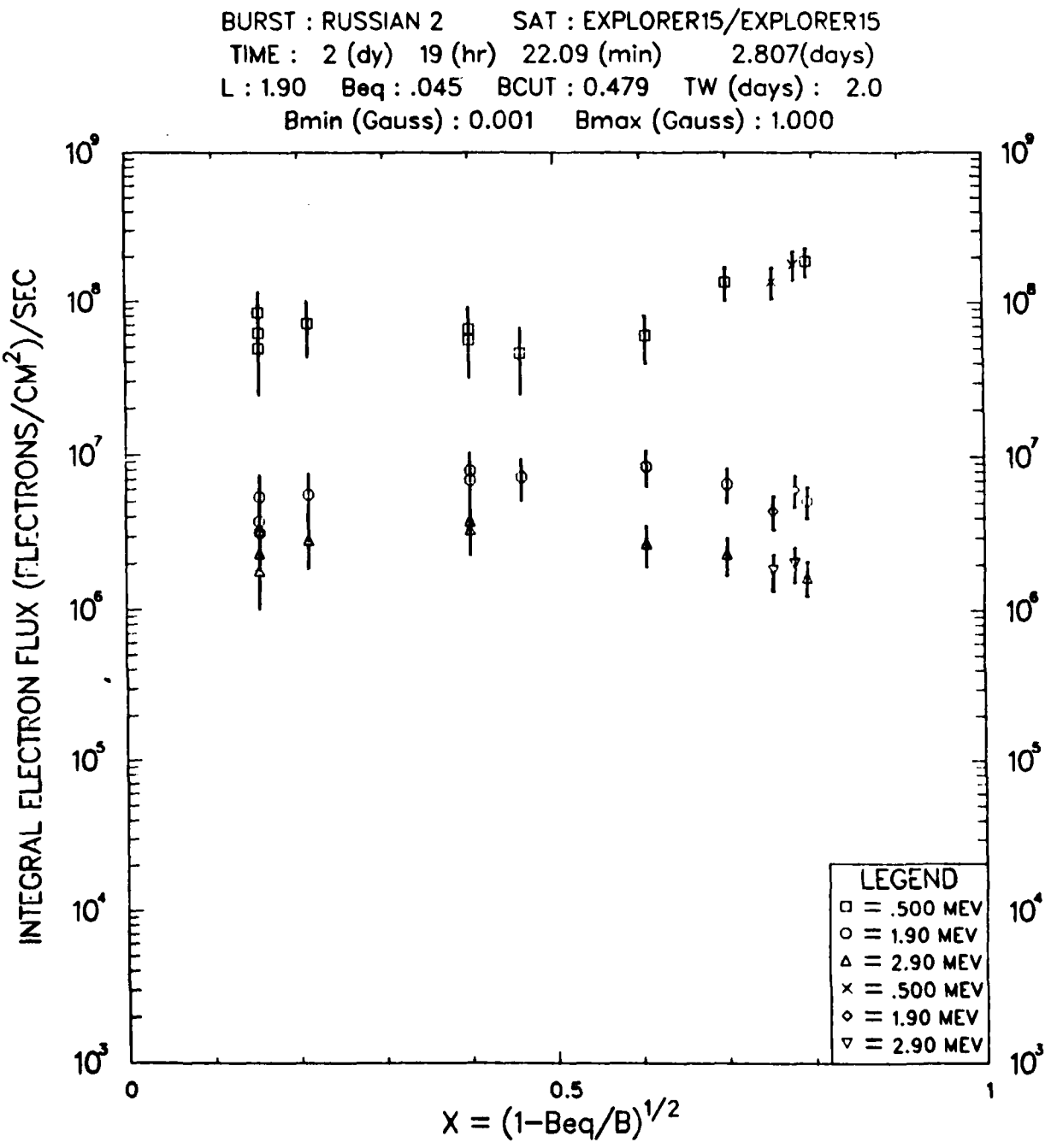

Figure 10(b). Raw Explorer 15 Data at Times Corresponding to Figure 3.

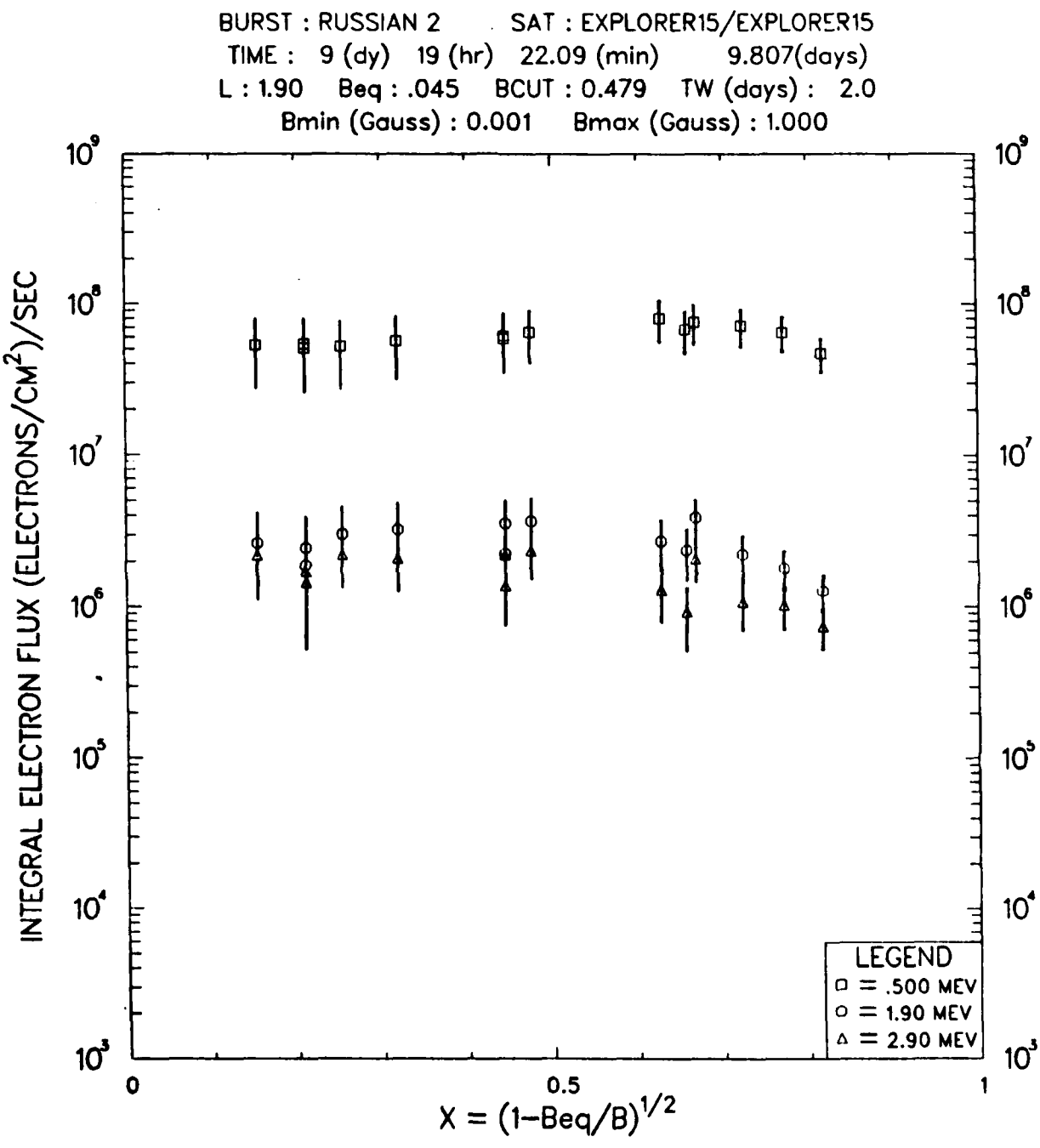

Figure 10(c). Raw Explorer 15 Data at Times Corresponding to Figure 3.

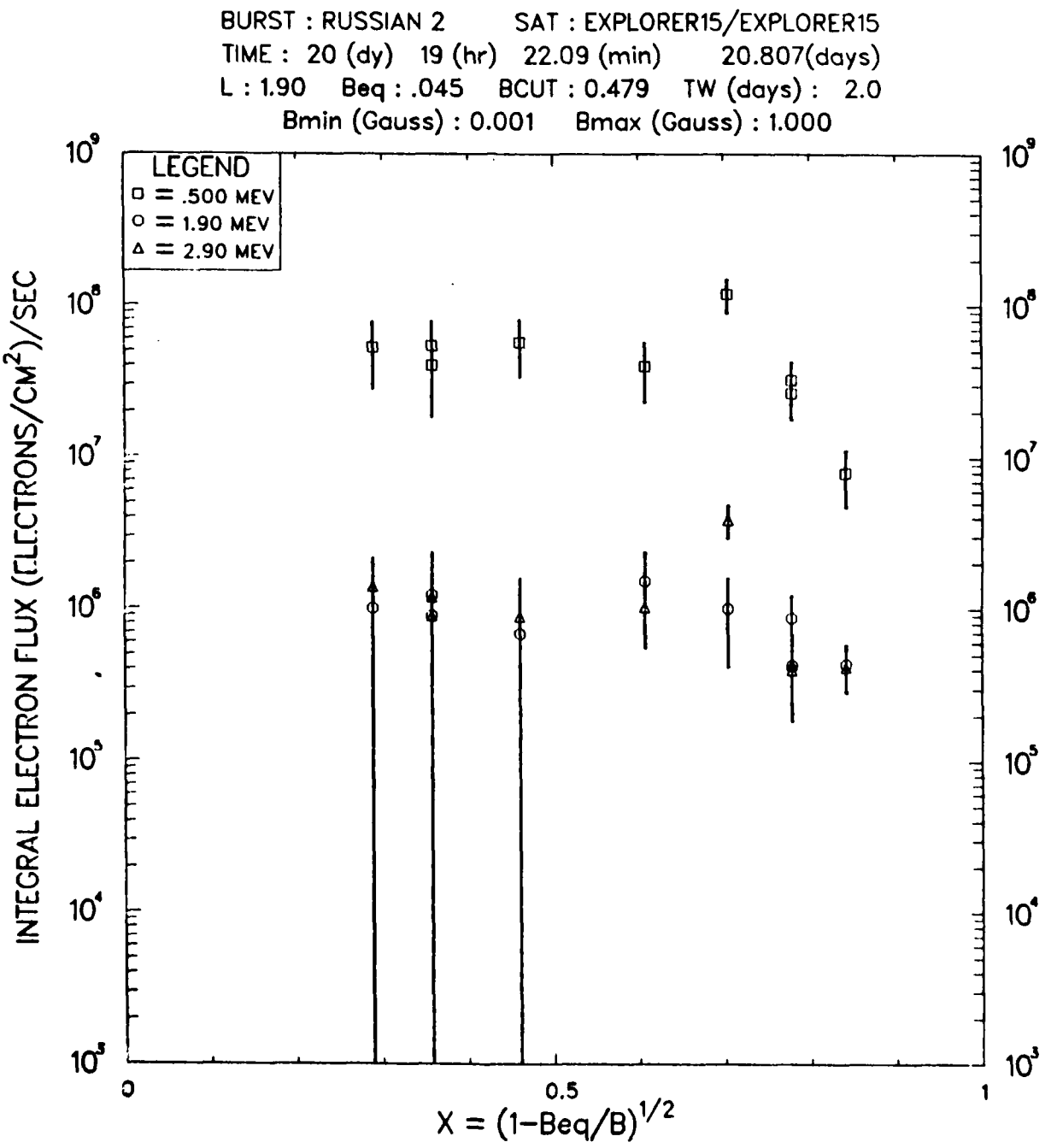

Figure 10(d). Raw Explorer 15 Data at Times Corresponding to Figure 3.

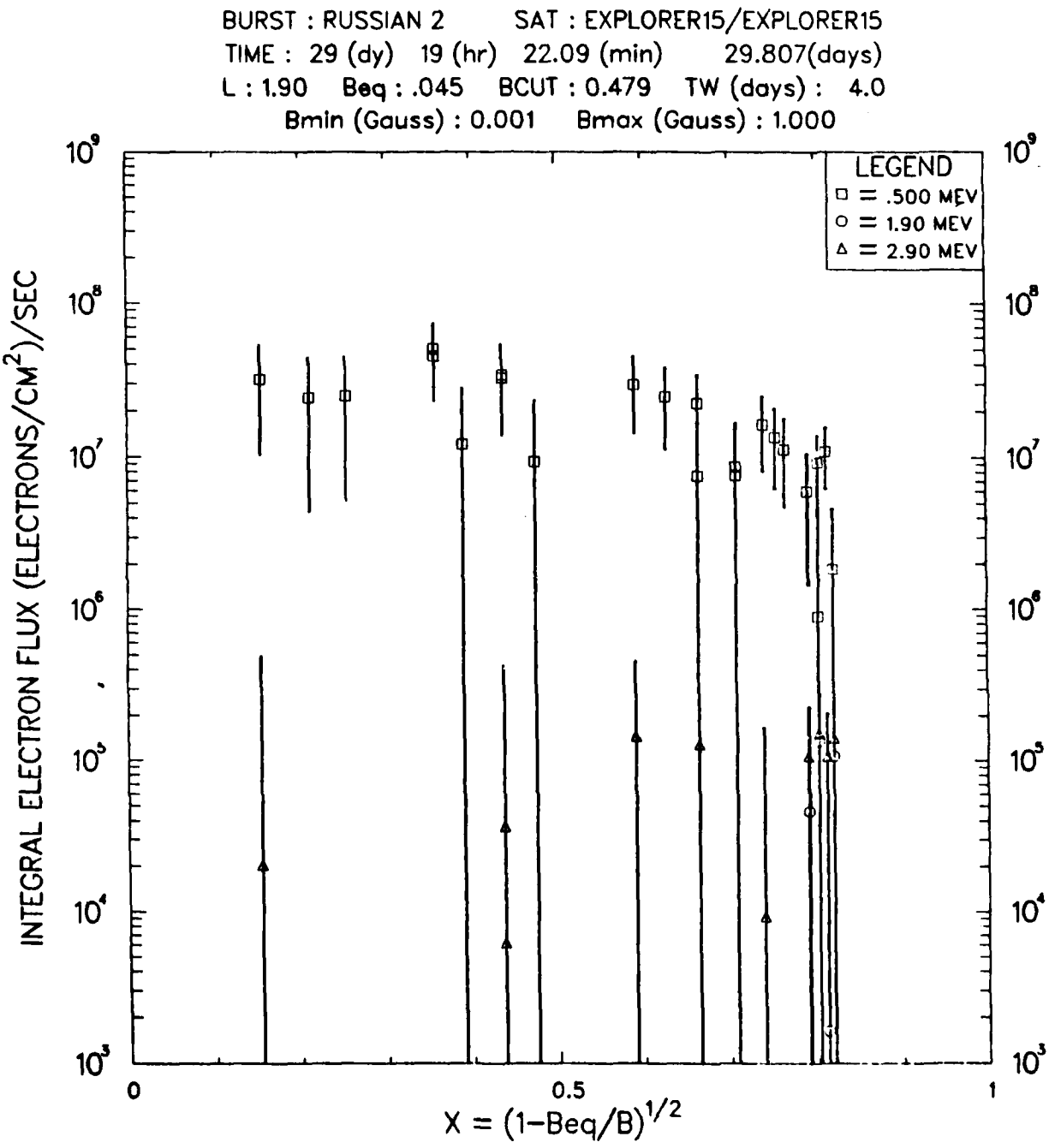

Figure 10(e). Raw Explorer 15 Data at Times Corresponding to Figure 3.

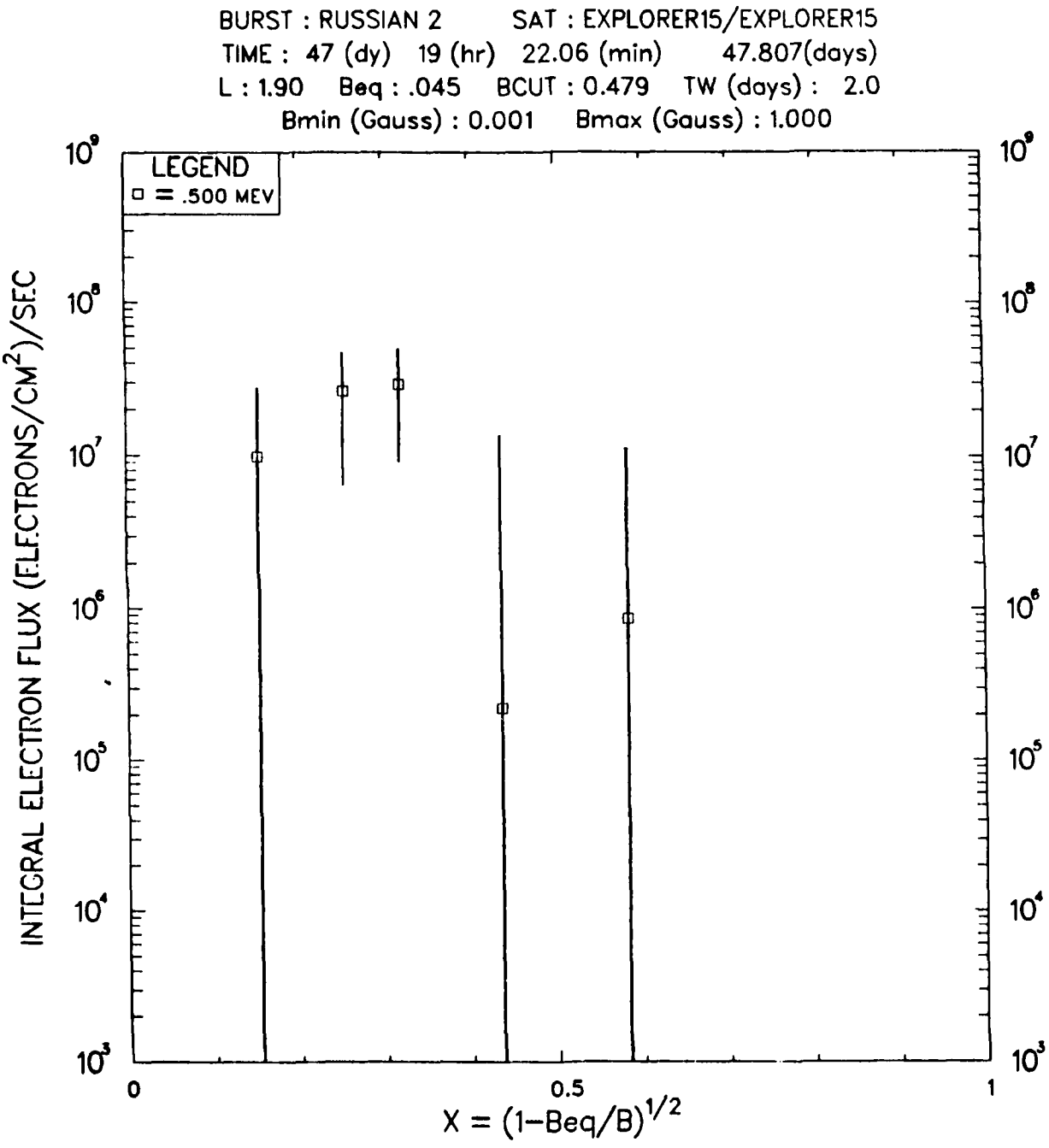

Figure 10(f). Raw Explorer 15 Data at Times Corresponding to Figure 3.

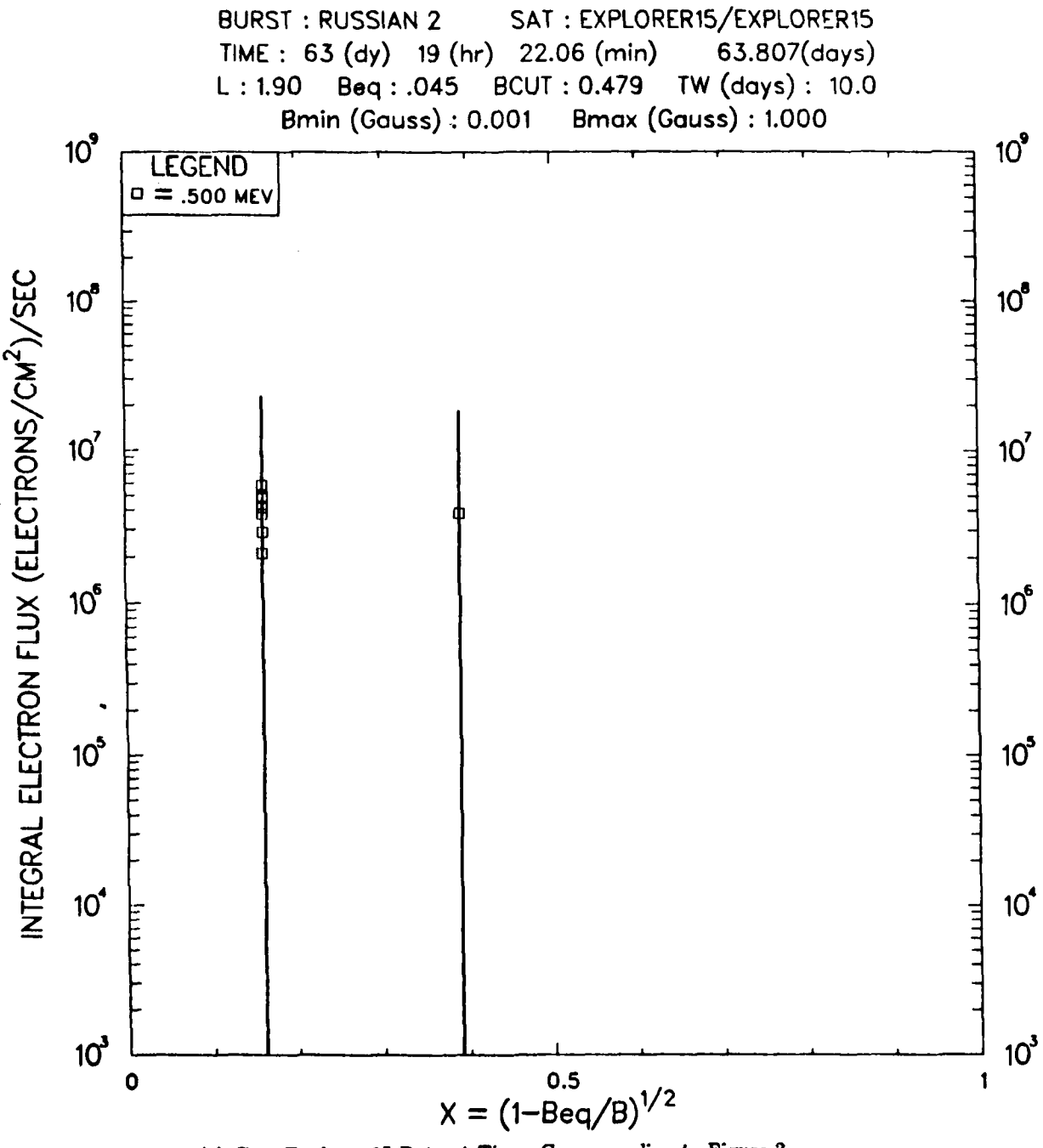

Figure 10(g). Raw Explorer 15 Data at Times Corresponding to Figure 3.

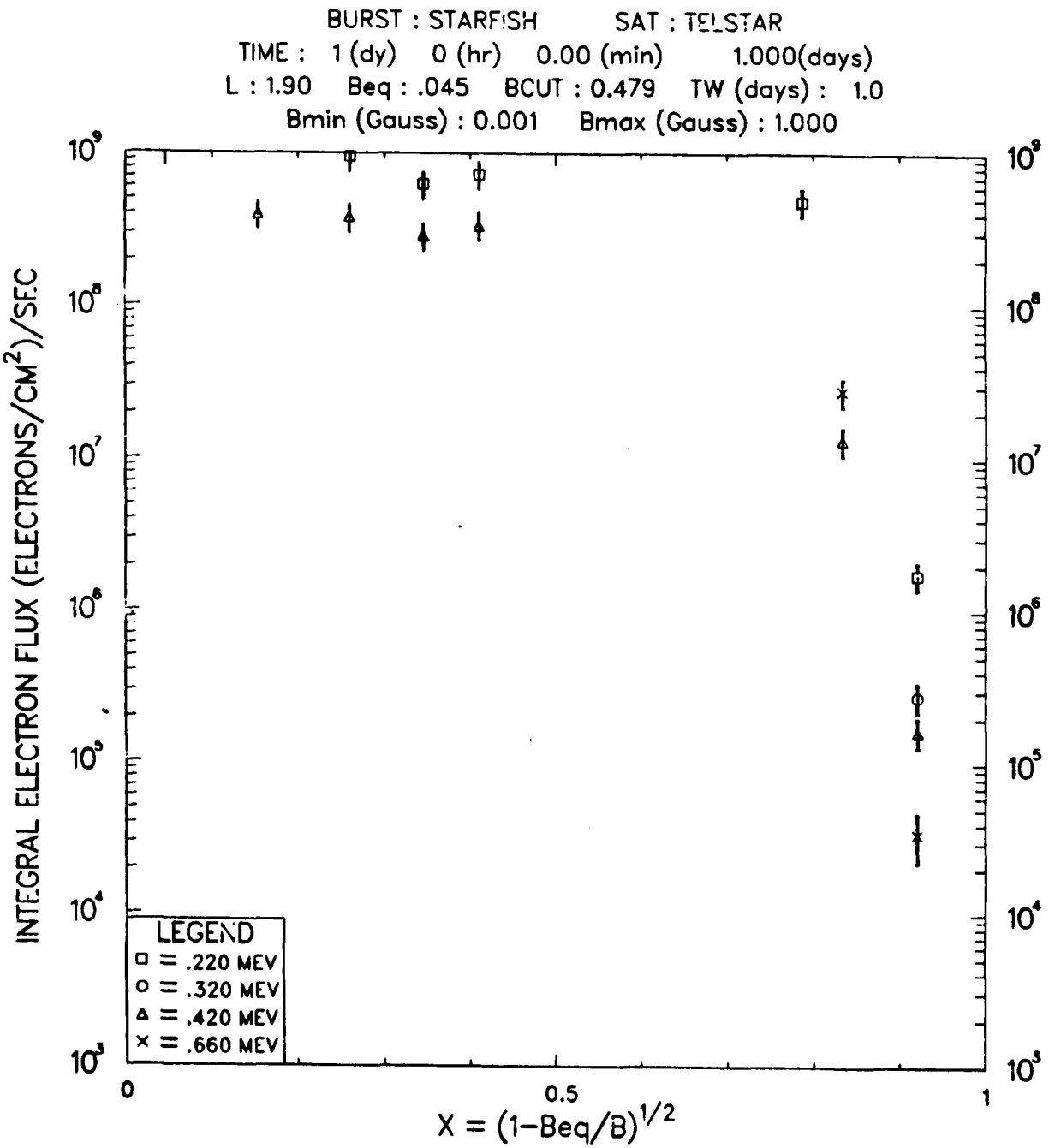

Figure 11(a). Temporal Progression for Raw Telstar Data from 1 to 90 Days Post-Burst.

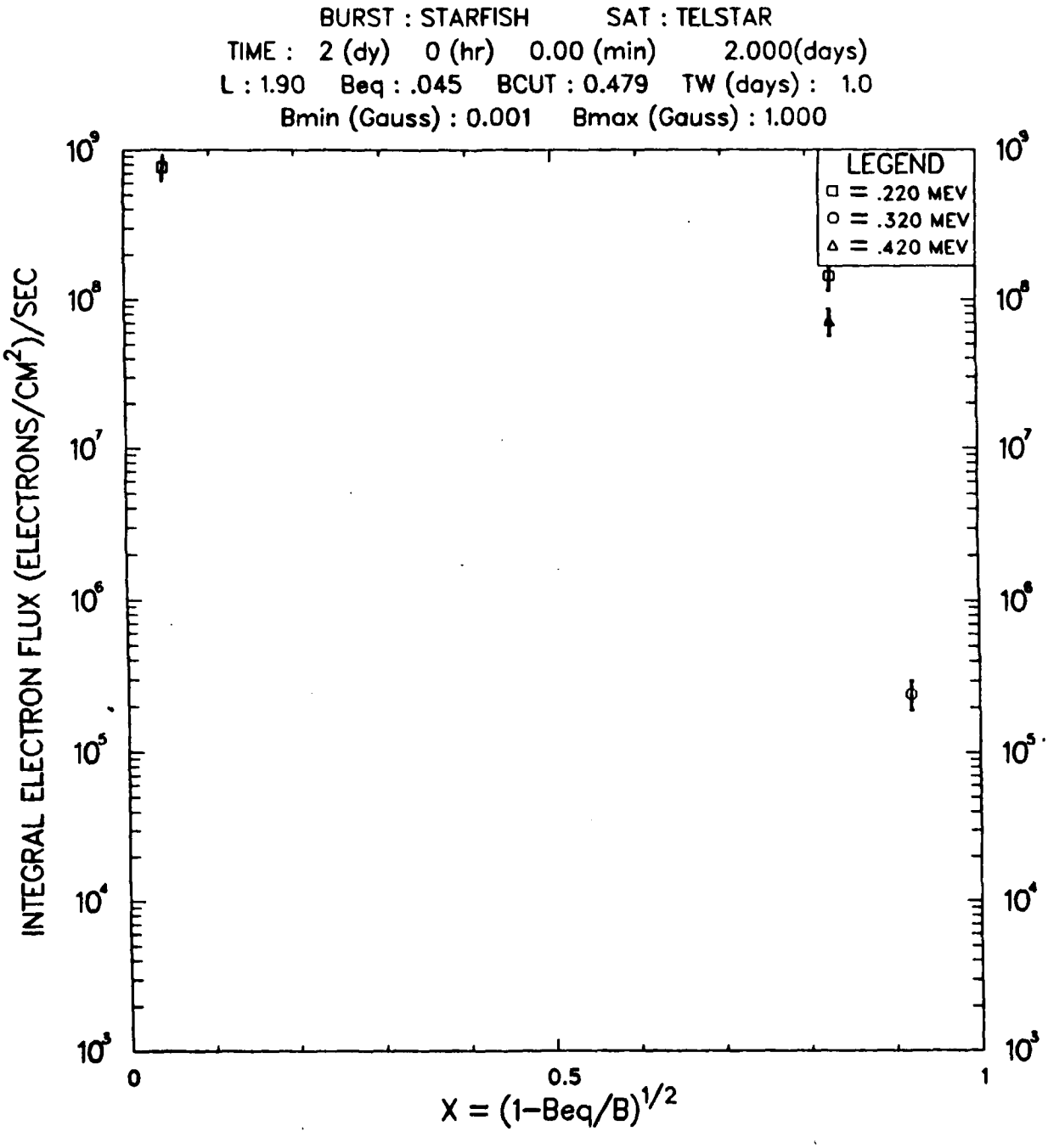

Figure 11(b). Temporal Progression for Raw Telstar Data from 1 to 90 Days Post-Burst.

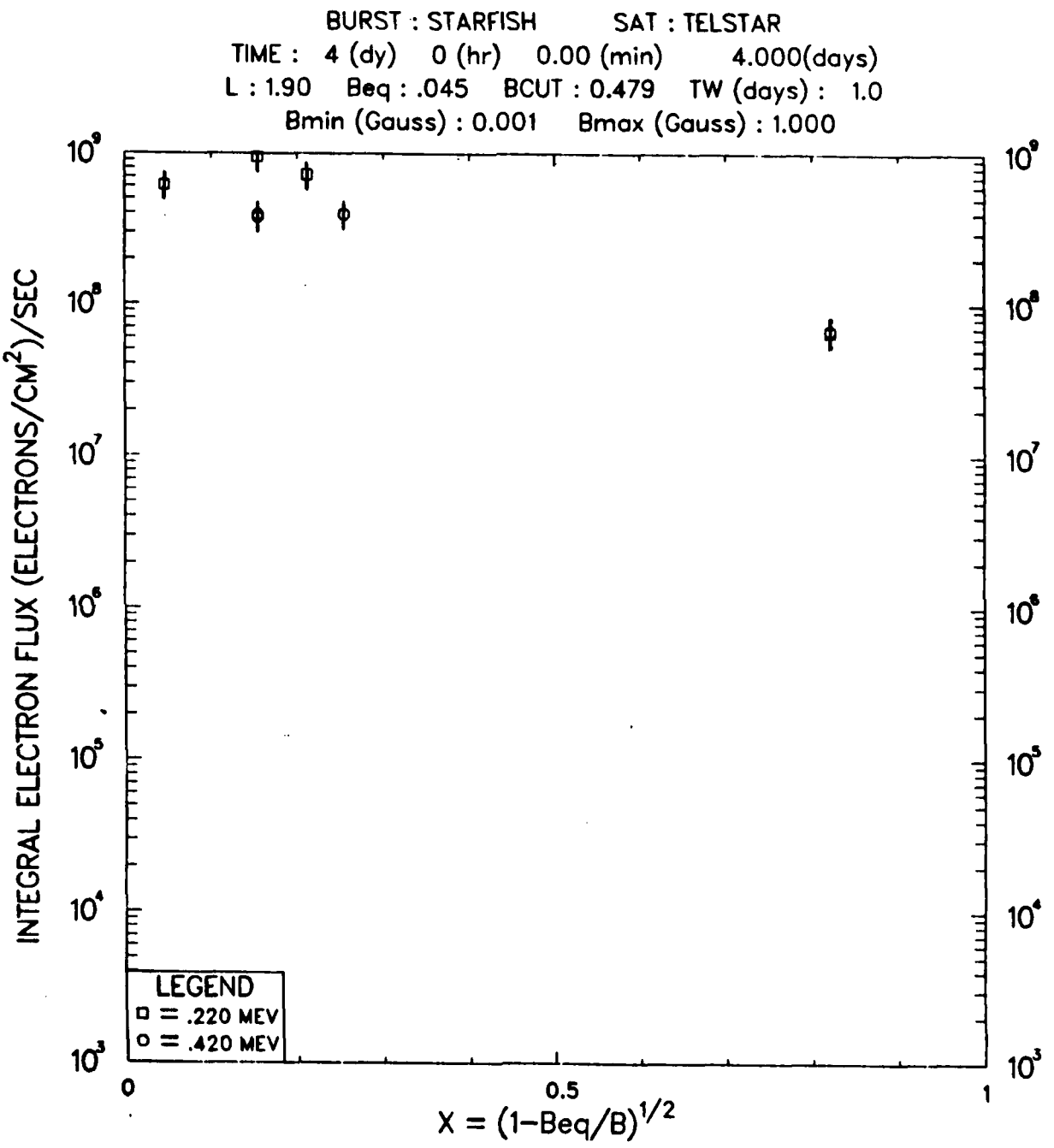

Figure 11(c). Temporal Progression for Raw Telstar Data from 1 to 90 Days Post-Burst.

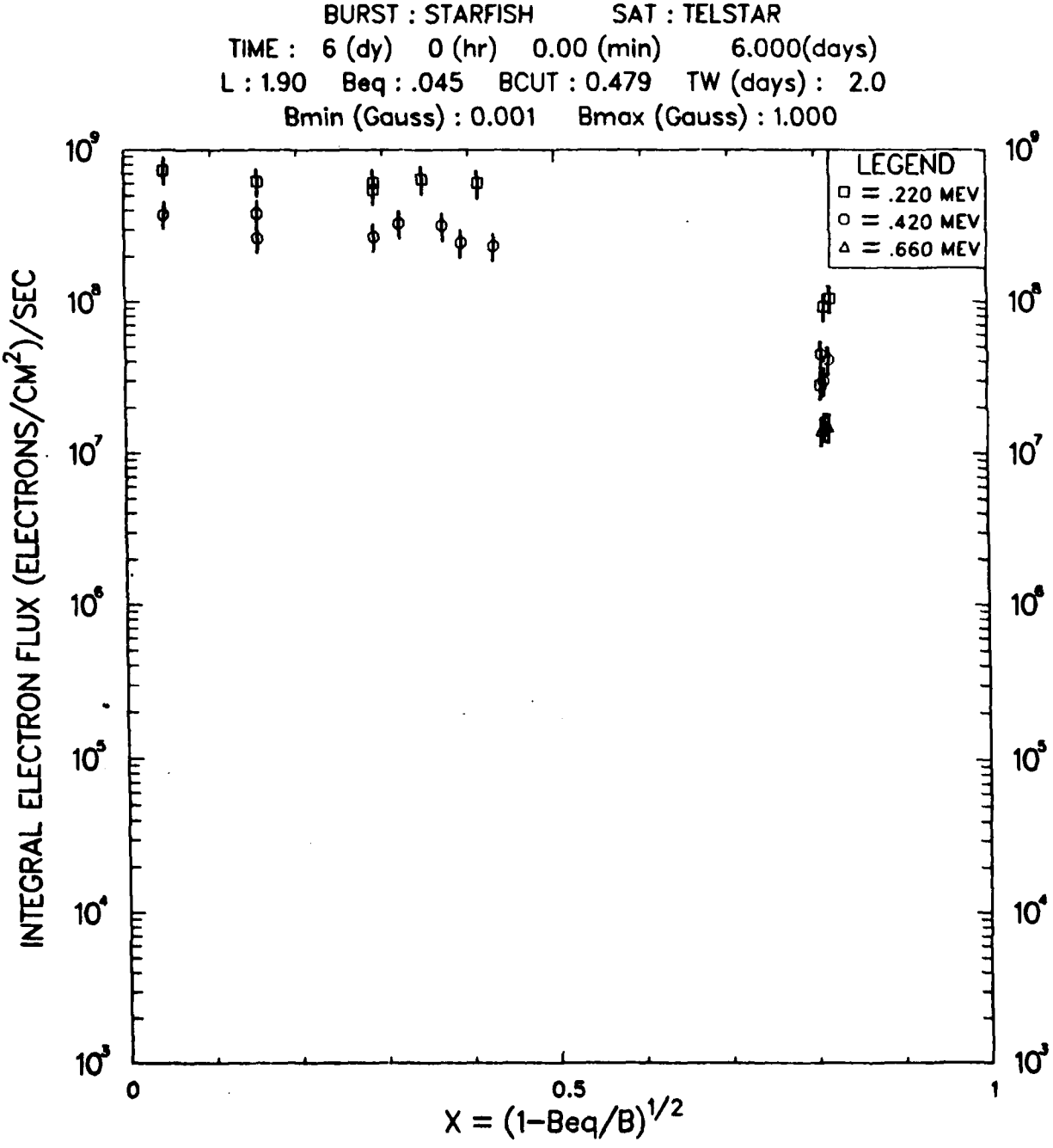

Figure 11(d). Temporal Progression for Raw Telstar Data from 1 to 90 Days Post-Burst.

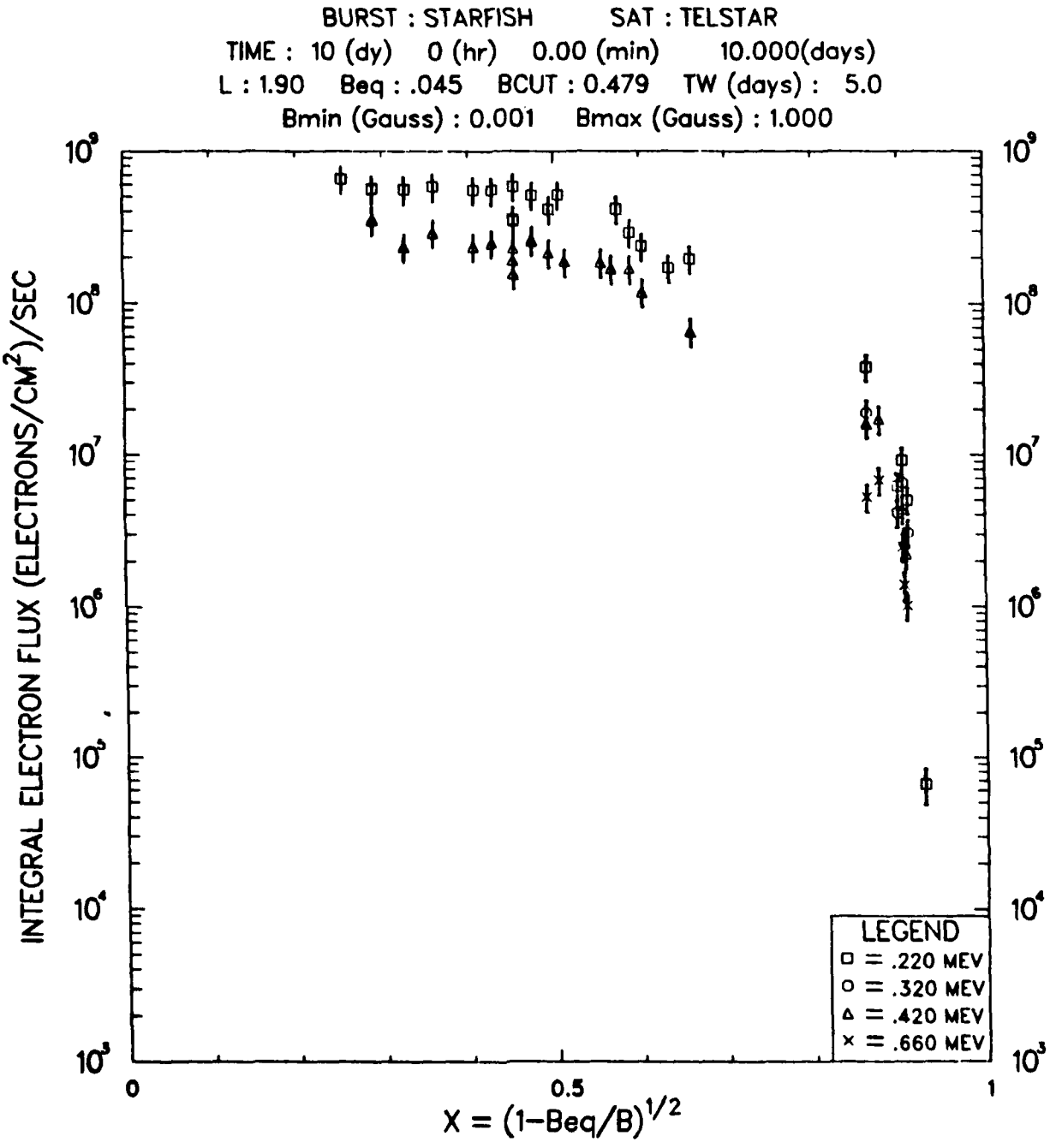

Figure 11(e). Temporal Progression for Raw Telstar Data from 1 to 90 Days Post-Burst.

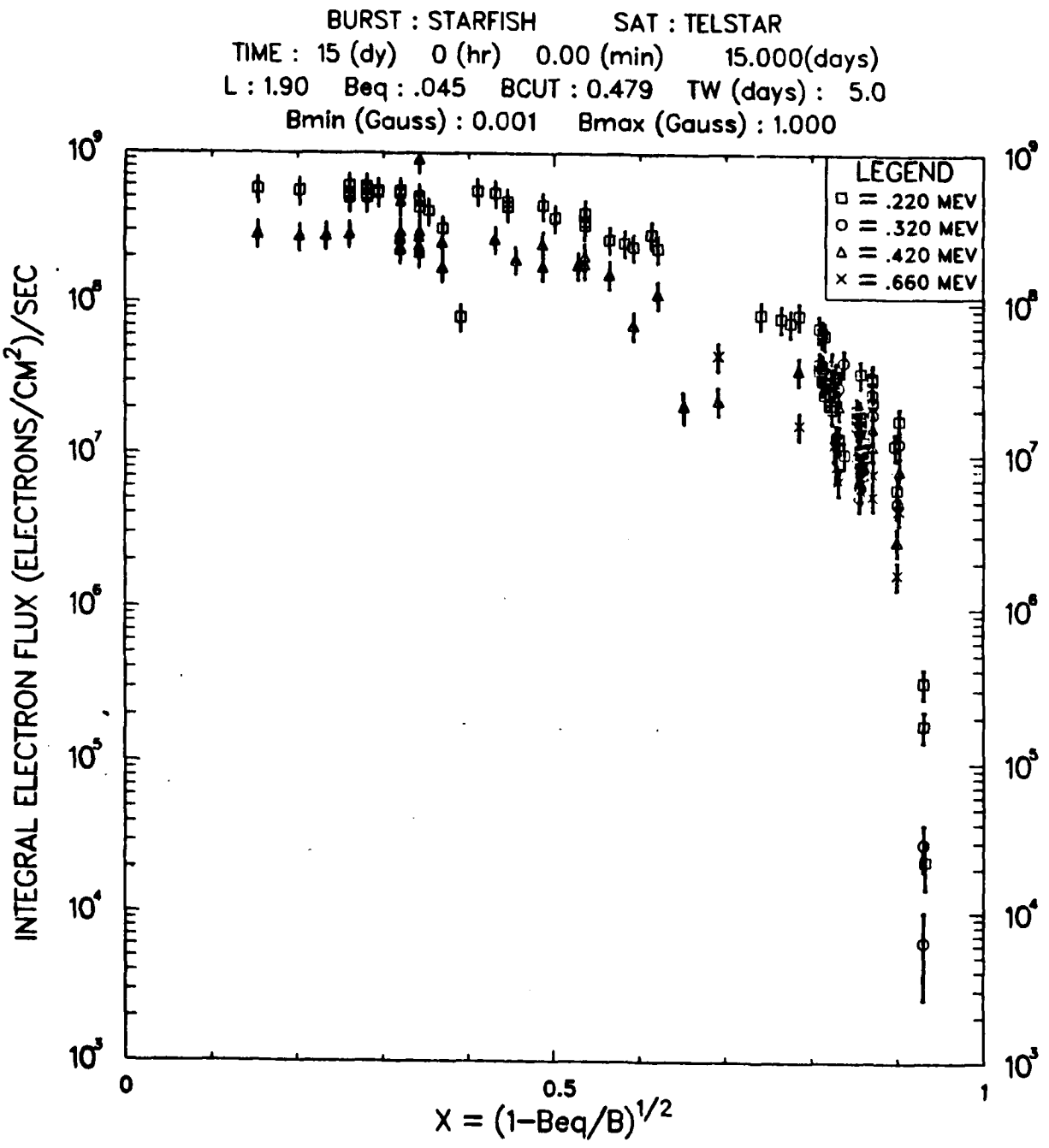

Figure 11(f). Temporal Progression for Raw Telstar Data from 1 to 90 Days Post-Burst.

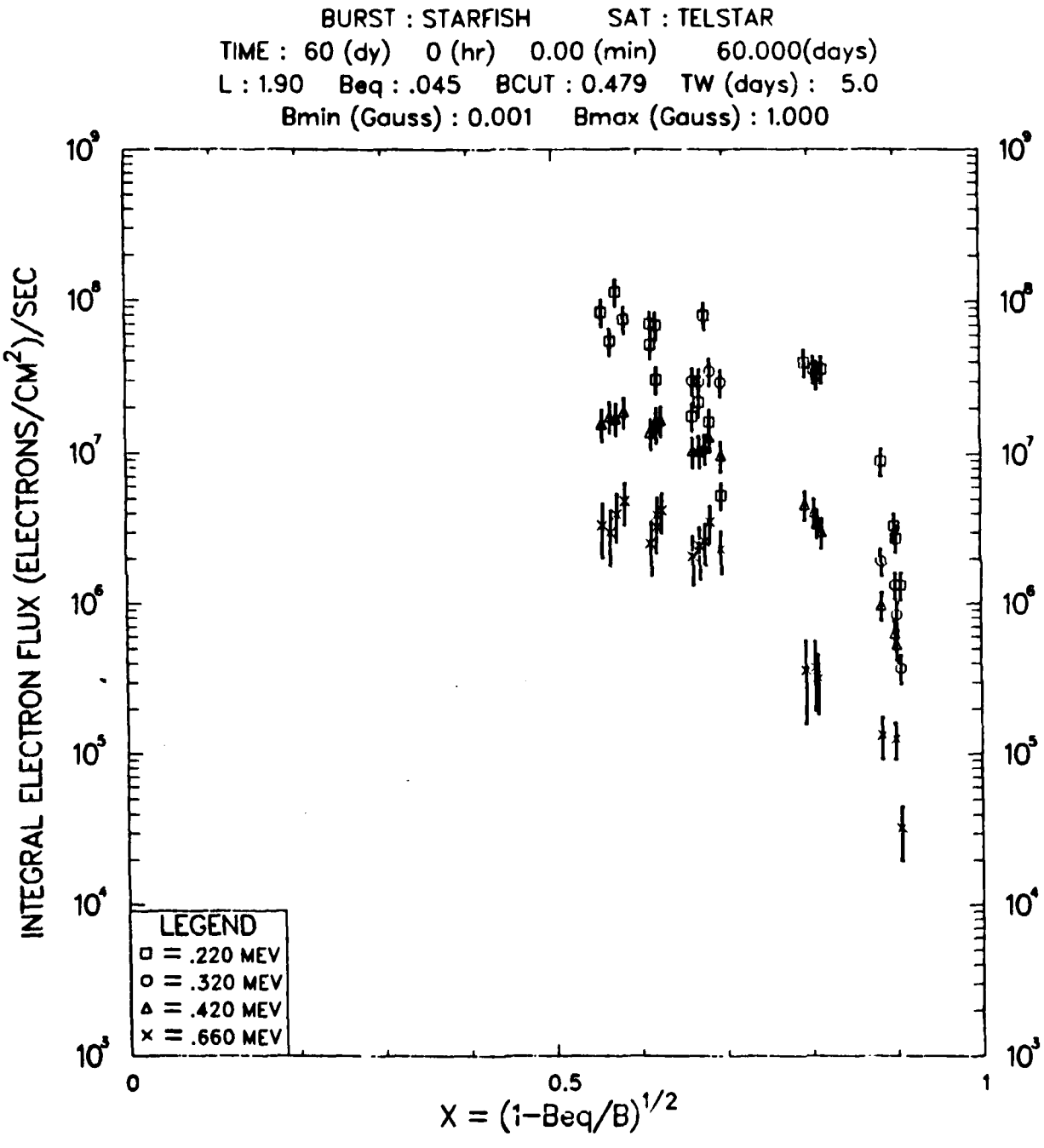

Figure 11(g). Temporal Progression for Raw Telstar Data from 1 to 90 Days Post-Burst.

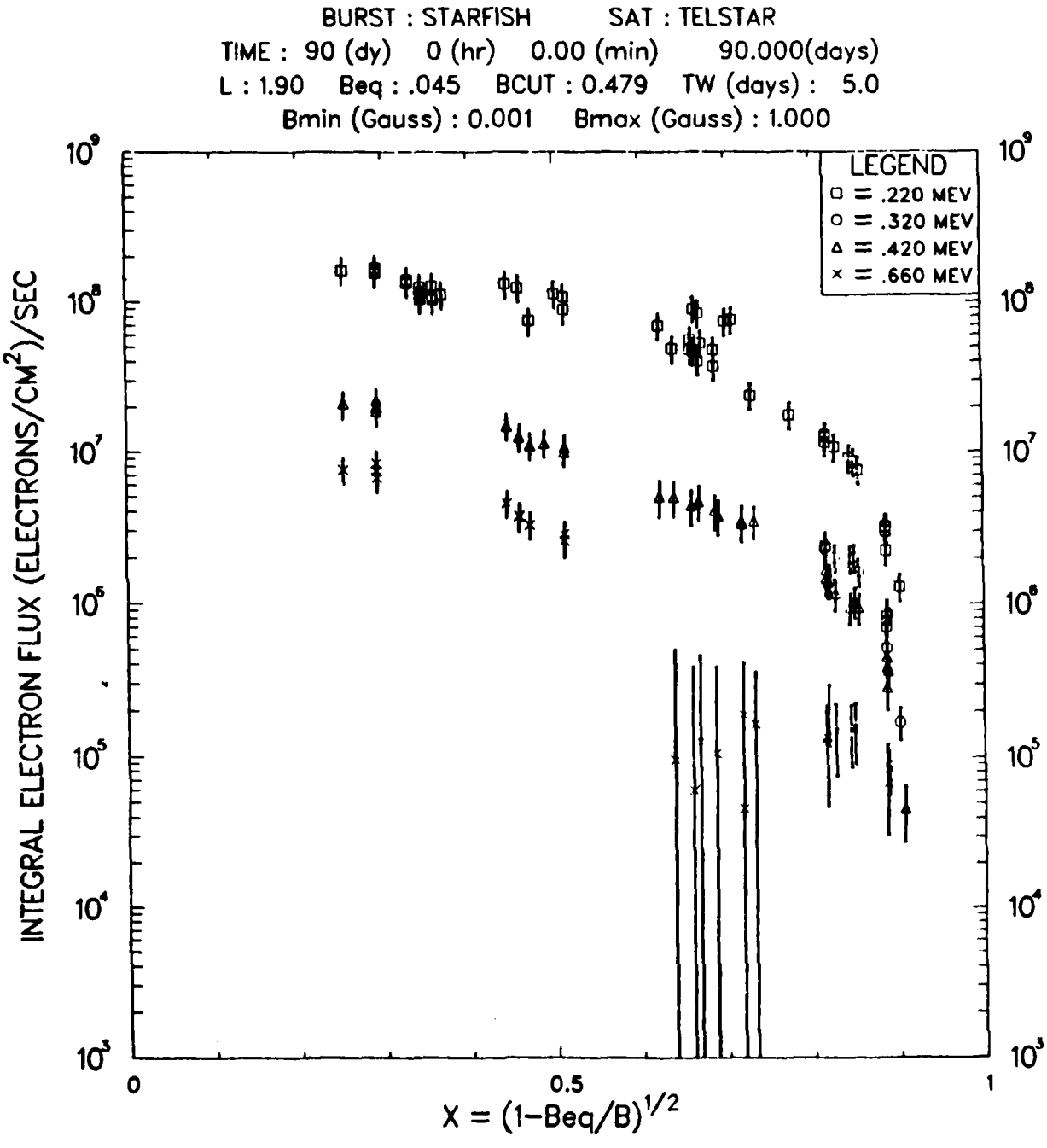

Figure 11(h). Temporal Progression for Raw Telstar Data from 1 to 90 Day : Post-Burst.

V. RESULTS AND DISCUSSION

Figures 12 and 13 show the typical temporal progression of raw data at two representative L values, $L = 2.3$ and $L = 2.4$. Included on those figures are the flux curves calculated from the amplitude coefficients and decay times fitted to that data by Electrofit. As previously noted, the curves shown on any given figure may vary slightly in time from the individual data points, since the curves represent only the one time-instant corresponding to the start time plus one-half the time window of the plot. Figures 12 and 13 represent maximum freedom of the fit, since each τ is free to vary independently of the other τ's.

Figure 14 shows the same temporal data progression with different fitted curves. The curves in this figure were calculated under the restriction that the ratios of the τ's were fixed at the theoretical values of 1:1/9:1/25; hence, only τ_1 was really varying in a random sence.

Figure 15 shows similar data progression and fitted curves where the τ's were allowed to freely vary, subject to the constraint that $\tau_0 > \tau_1 > \tau_2$. Also, this was an initial run with 500 tries for convergence, vice 96 tries. In addition, the computed flux was used in the iteration process to eliminate non-physical (negative) solutions. The solution was restricted to being positive at four different times and at five different equatorial pitch angles. Although this is an initial run with only a small amount of data used, it indicates that the recommendations in Chapter VI should be pursued.

Table XVII shows the fitted linear amplitude coefficients and exponential decay times (in days) at constant Energy and L-shell for a representative subset of the data examined in this study. The sheer volume of resultant fits and calculated curves made it impossible to include all results in this report. The values shown in Table XVII were computed with the τ's allowed to vary freely.

Figures 12 and 13 are considered representative of the results of the fitting model. It is apparent from examination of Figures 12 and 13 that the pitch-angle diffusion theory and flux computation method developed in this report are consistent with experimental measurements. Higher eigenmodes are readily discernible at the lowest energy in the Figures or the first five days, and are not visible at later times. These higher eigenmodes are not discernible in the plots at the higher energies; Table XVII shows that these modes are present, but at much lower levels, in some cases. The calculated curves show a reasonable fit to the data even at late times, consistent with the assumption of exponential decay.

Examination of Figures 14 and 15 shows that some inconsistencies remain to be resolved in the use of this fitting method. The calculated flux curves for the low-energy data points also appear to be slightly lower than optimum, while the high-energy data appears to be fitted better by the model. This may be partially explained by the existence of many lower data points in the vicinity of the loss cone which tend to "drag down" the overall fit. Any change in the cutoff value significantly affects the fit by shifting the "vertical" portion of the curve toward or away from those points. However, this cannot account for the entire difference of the curves from the data. The energy dependence may be treated less than optimally in the choice of functional solution made in this study. If the chosen functional solution is not the correct one, it may be nevertheless close enough to correct to give a reasonable fit at high energy, but be significantly in error at lower energy. A different functional solution may fit the lower-energy groups better and yet still fit the high-energy electrons as well. Recommendation for the use of other functions is made in Chapter VI.

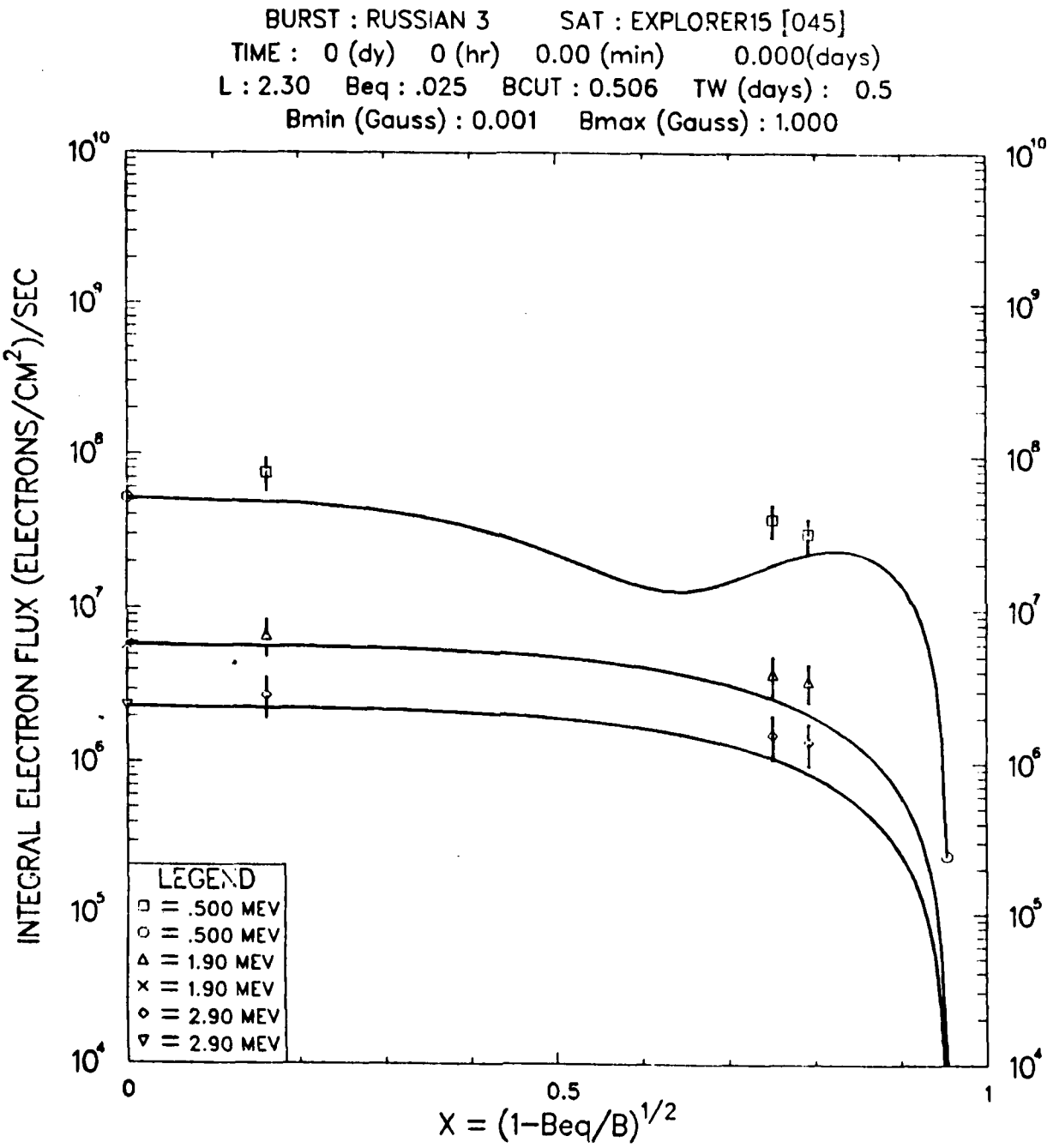

Figure 12(a). Temporal Progression of Raw Data and Fitted Flux Curves at $L = 2.3$ for Russian 3 Burst (r_n freely varying).

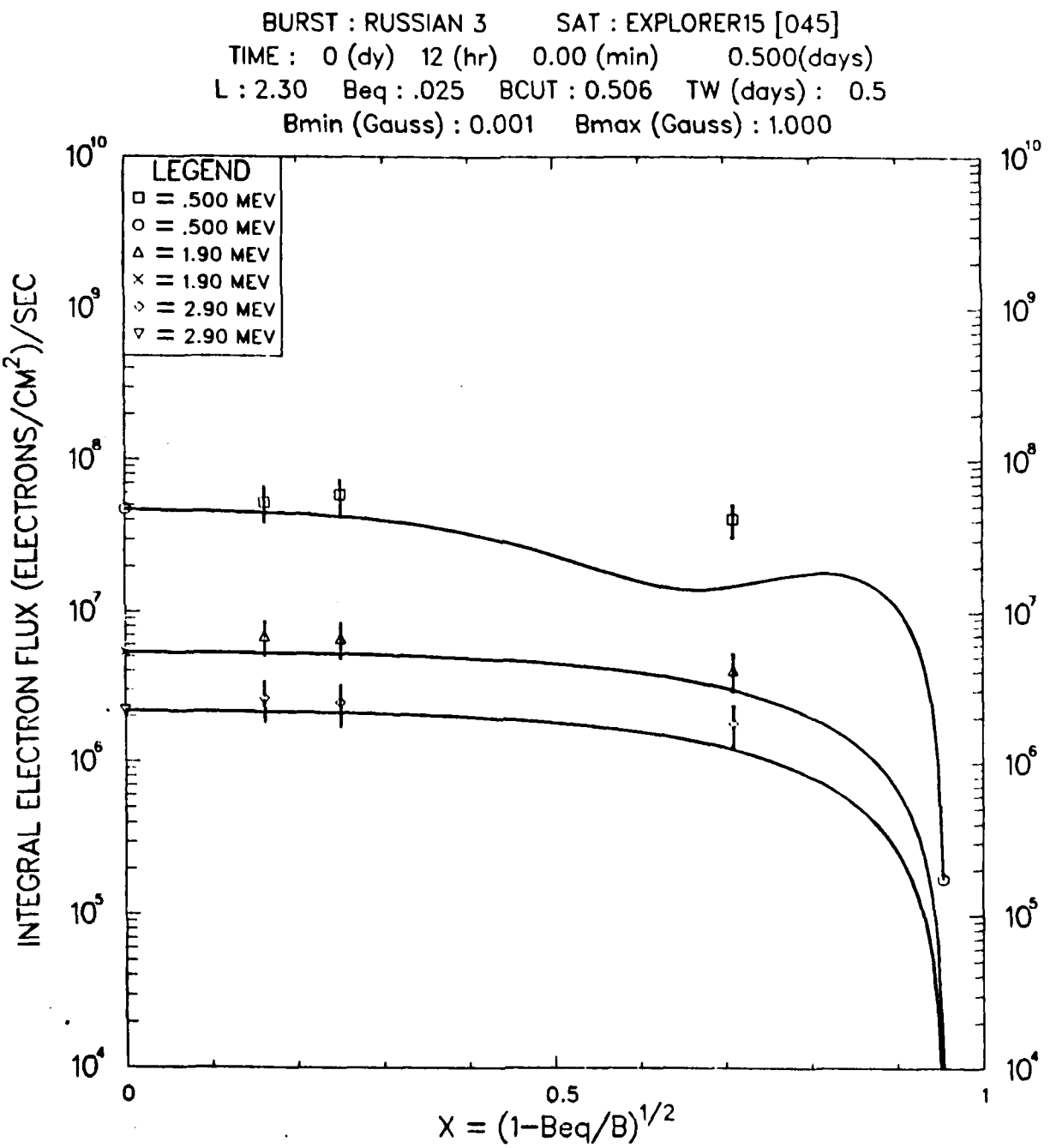

Figure 12(b). Temporal Progression of Raw Data and Fitted Flux Curves at $L = 2.3$ for Russian 3 Burst (r_n freely varying).

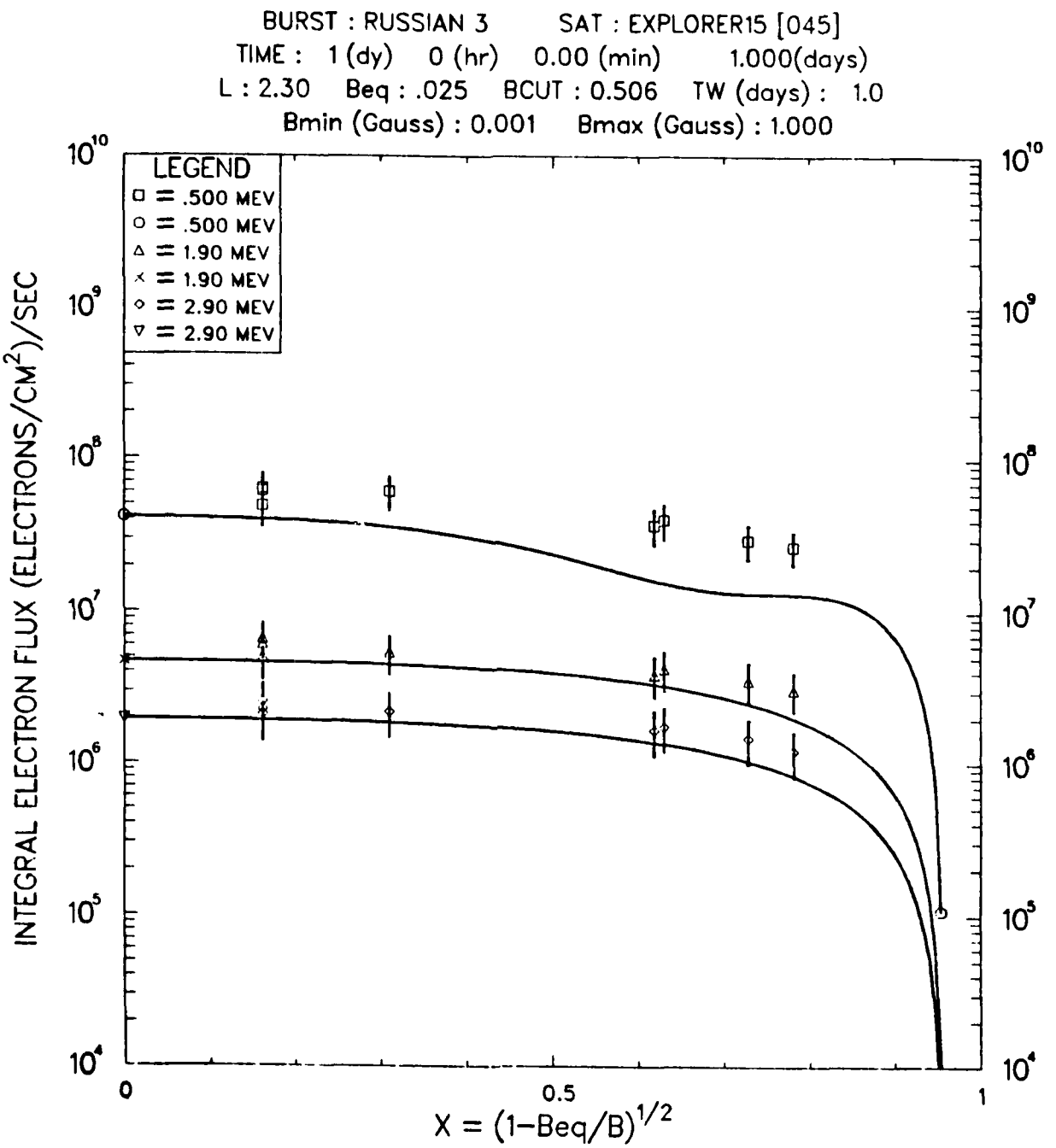

Figure 12(c). Temporal Progression of Raw Data and Fitted Flux Curves at $L = 2.3$ for Russian 3 Burst (r_n freely varying).

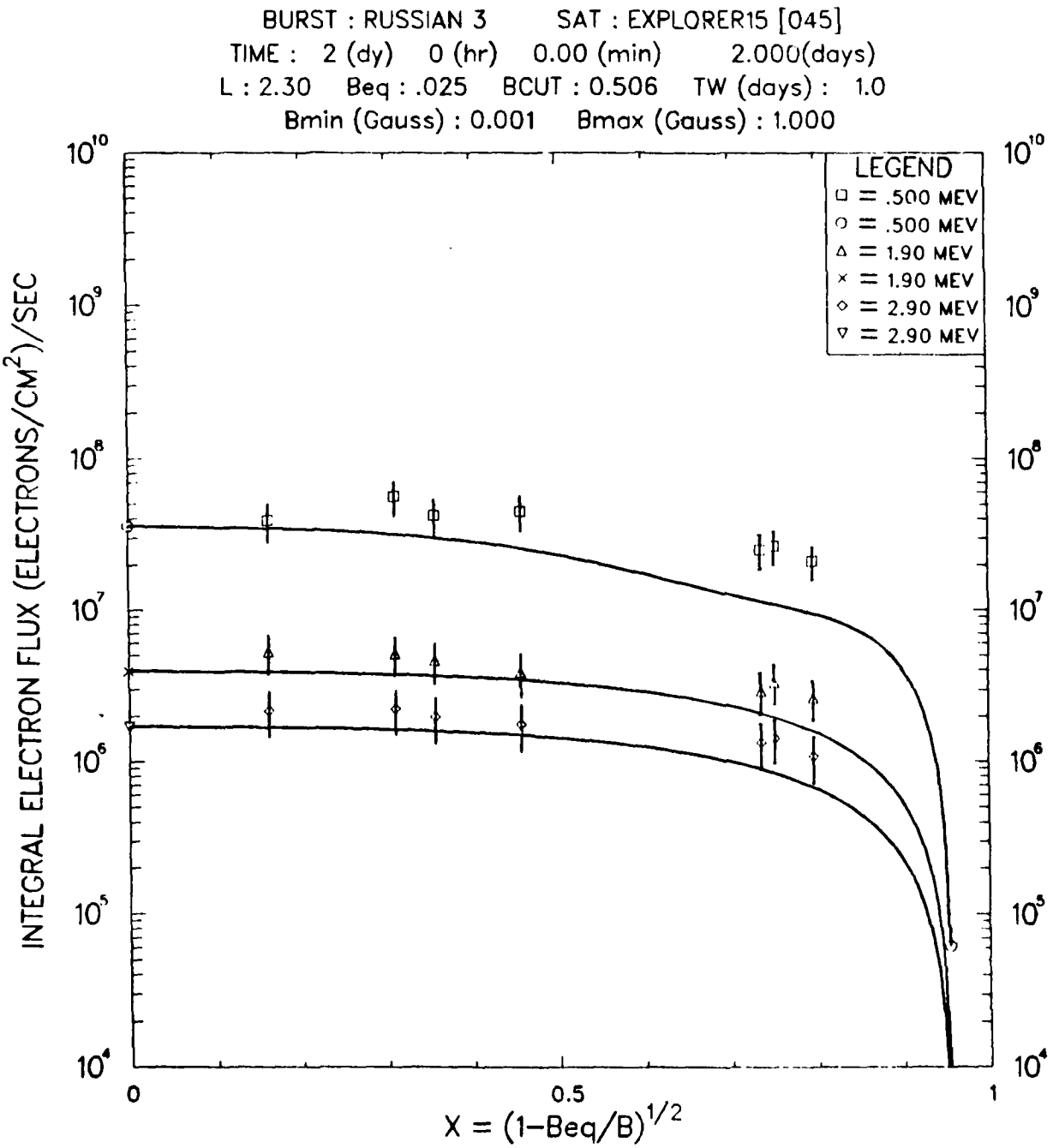

Figure 12(d). Temporal Progression of Raw Data and Fitted Flux Curves at $L = 2.3$ for Russian 3 Burst (r_n freely varying).

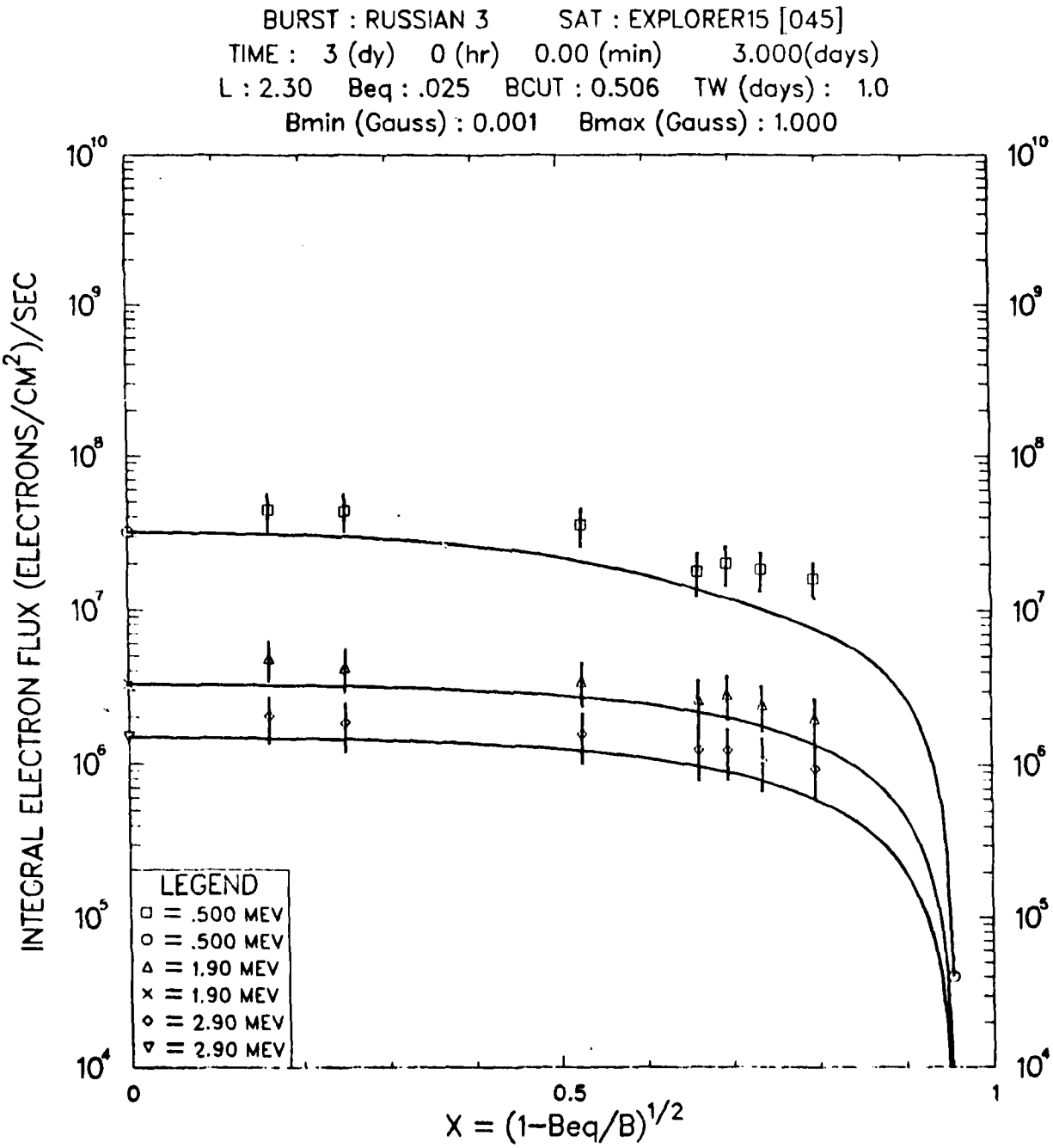

Figure 12(e). Temporal Progression of Raw Data and Fitted Flux Curves at $L = 2.3$ for Russian 3 Burst (r_n freely varying).

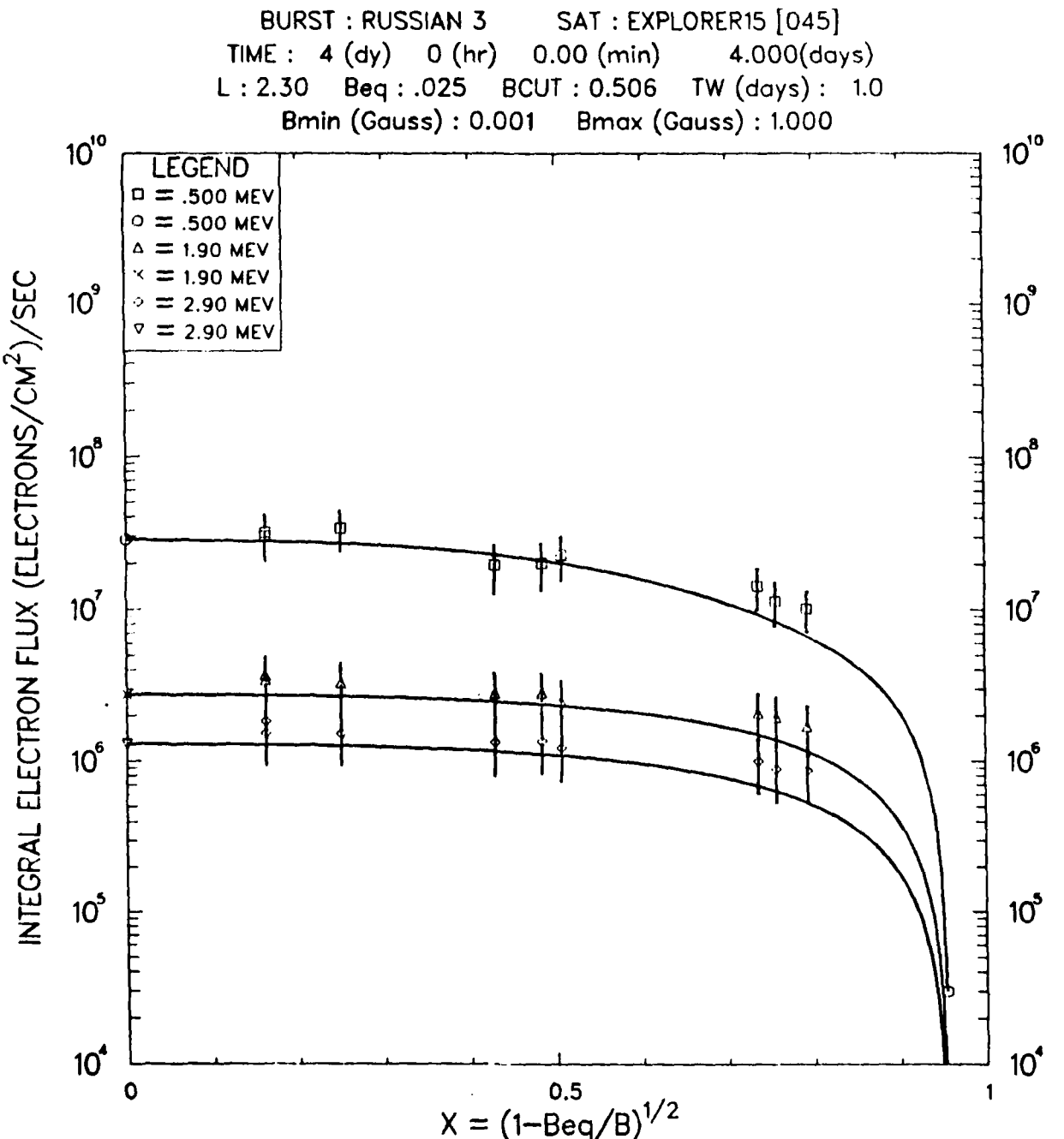

Figure 12(f). Temporal Progression of Raw Data and Fitted Flux Curves at $L = 2.3$ for Russian 3 Burst (τ_n freely varying).

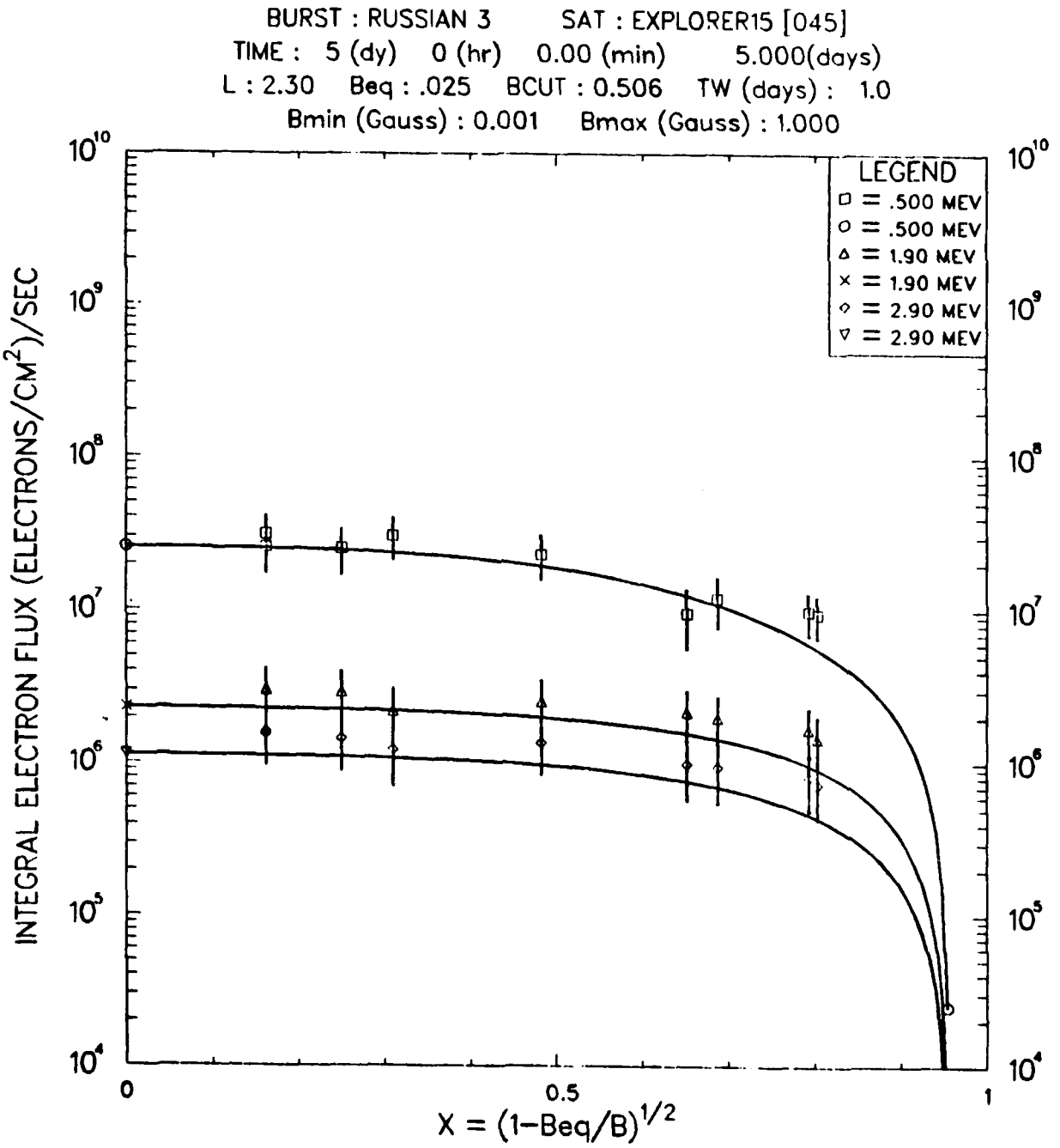

Figure 12(g). Temporal Progression of Raw Data and Fitted Flux Curves at $L = 2.3$ for Russian 3 Burst (r_n freely varying).

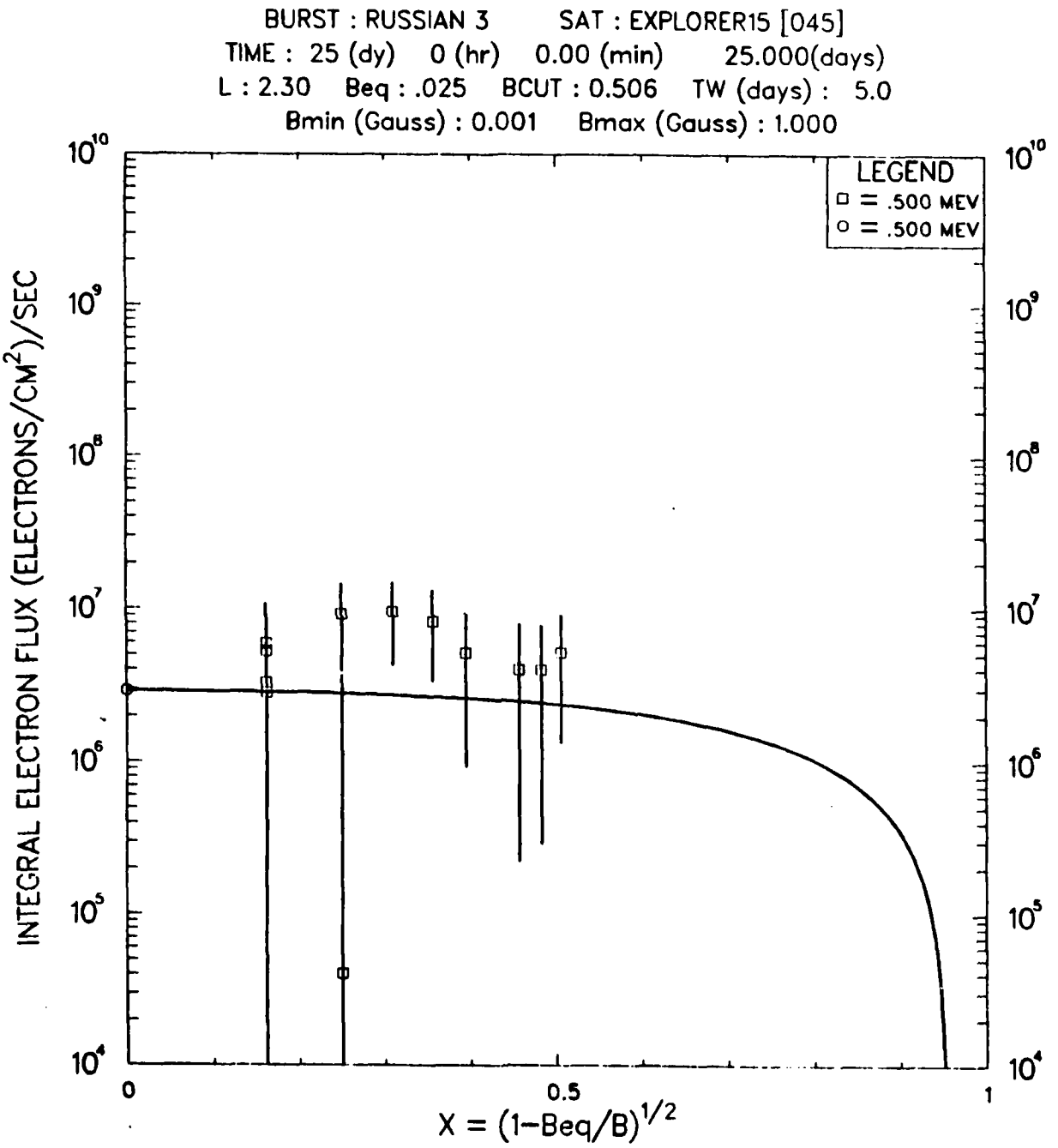

Figure 12(h). Temporal Progression of Raw Data and Fitted Flux Curves at $L = 2.3$ for Russian 3 Burst (r_n freely varying).

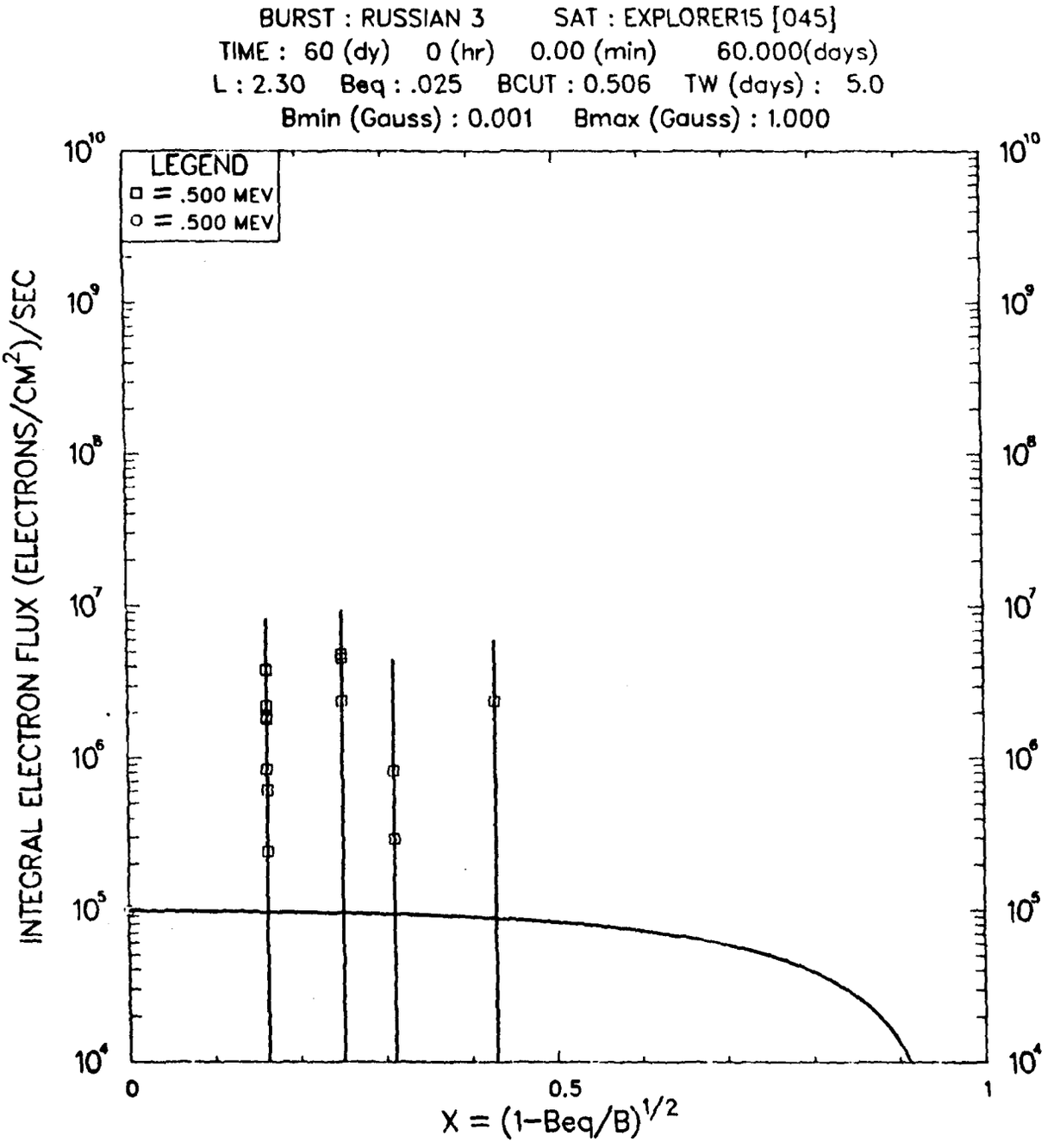

Figure 12(i). Temporal Progression of Raw Data and Fitted Flux Curves at $L = 2.3$ for Russian 3 Burst (τ_n freely varying).

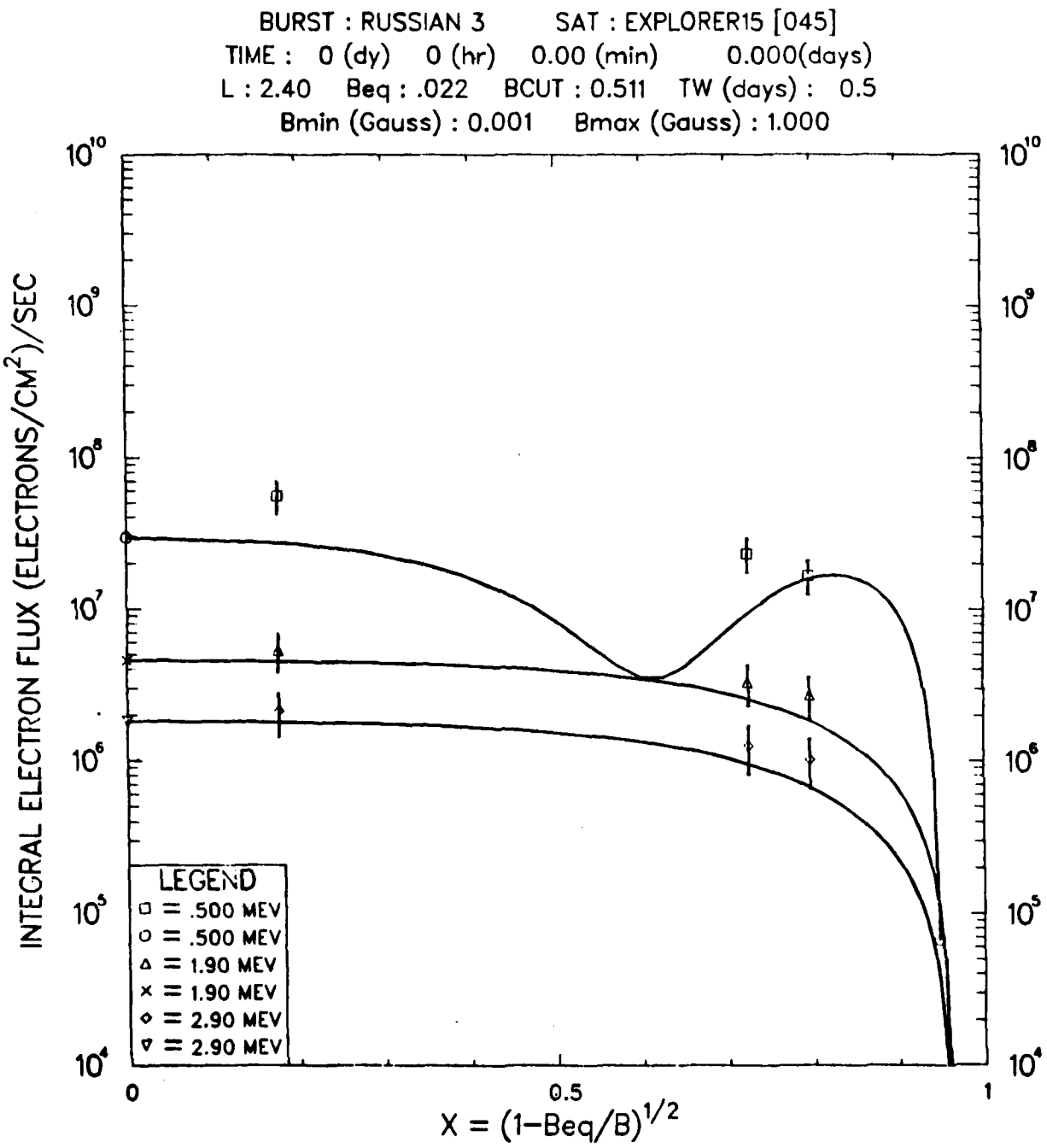

Figure 13(a). Temporal Progression of Raw Data and Fitted Flux Curves at $L = 2.4$ for Russian 3 Burst (r_n freely varying).

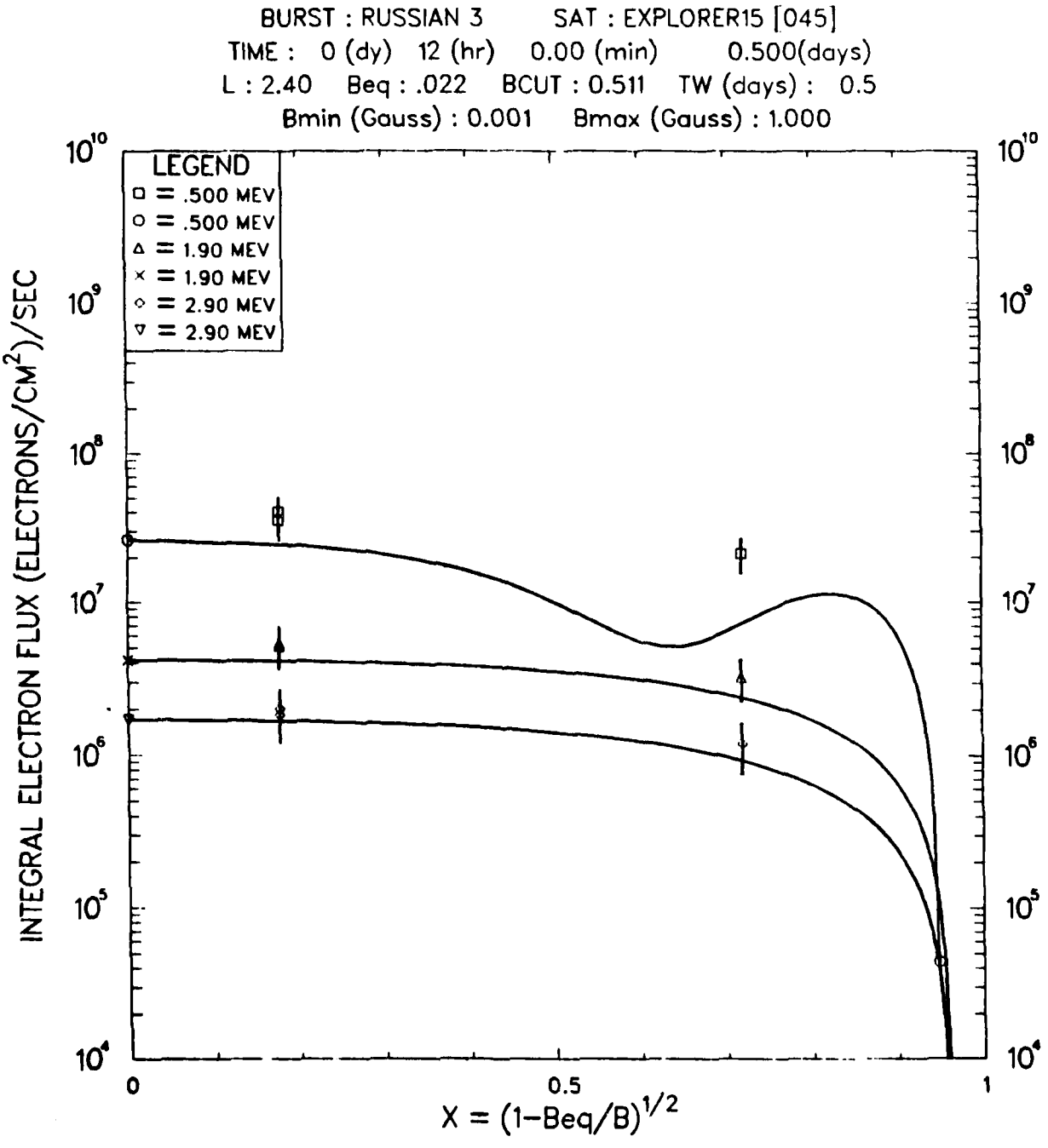

Figure 13(b). Temporal Progression of Raw Data and Fitted Flux Curves at $L = 2.4$ for Russian 3 Burst (r_n freely varying).

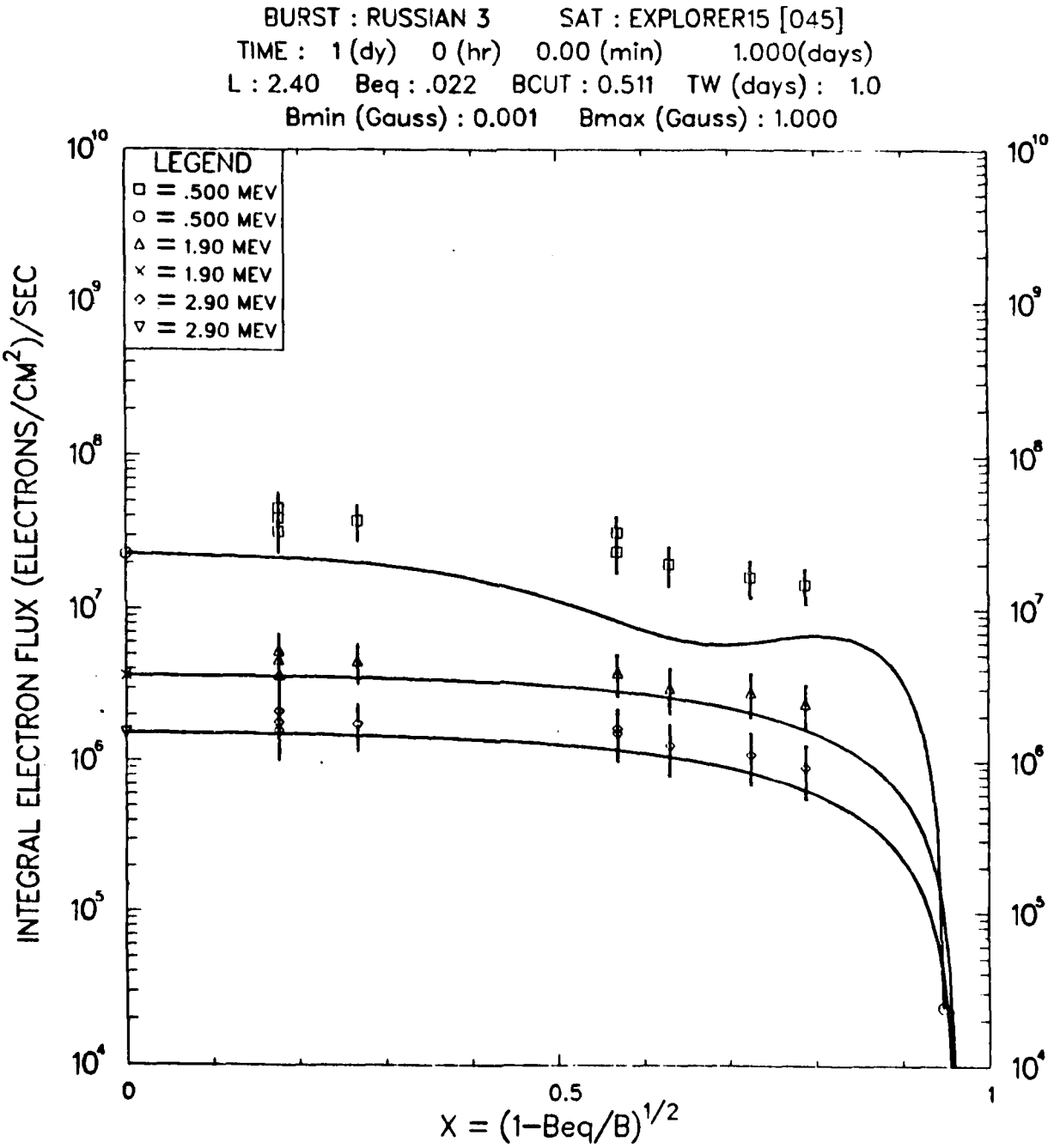

Figure 13(c). Temporal Progression of Raw Data and Fitted Flux Curves at $L = 2.4$ for Russian 3 Burst (τ_n freely varying).

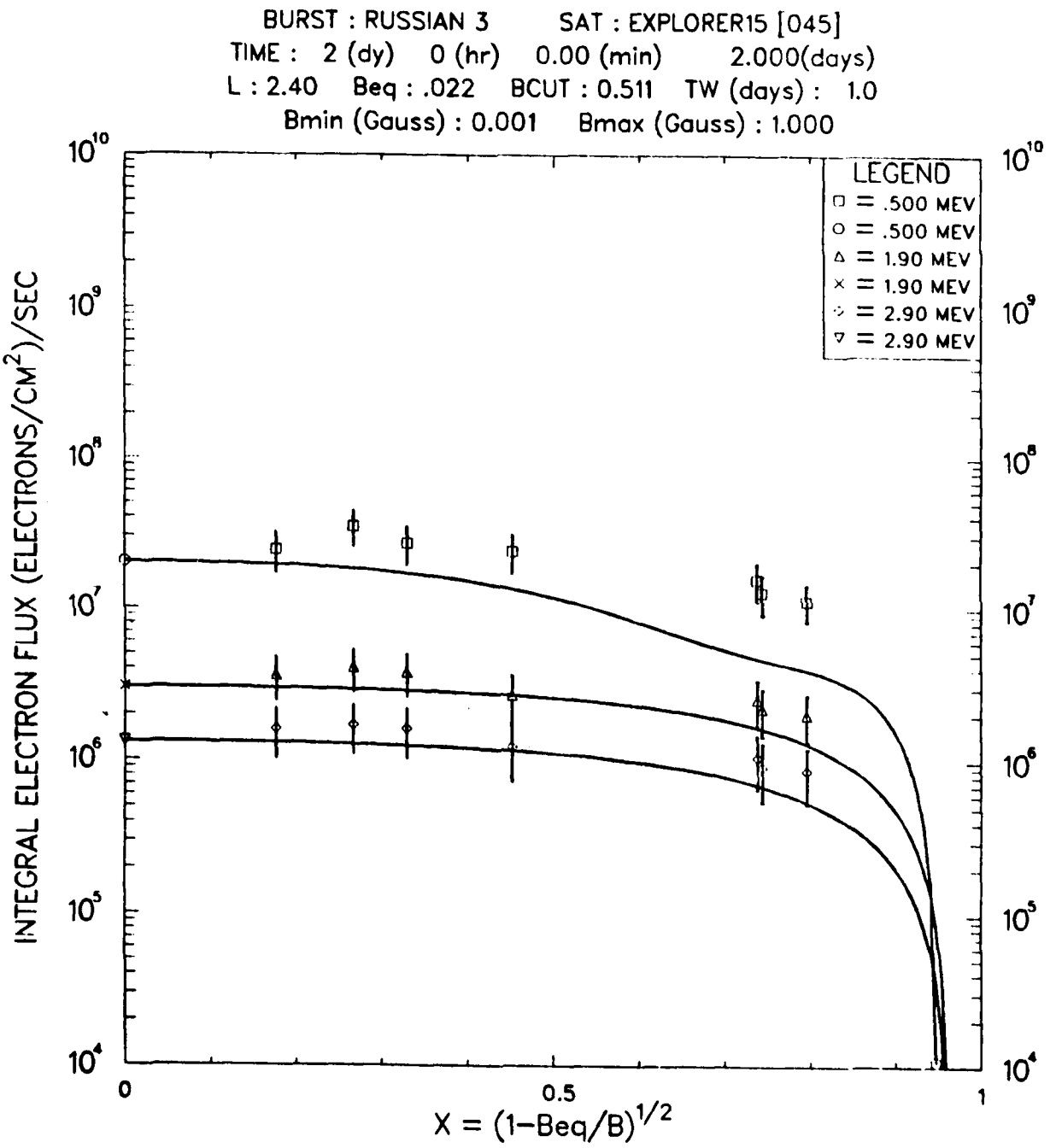

Figure 13(d). Temporal Progression of Raw Data and Fitted Flux Curves at $L = 2.4$ for Russian 3 Burst (r_n freely varying).

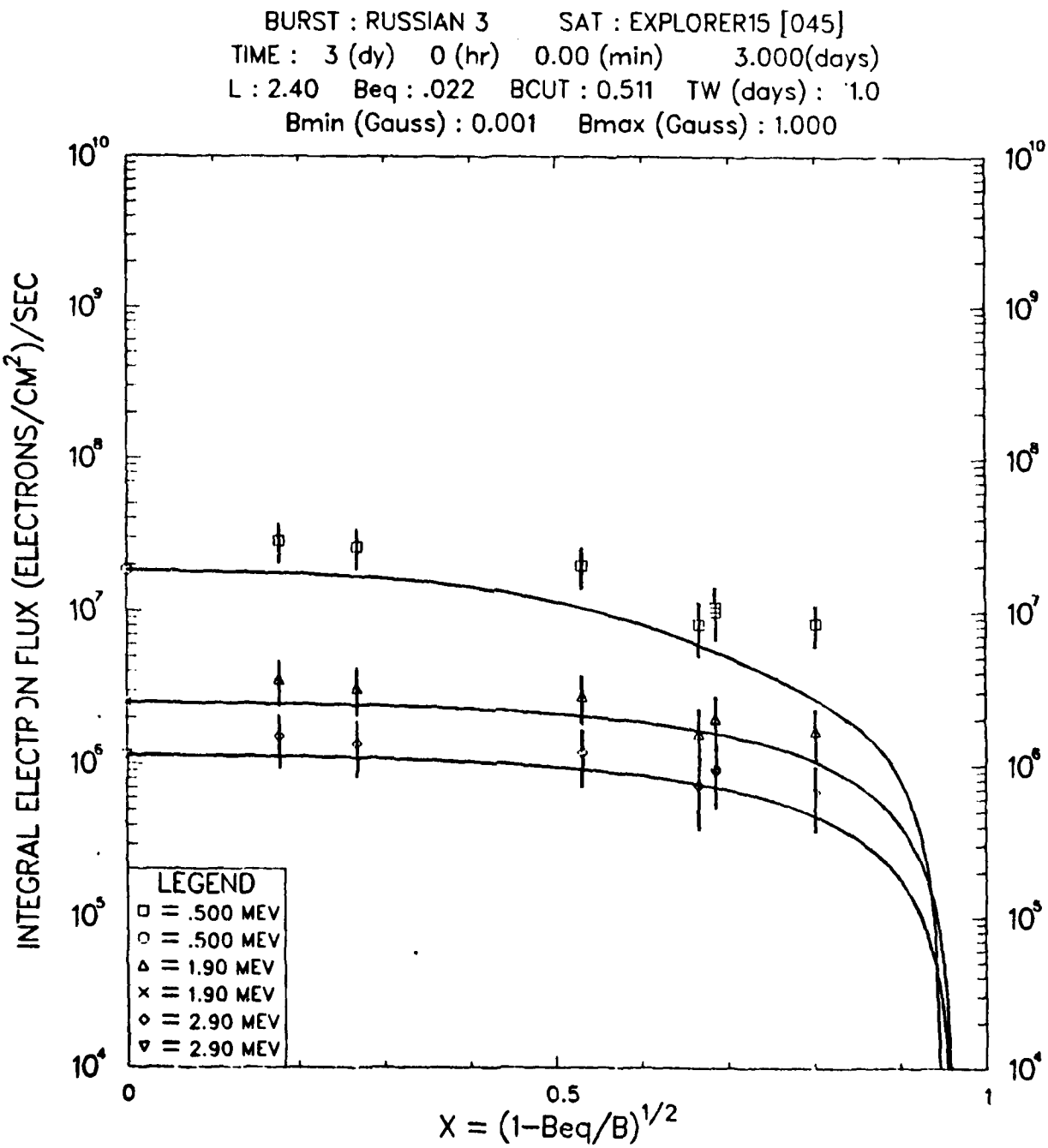

Figure 13(e). Temporal Progression of Raw Data and Fitted Flux Curves at $L = 2.4$ for Russian 3 Burst (τ_n freely varying).

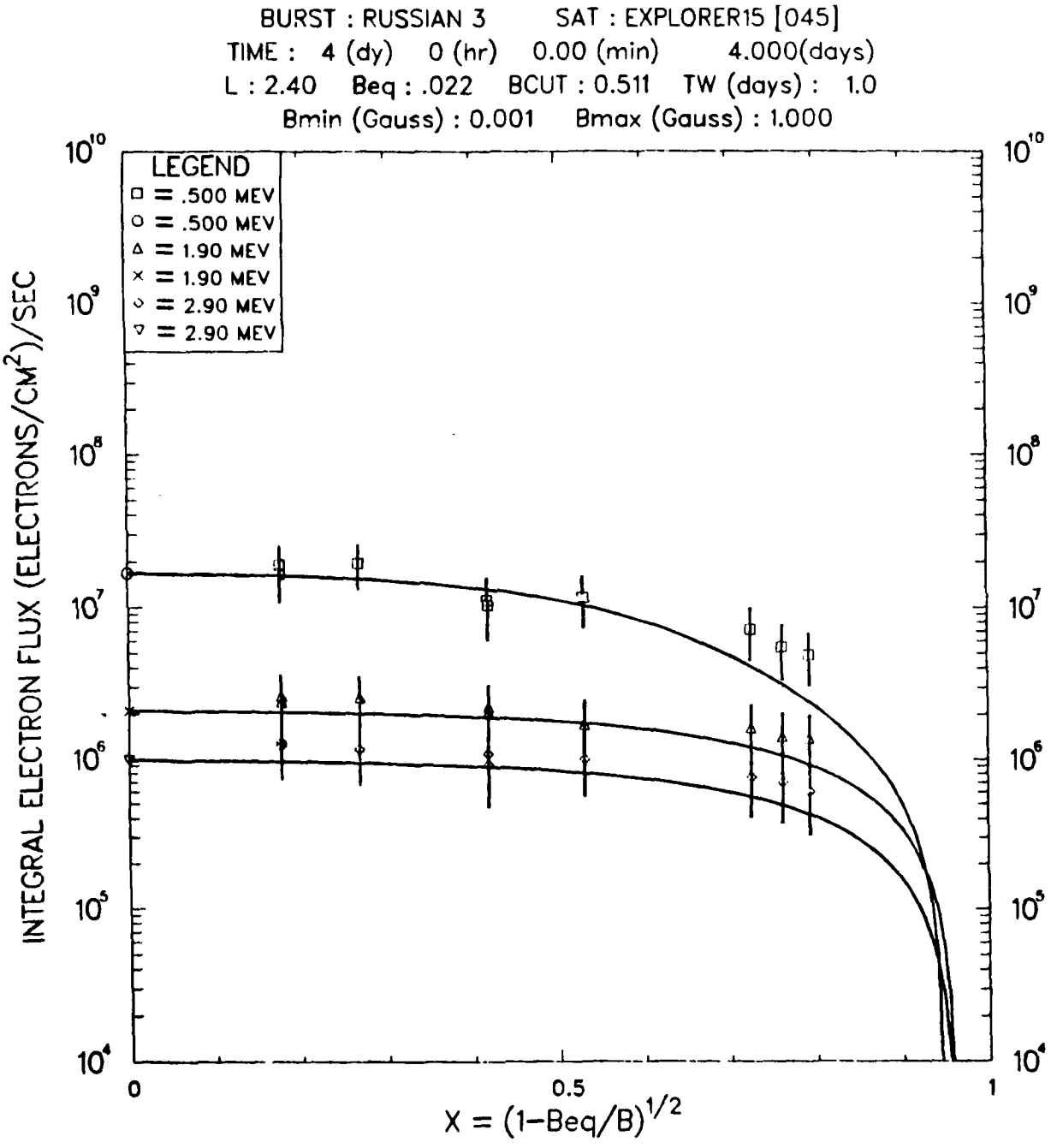

Figure 13(f). Temporal Progression of Raw Data and Fitted Flux Curves at $L = 2.4$ for Russian 3 Burst (τ_n freely varying).

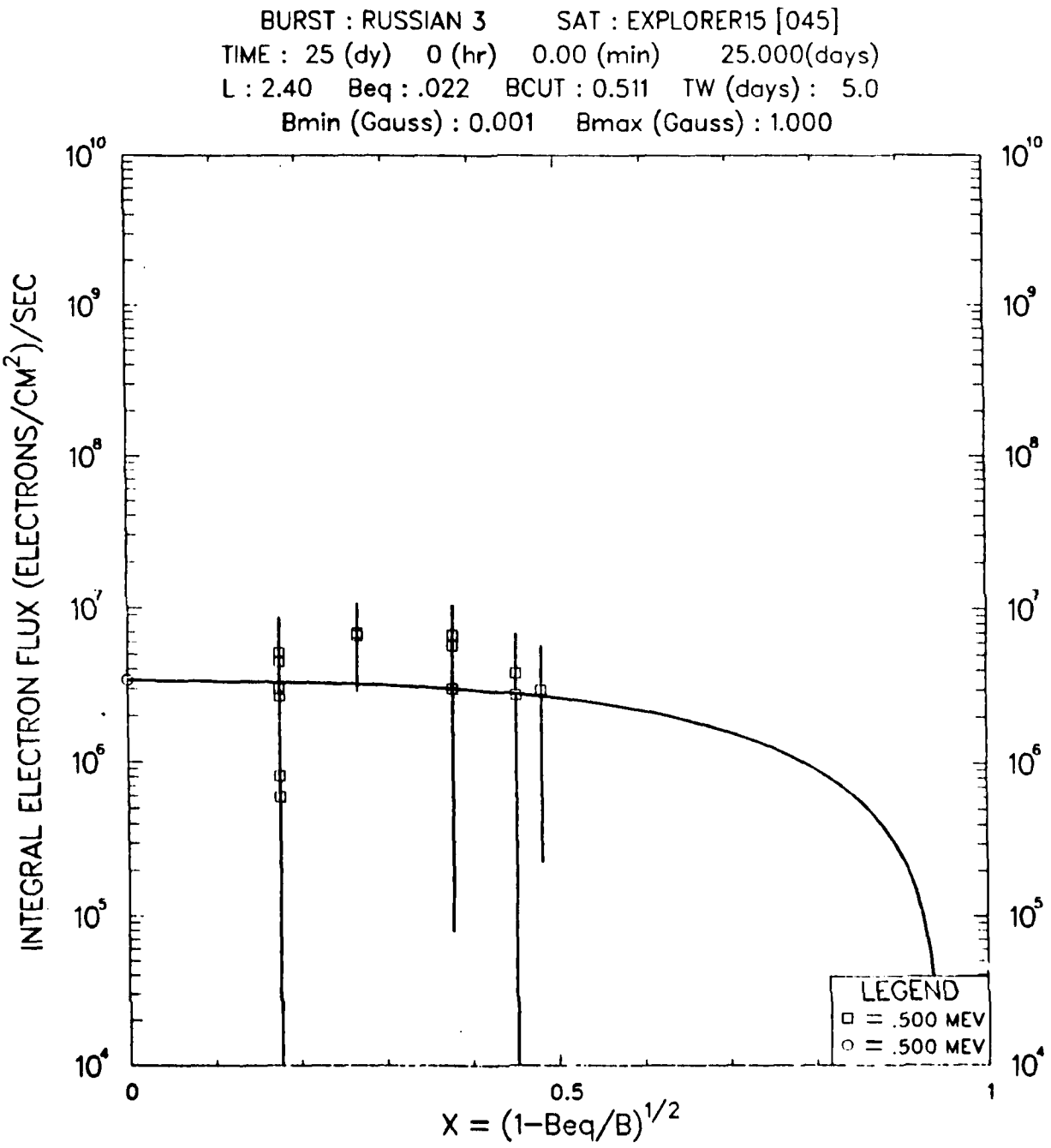

Figure 13(g). Temporal Progression of Raw Data and Fitted Flux Curves at $L = 2.4$ for Russian 3 Burst (r_n freely varying).

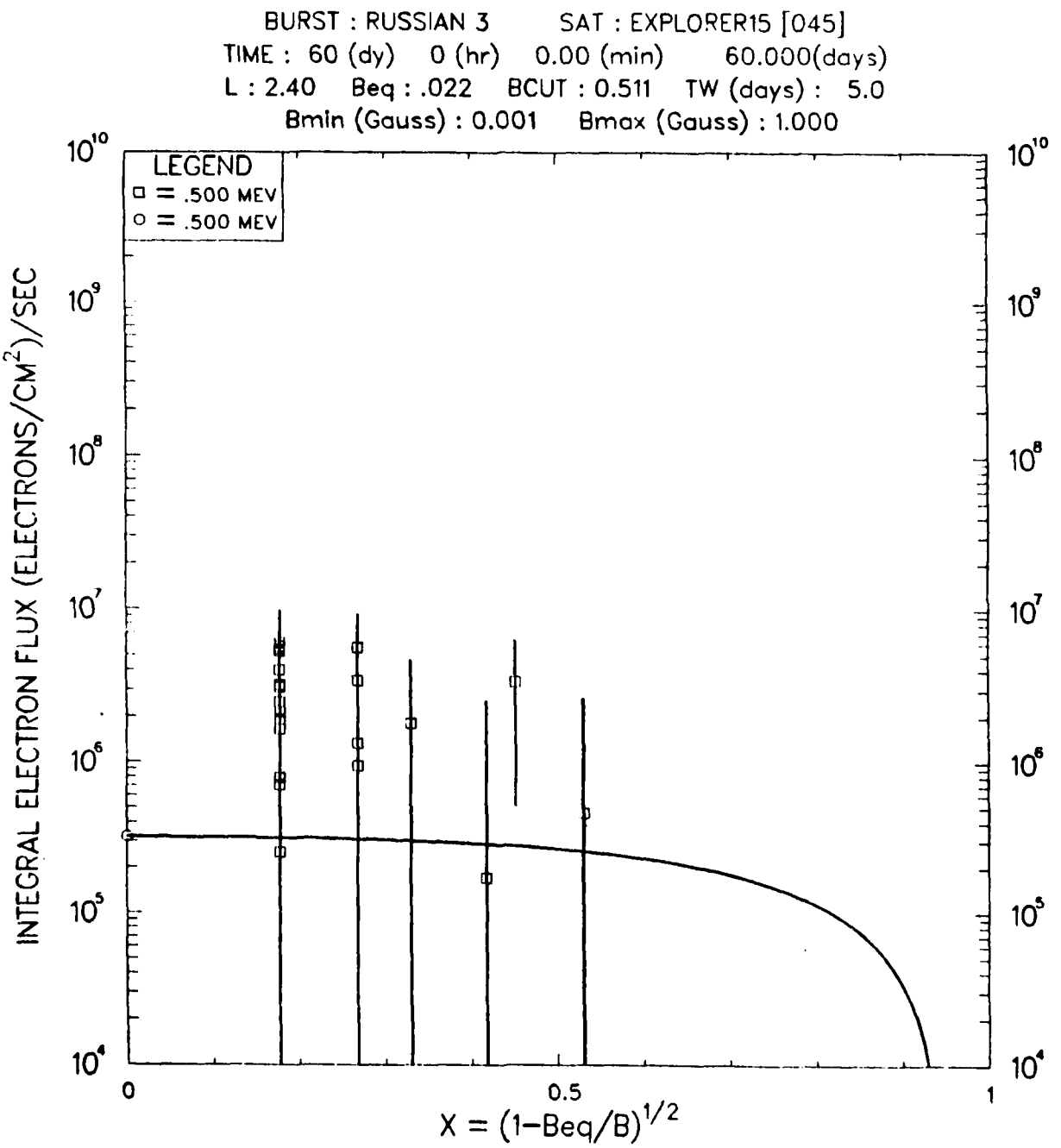

Figure 13(h). Temporal Progression of Raw Data and Fitted Flux Curves at $L = 2.4$ for Russian 3 Burst (r_n freely varying).

AD-A127 324 ELECTRON LOSSES FROM THE MAGNETOSPHERE(U) AIR FORCE INST OF TECH WRIGHT-PATTERSON AFB OH SCHOOL OF ENGINEERING R S DEWEY MAR 83 AFIT/GNE/PH/83M-4 2/2

UNCLASSIFIED F/G 8/14 NL

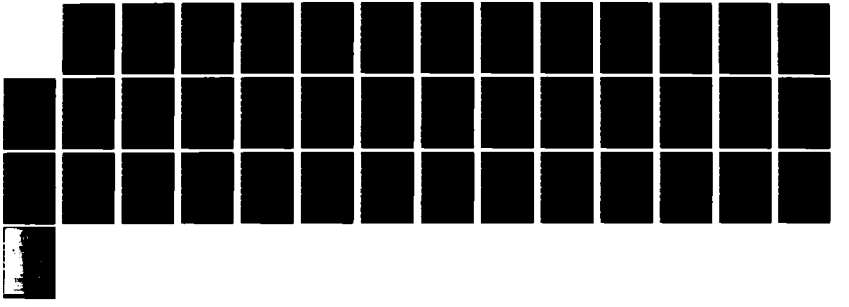

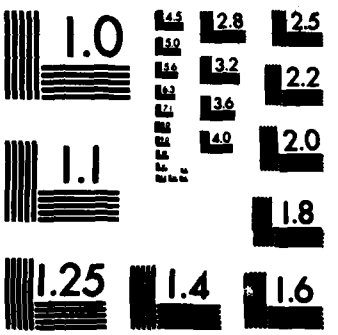

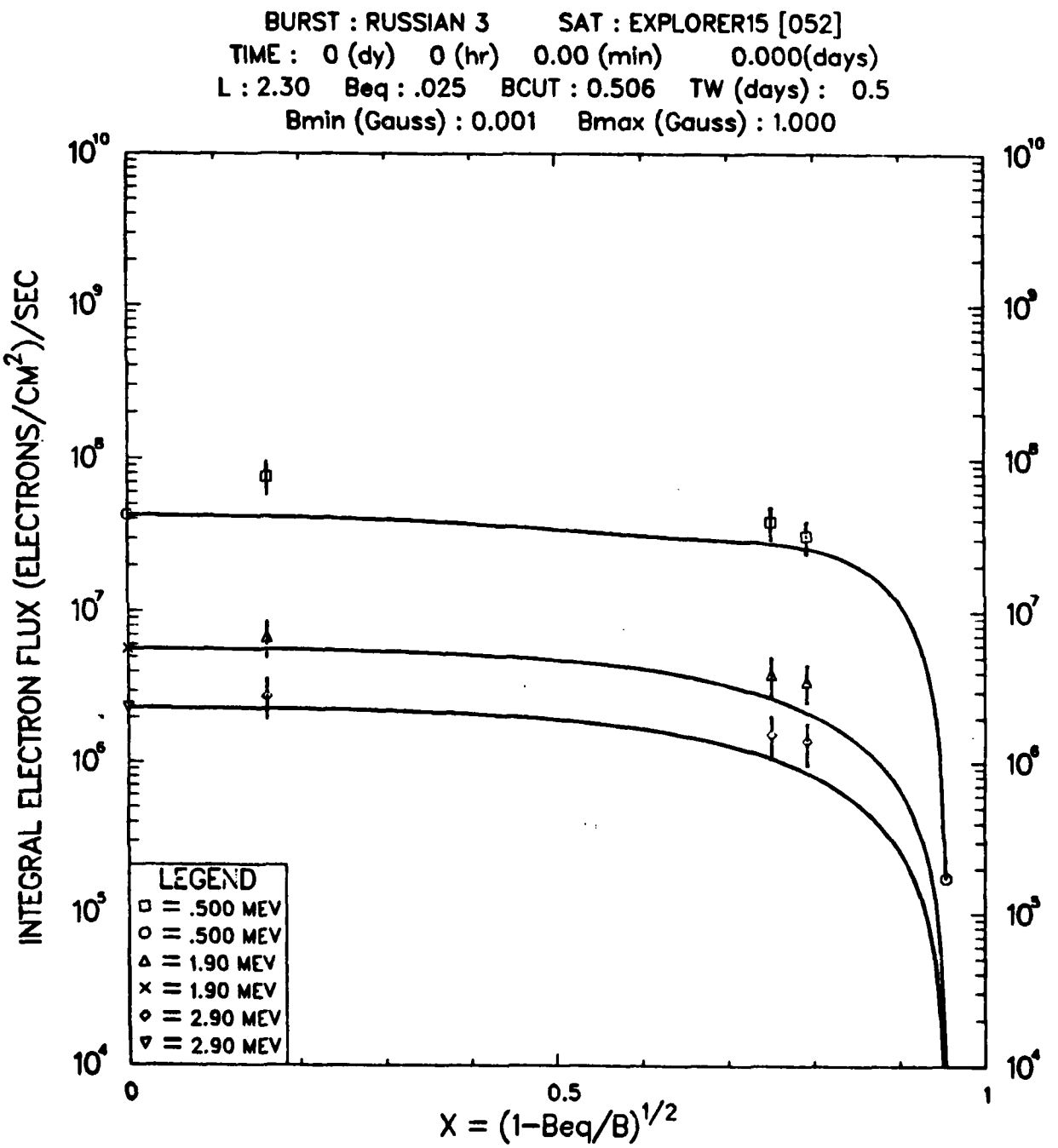

Figure 14(a). Temporal Progression of Raw Data and Fitted Flux Curves at $L = 2.3$ for Russian 3 Burst (r_n fixed 1:1/9:1/25).

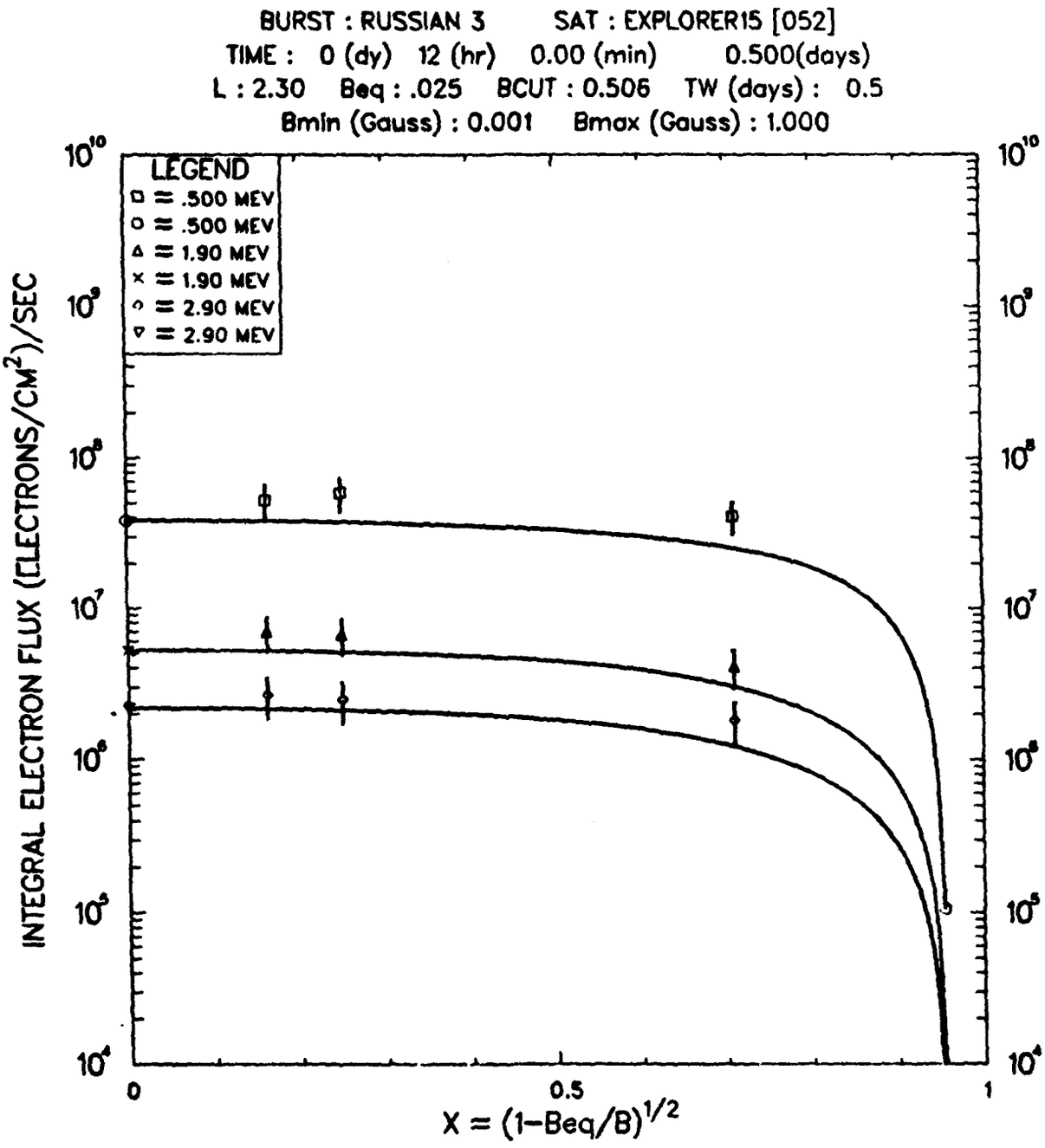

Figure 14(b). Temporal Progression of Raw Data and Fitted Flux Curves at $L = 2.3$ for Russian 3 Burst (τ_n fixed 1:1/9:1/25).

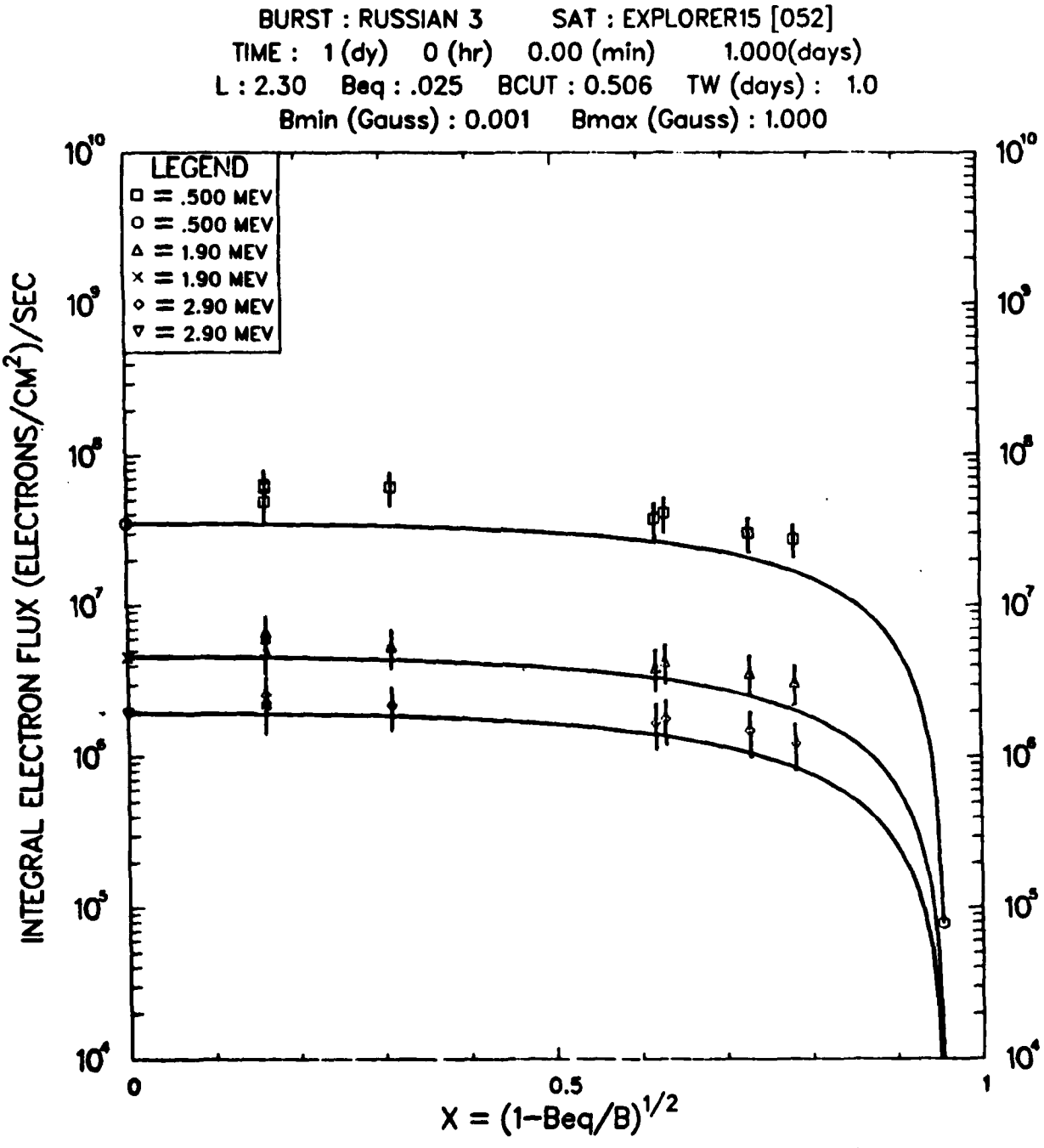

Figure 14(c). Temporal Progression of Raw Data and Fitted Flux Curves at $L = 2.3$ for Russian 3 Burst (r_n fixed 1:1/9:1/25).

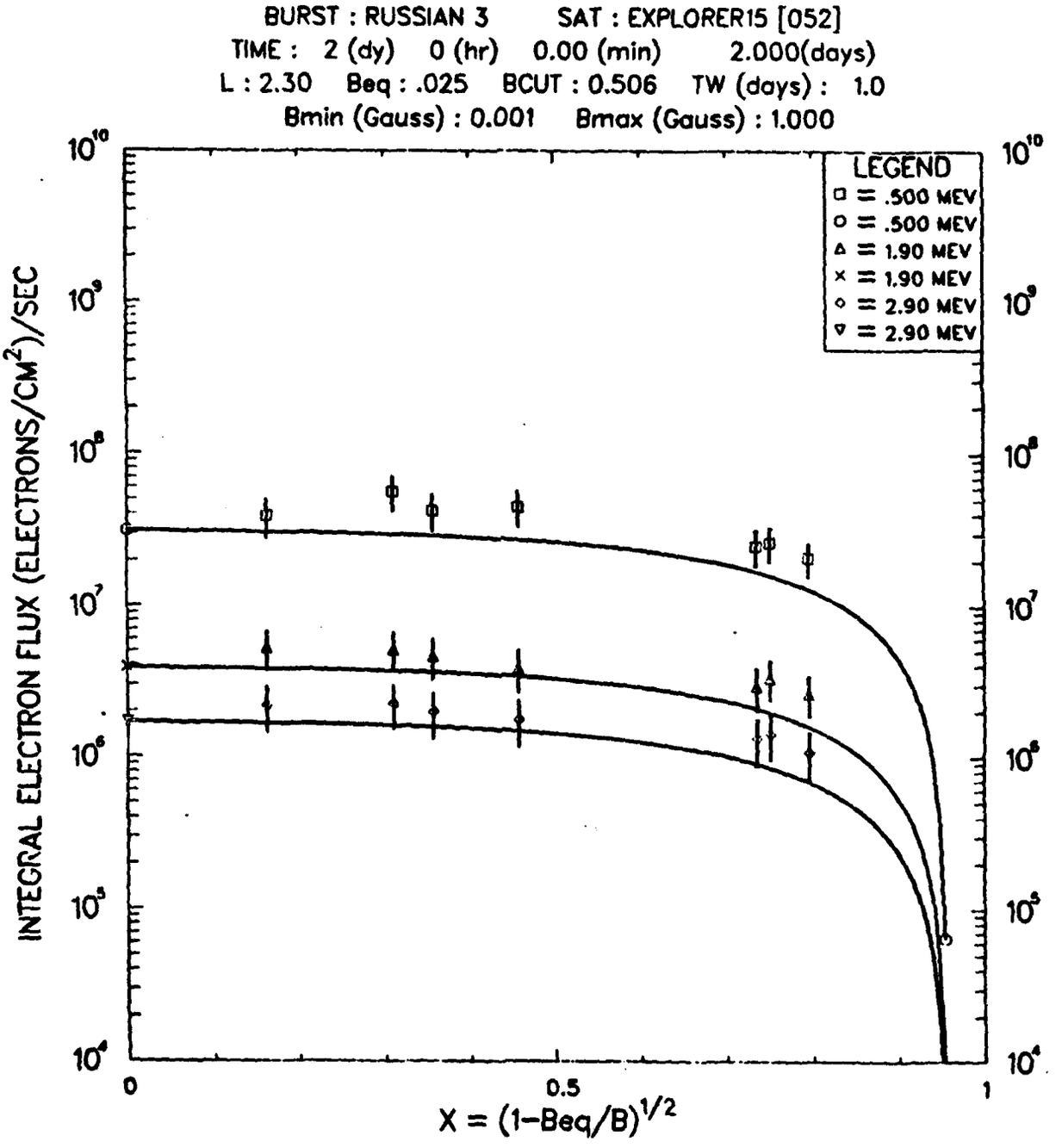

Figure 14(d). Temporal Progression of Raw Data and Fitted Flux Curves at $L = 2.3$ for Russian 3 Burst (r_n fixed 1:1/9:1/25).

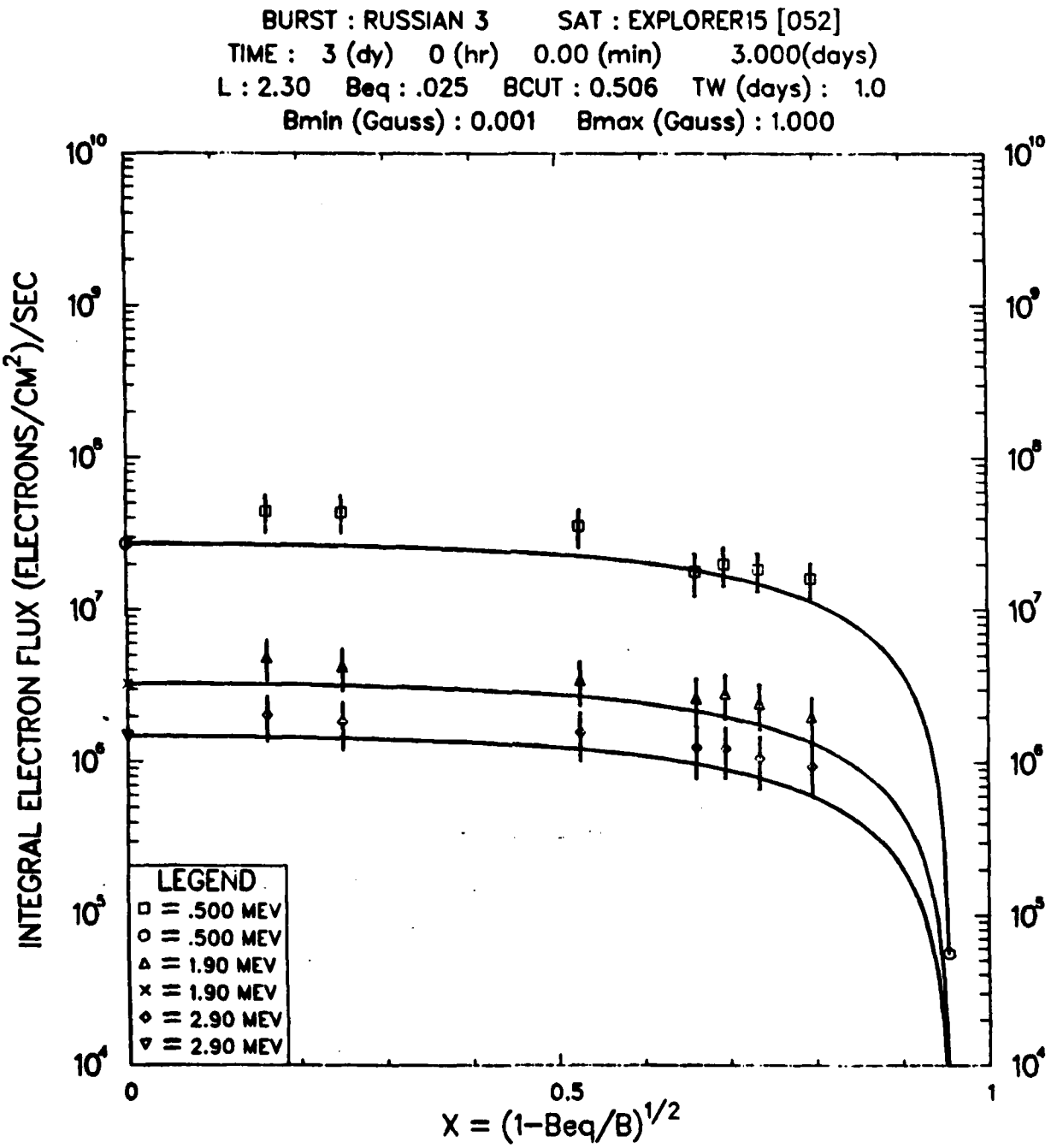

Figure 14(e). Temporal Progression of Raw Data and Fitted Flux Curves at $L = 2.3$ for Russian 3 Burst (r_n fixed 1:1/9:1/25).

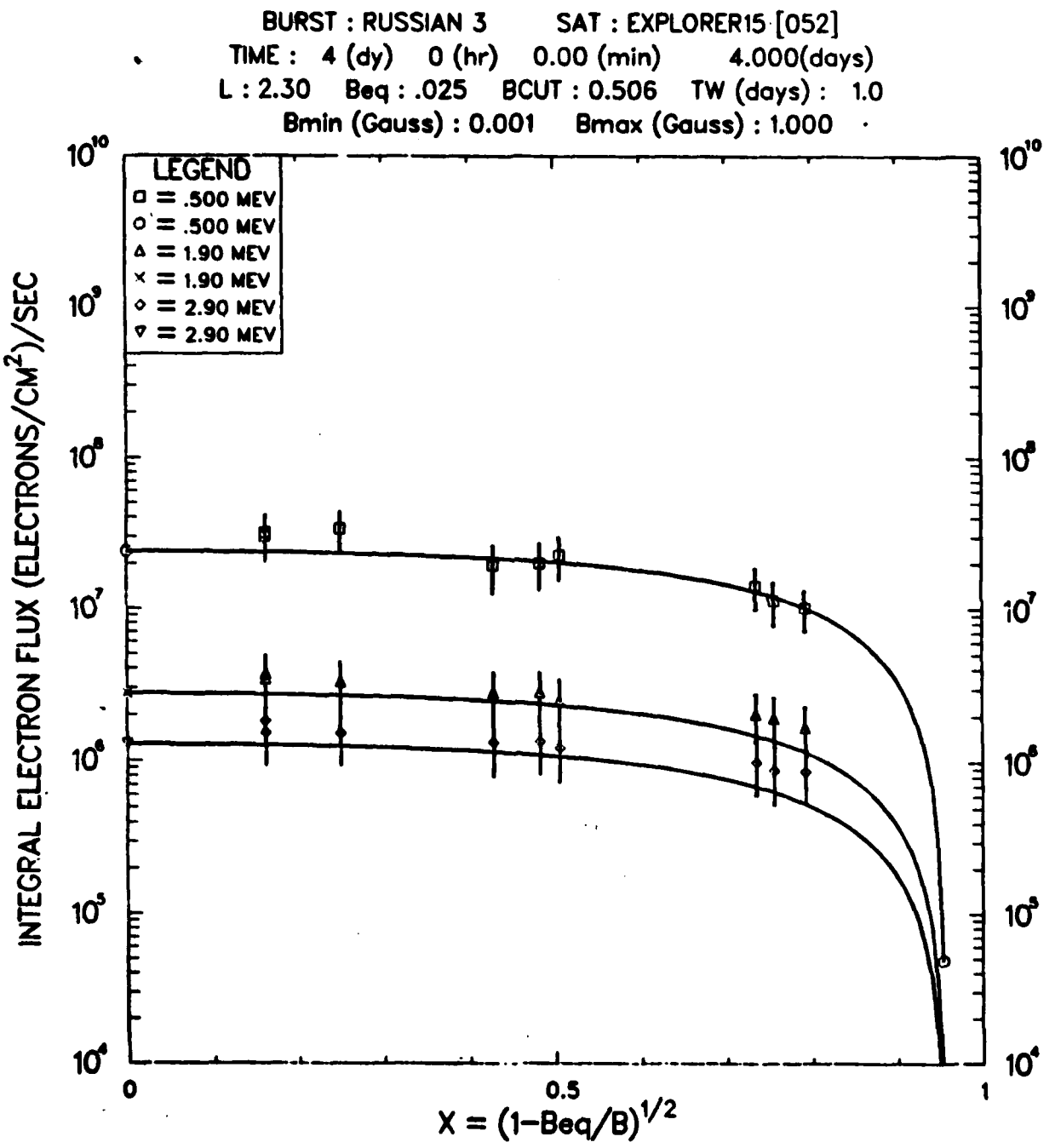

Figure 14(f). Temporal Progression of Raw Data and Fitted Flux Curves at $L = 2.3$ for Russian 3 Burst (r_n fixed 1:1/9:1/25).

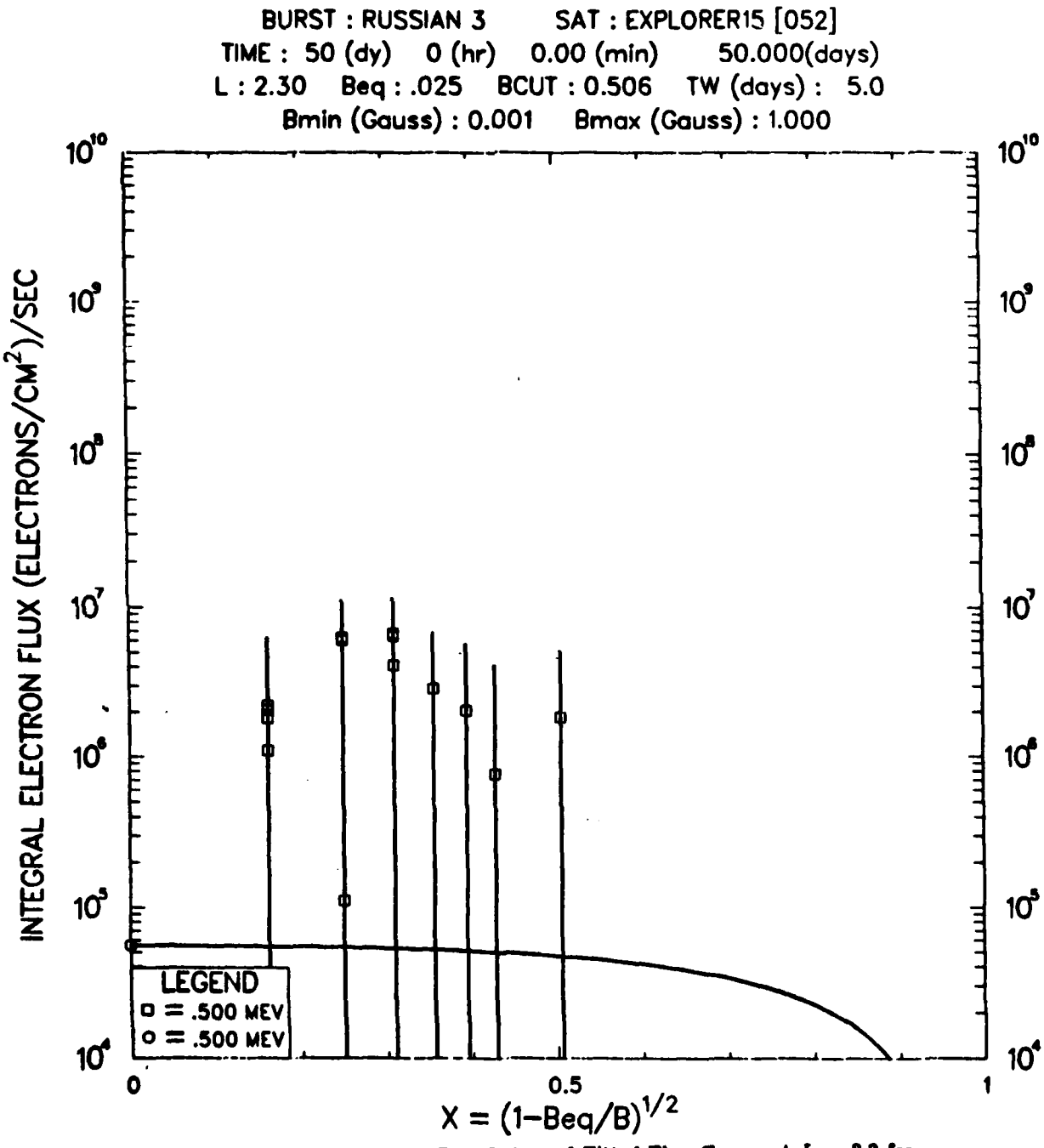

Figure 14(g). Temporal Progression of Raw Data and Fitted Flux Curves at $L = 2.3$ for Russian 3 Burst (r_n fixed 1:1/9:1/25).

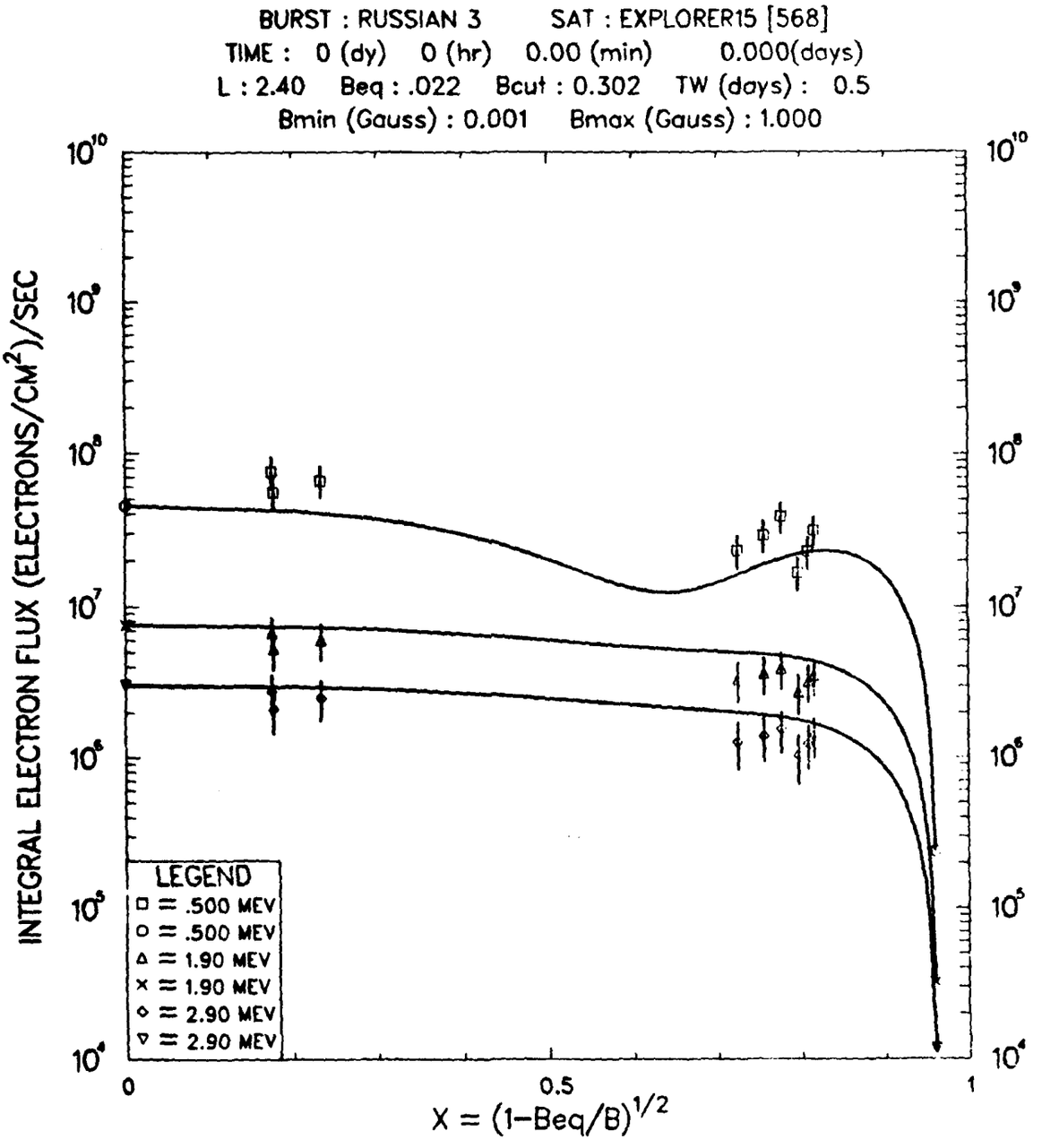

Figure 15(a). Temporal Progression of Raw Data and Fitted Flux Curves at $L = 2.4$ for Russian 3 Burst (r_n freely varying with physical contraints).

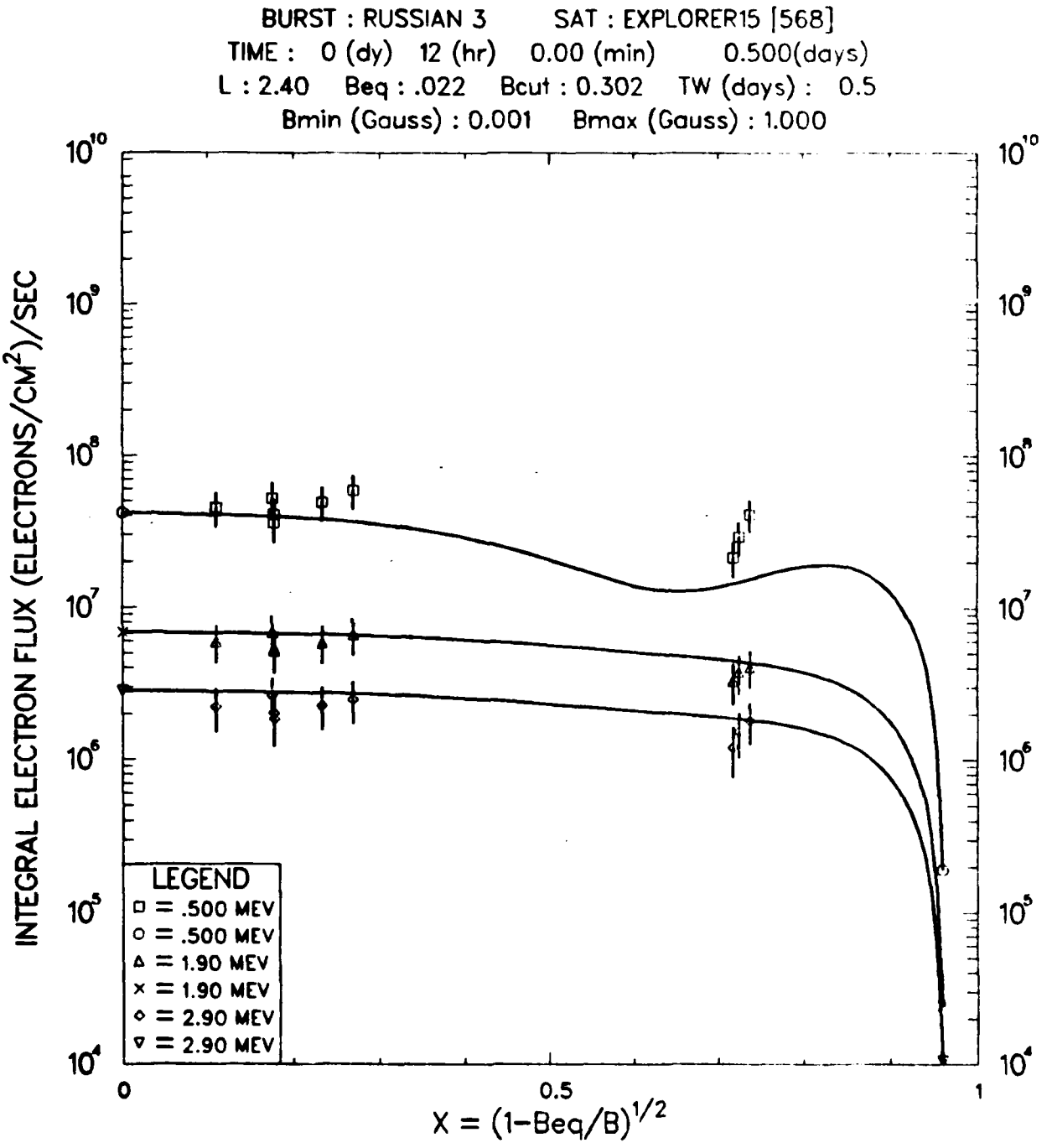

Figure 15(b). Temporal Progression of Raw Data and Fitted Flux Curves at $L = 2.4$ for Russian 3 Burst (r_o freely varying with physical contraints).

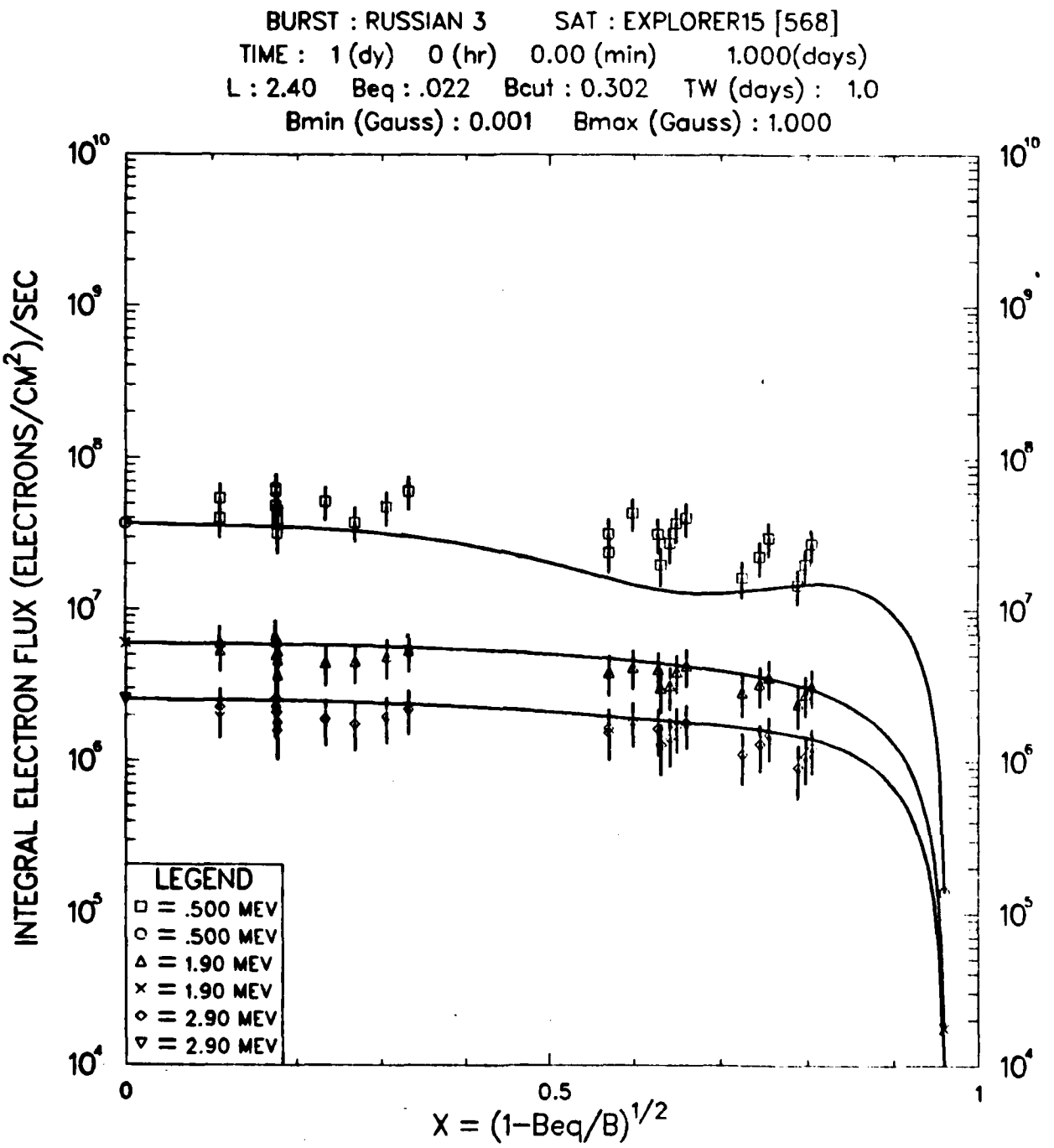

Figure 15(c). Temporal Progression of Raw Data and Fitted Flux Curves at $L = 2.4$ for Russian 3 Burst (τ_n freely varying with physical contraints).

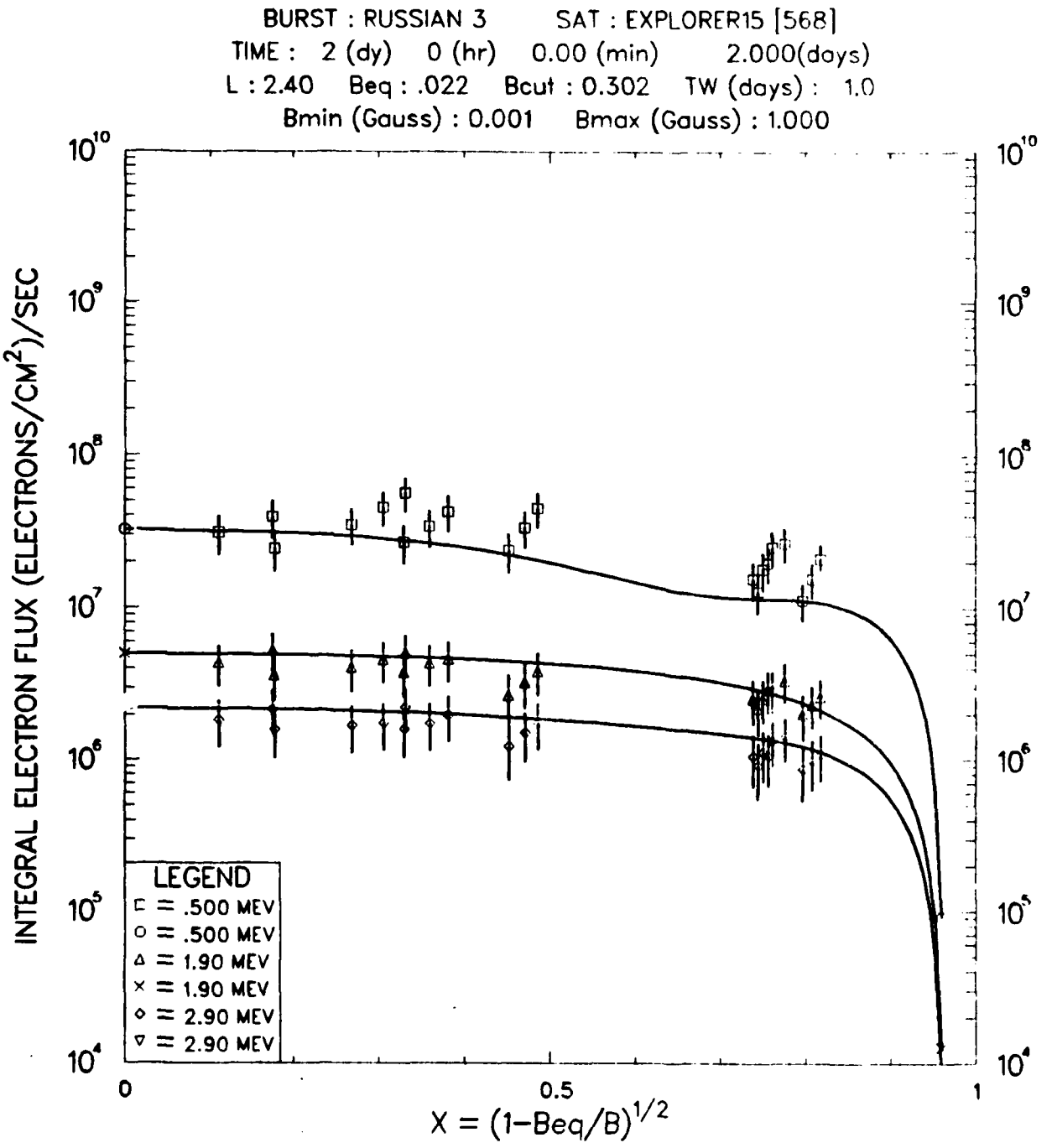

Figure 15(d). Temporal Progression of Raw Data and Fitted Flux Curves at $L = 2.4$ for Russian 3 Burst (r_n freely varying with physical contraints).

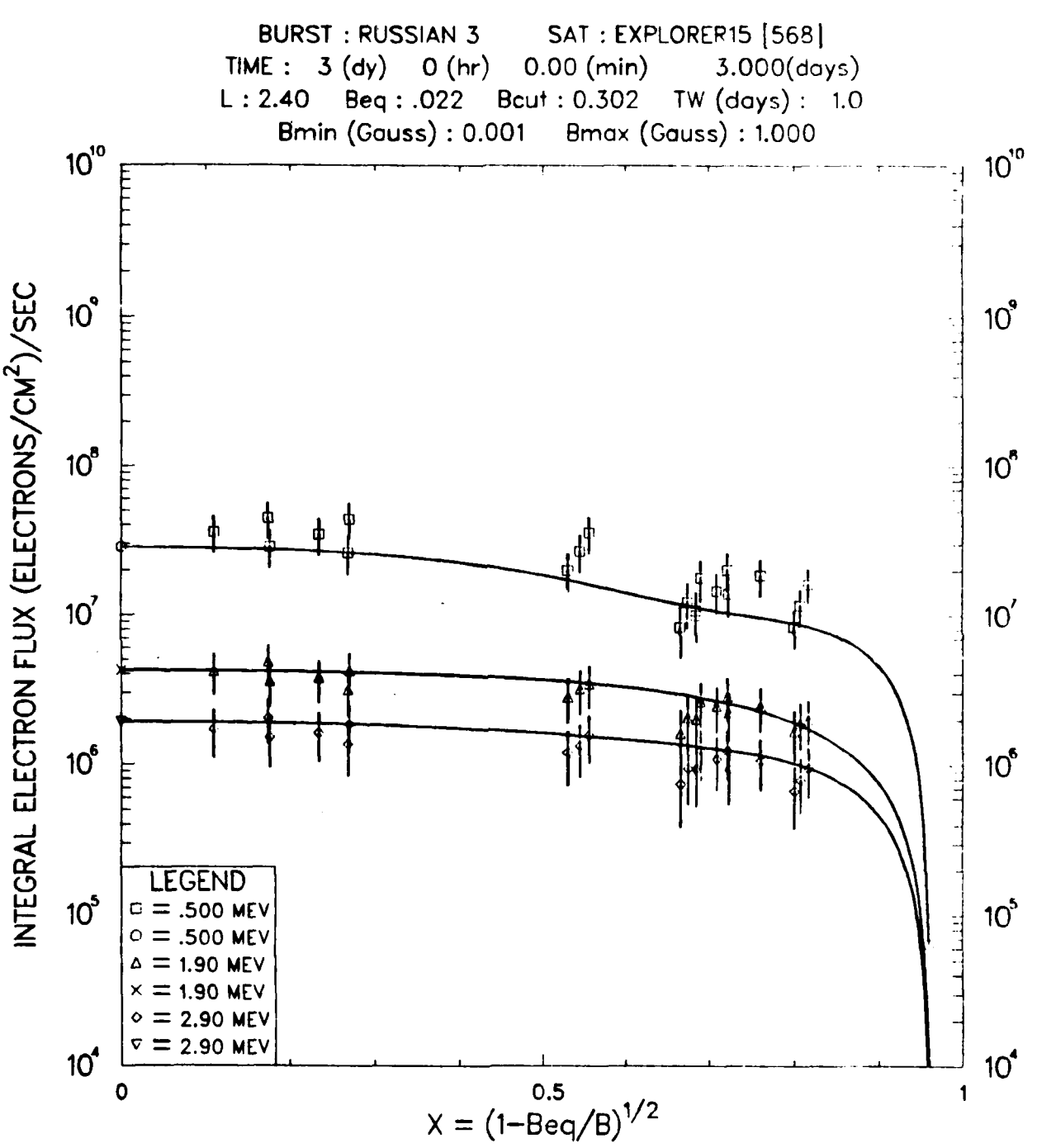

Figure 15(e). Temporal Progression of Raw Data and Fitted Flux Curves at $L = 2.4$ for Russian 3 Burst (r_m freely varying with physical contraints).

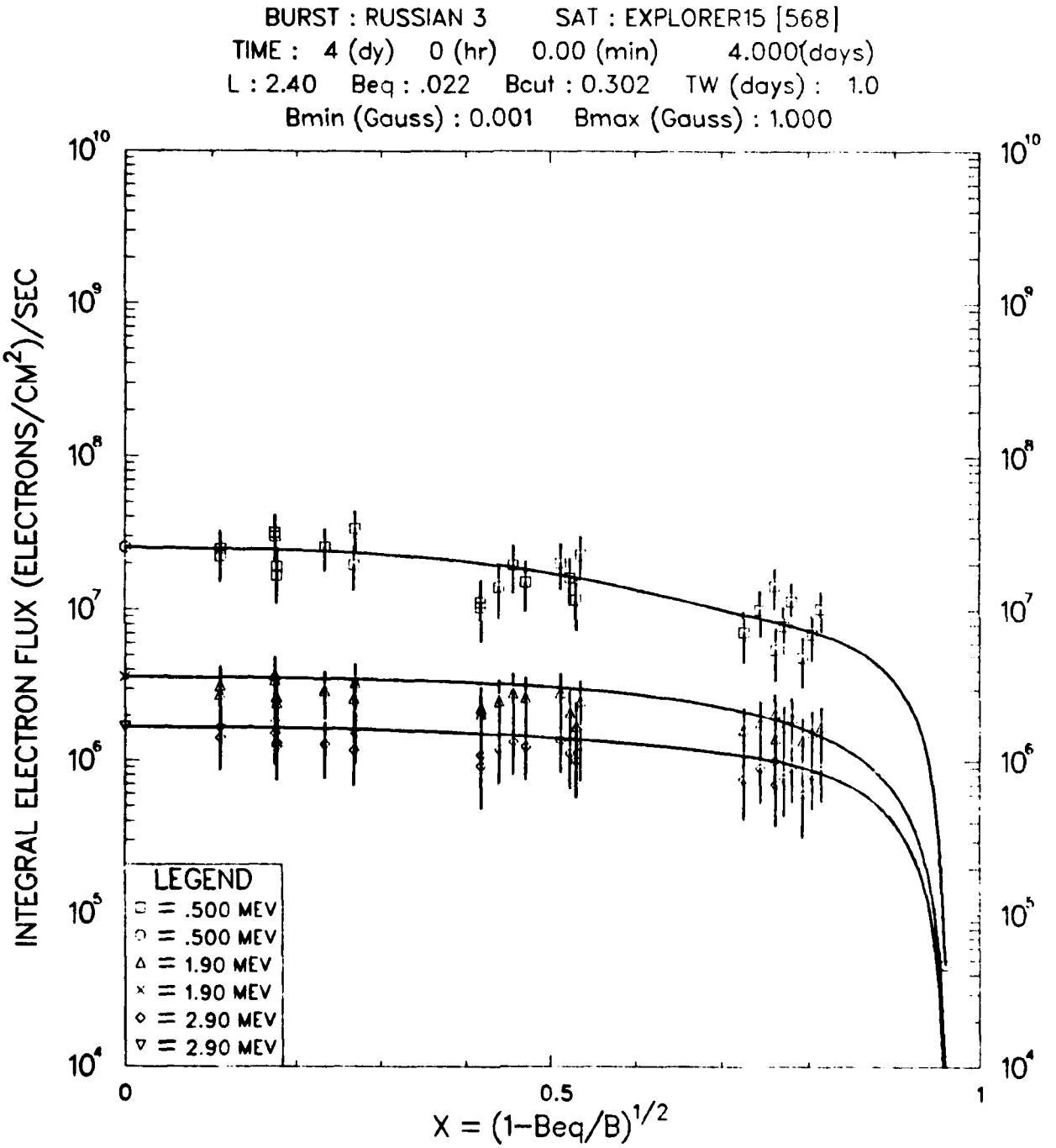

Figure 15(f). Temporal Progression of Raw Data and Fitted Flux Curves at $L = 2.4$ for Russian 3 Burst (r_0 freely varying with physical contraints).

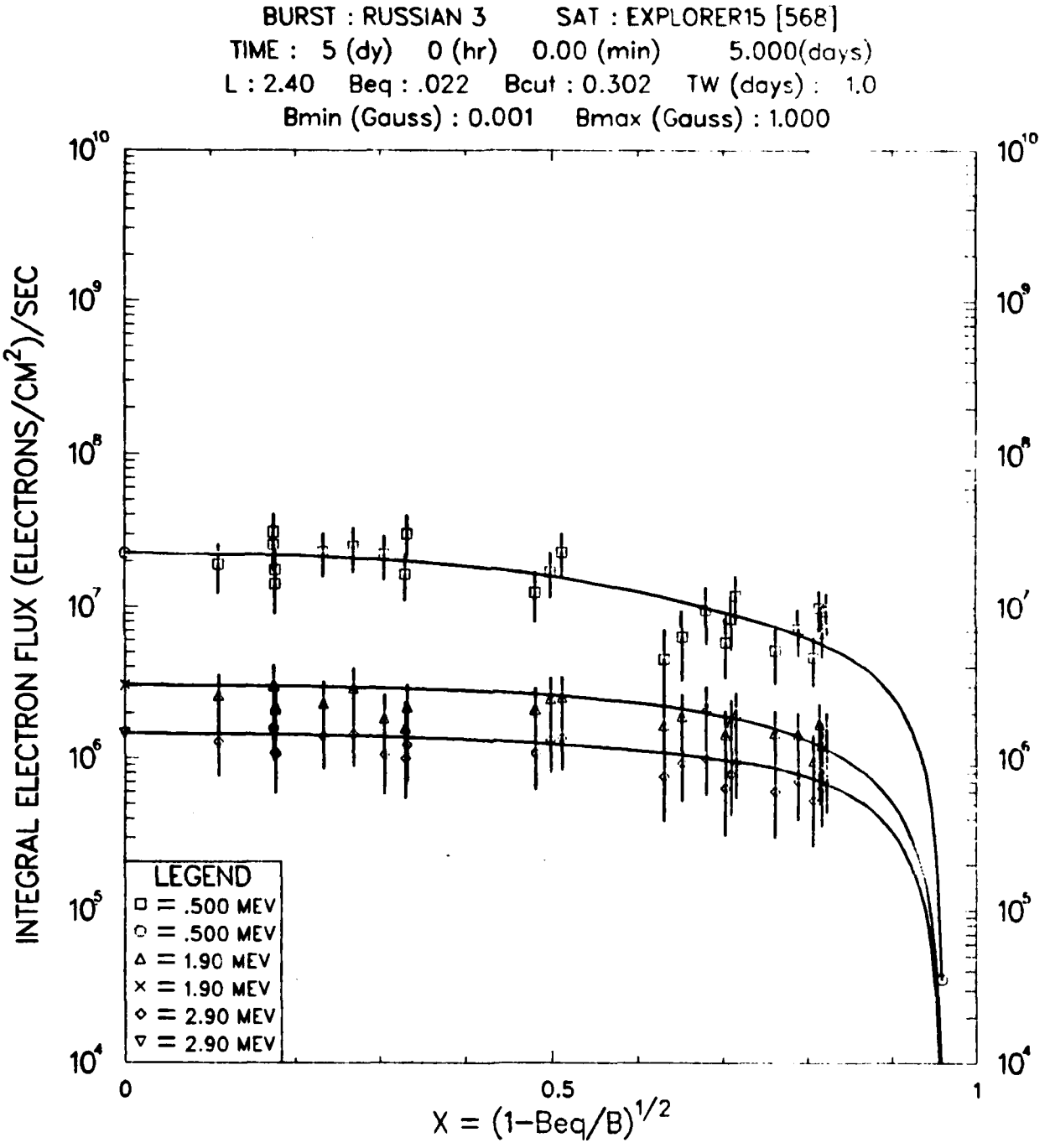

Figure 15(g). Temporal Progression of Raw Data and Fitted Flux Curves at $L = 2.4$ for Russian 3 Burst (r_n freely varying with physical contraints).

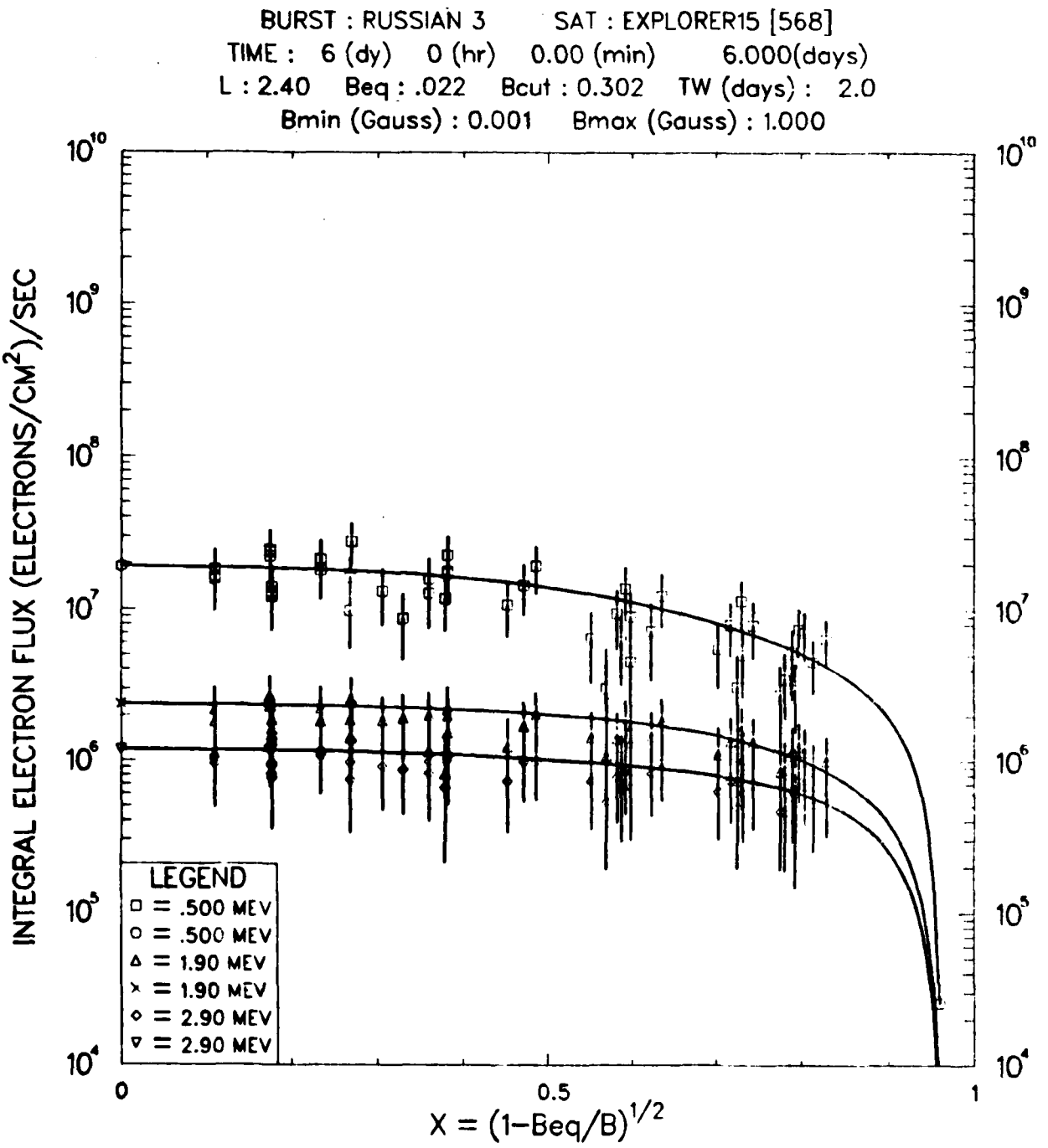

Figure 15(h). Temporal Progression of Raw Data and Fitted Flux Curves at $L = 2.4$ for Russian 3 Burst (r_n freely varying with physical contraints).

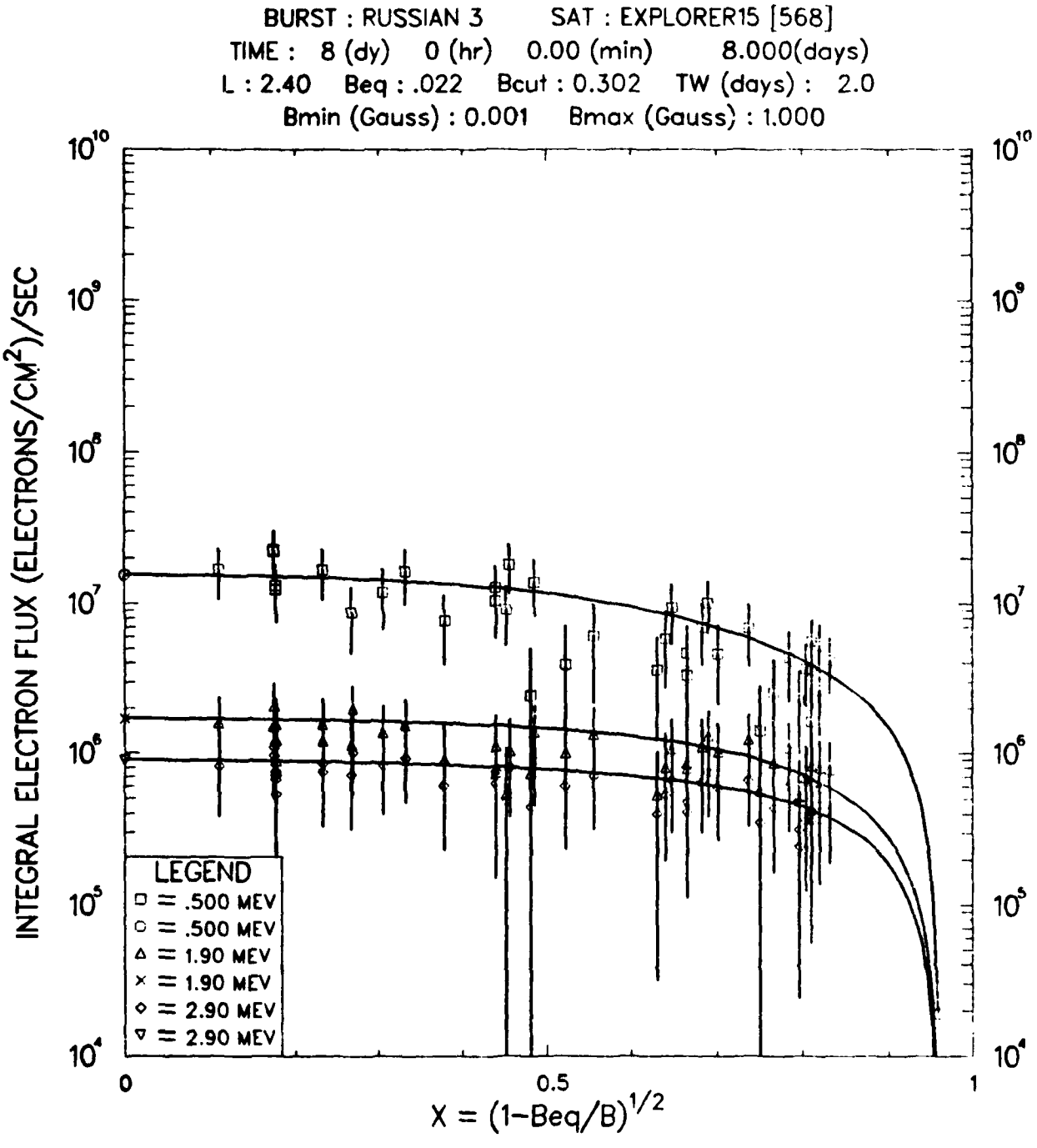

Figure 15(i). Temporal Progression of Raw Data and Fitted Flux Curves at $L = 2.4$ for Russian 3 Burst (r_n freely varying with physical contraints).

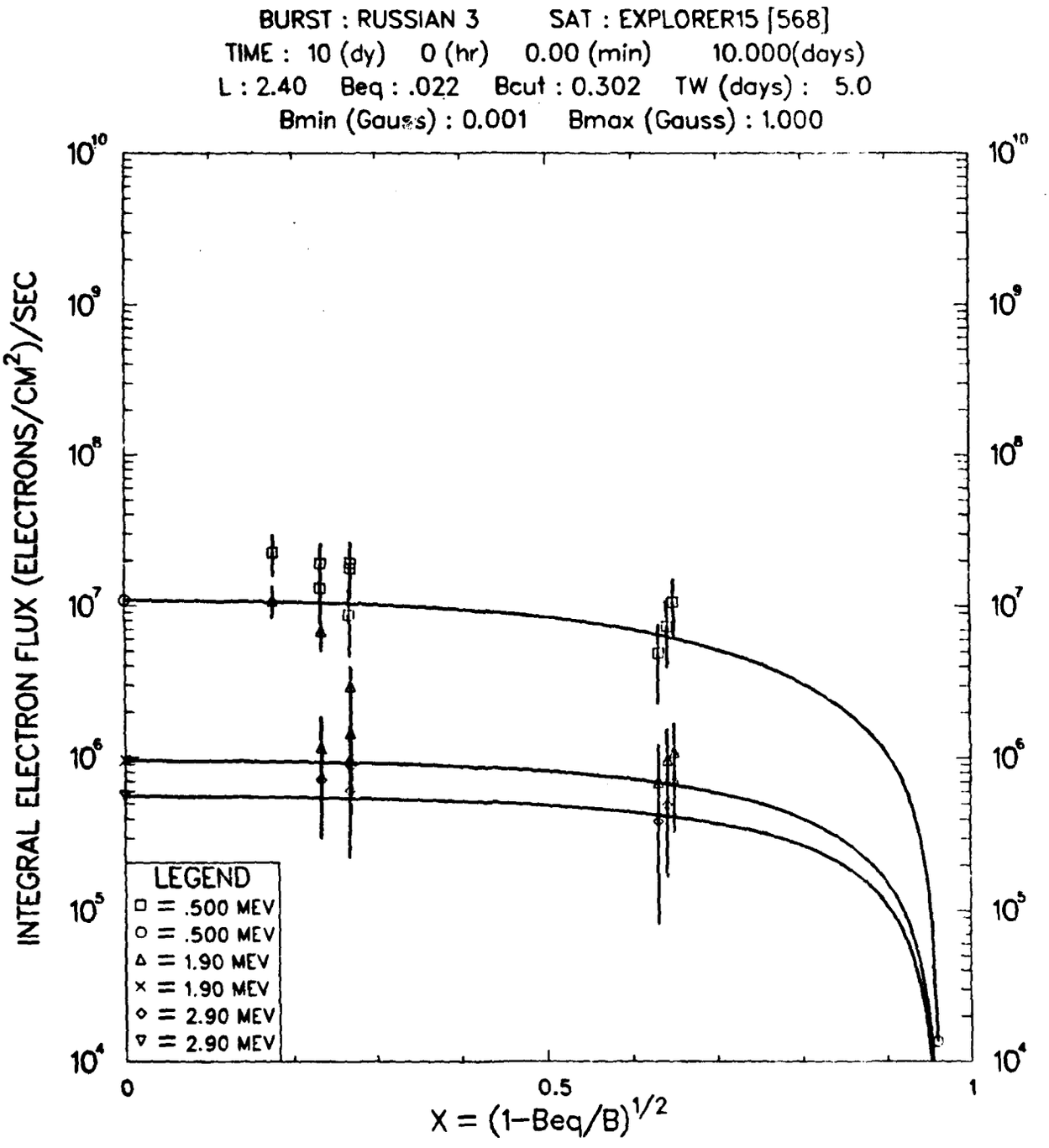

Figure 15(j). Temporal Progression of Raw Data and Fitted Flux Curves at $L = 2.4$ for Russian 3 Burst (r_n freely varying with physical contraints).

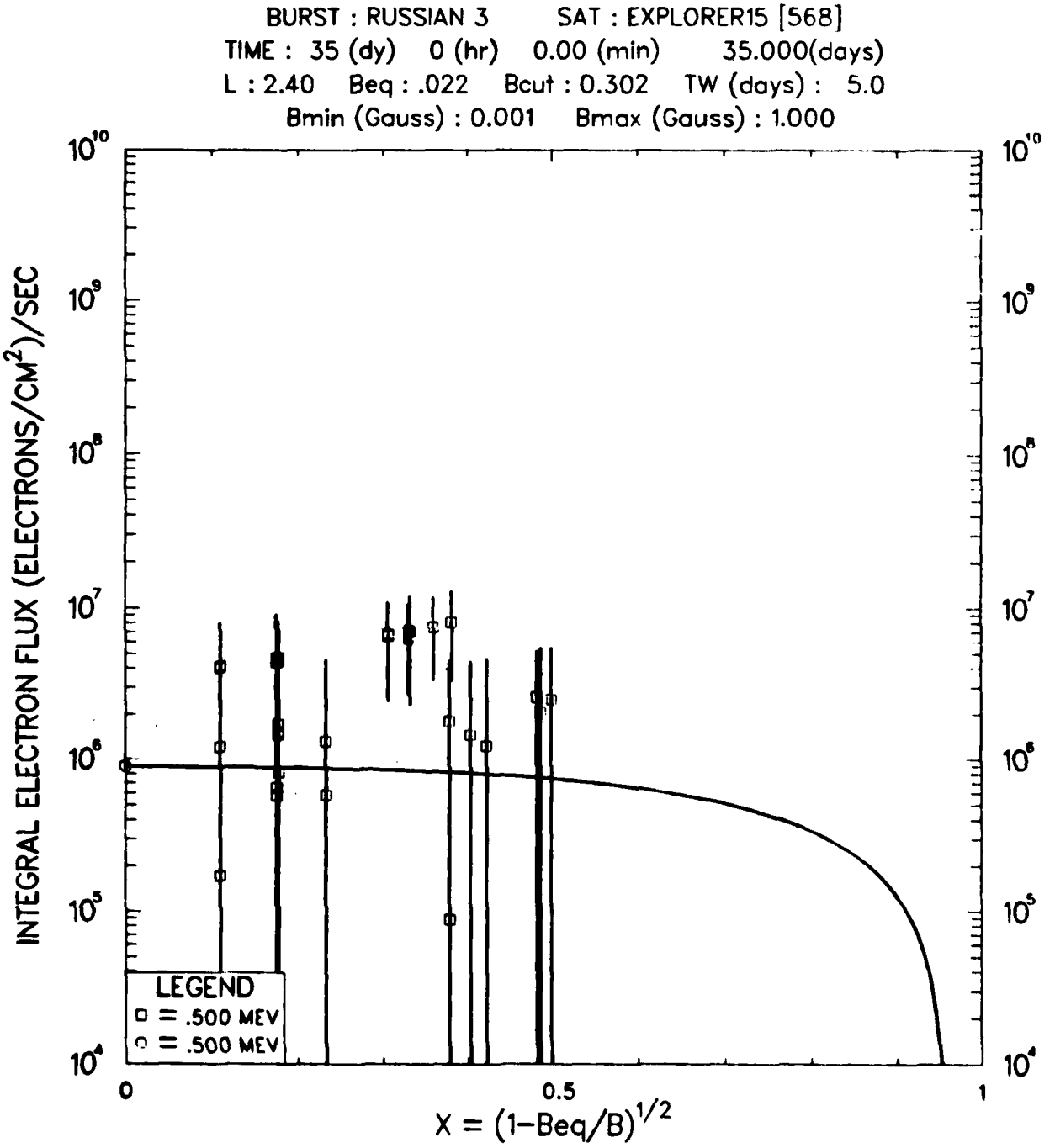

Figure 15(k). Temporal Progression of Raw Data and Fitted Flux Curves at $L = 2.4$ for Russian 3 Burst (τ_n freely varying with physical contraints).

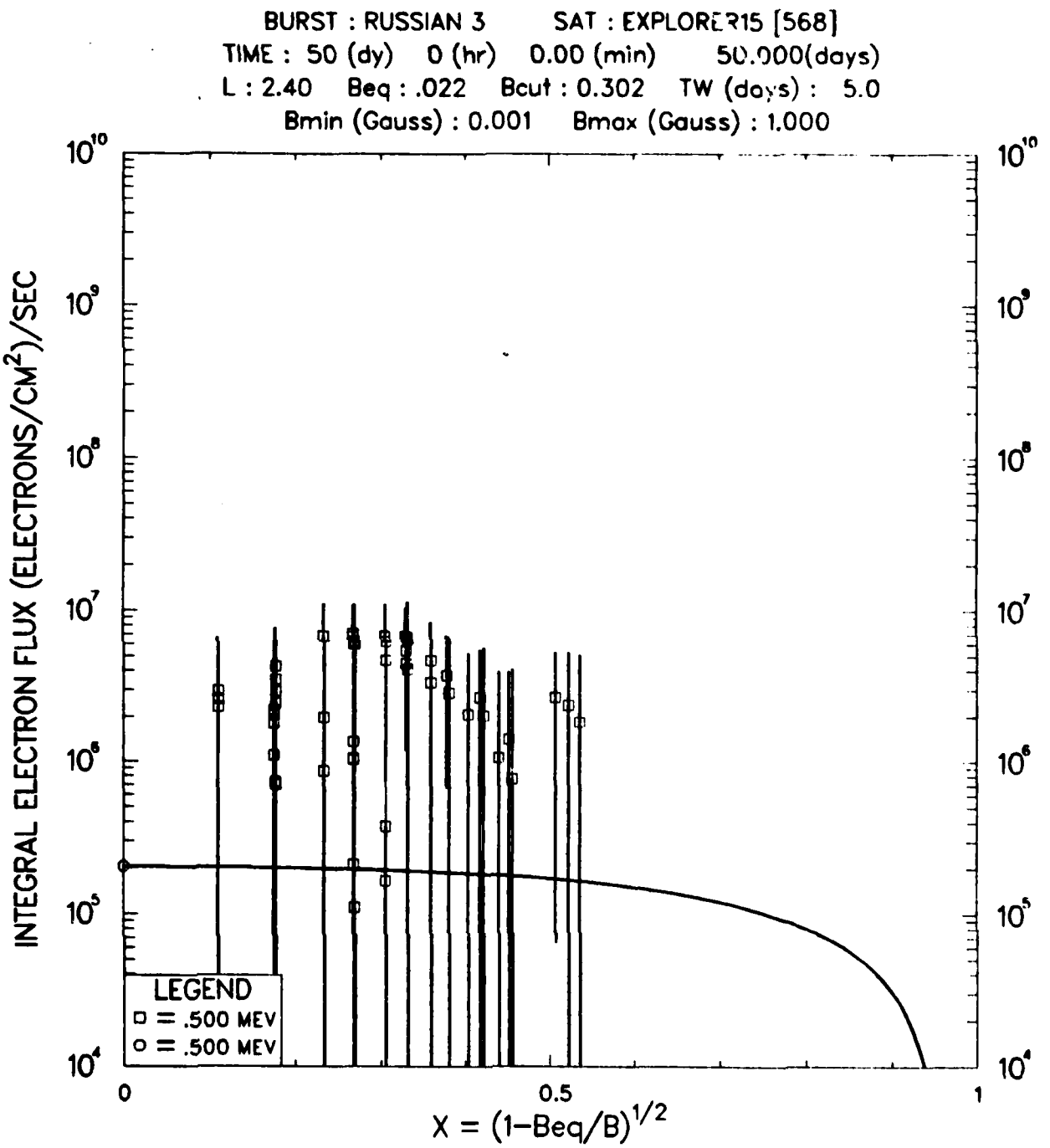

Figure 15(l). Temporal Progression of Raw Data and Fitted Flux Curves at $L = 2.4$ for Russian 3 Burst (τ_n freely varying with physical contraints).

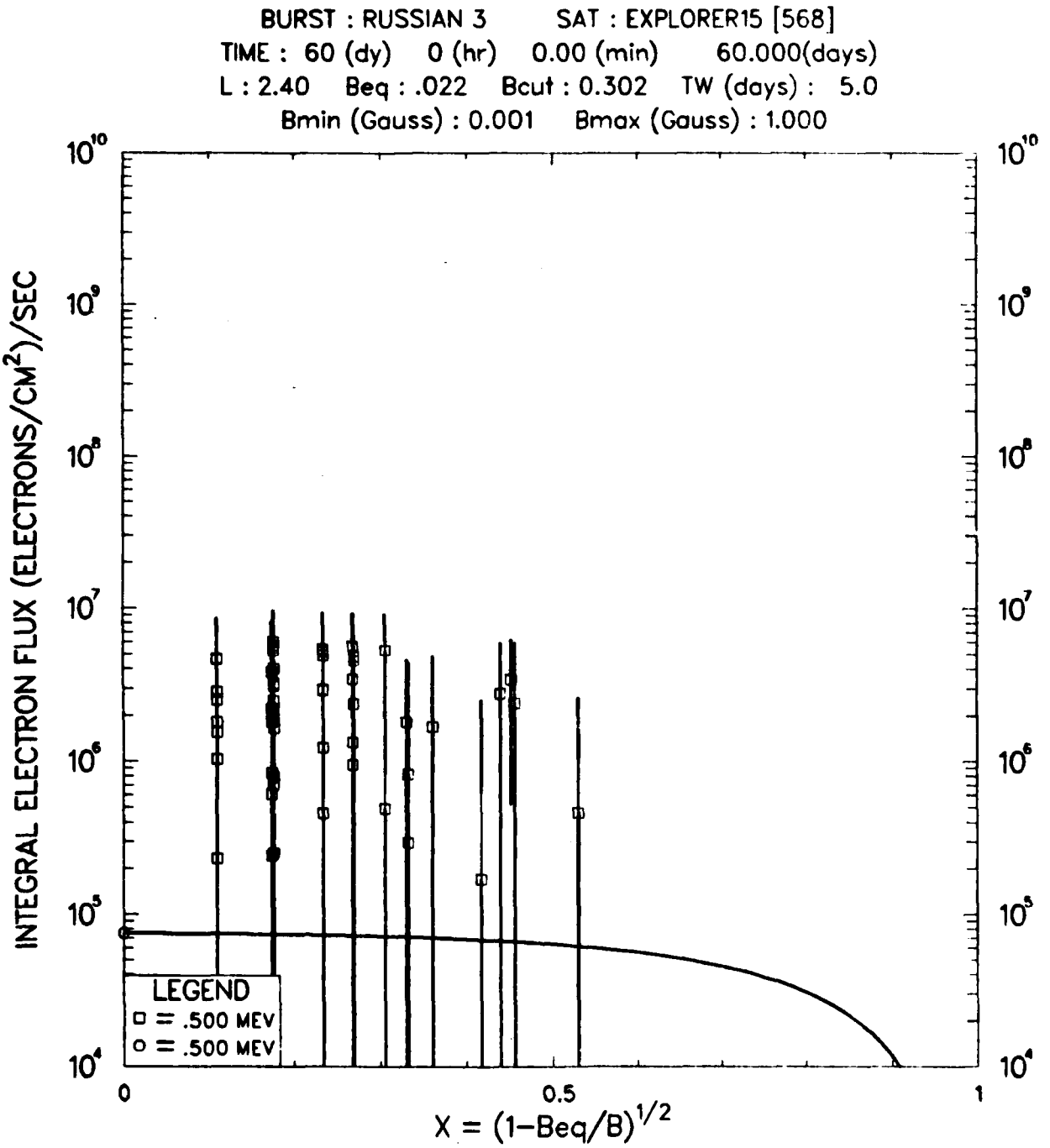

Figure 15(m). Temporal Progression of Raw Data and Fitted Flux Curves at $L = 2.4$ for Russian 3 Burst (r_o freely varying with physical contraints).

Table XVII

Fitted Linear Amplitude Coefficients and Exponential Decay Times at constant *L*-shell and Energy

Burst: Russian 2 Satellites: Allouette/Explorer 15/Telstar Run: [548]

L	E(MeV)	A_0	A_1	A_2	Tau_0	Tau_1	Tau_2	Y_{cut}	S.D.
1.80	3.900	1.1706E+05	-2.1859E+04	-1.2490E+04	12.00	1.333	0.48	0.4384	1.19E+05
		1.4831E+06	8.3226E+05	2.3031E+05	19.09	11.246	6.46	0.4276	1.18E+05
1.80	0.500	1.9632E+06	-2.0431E+06	4.2845E+06	275.00	30.556	11.00	0.4384	5.70E+07
		1.8626E+07	-7.6605E+06	5.6524E+06	421.90	127.058	91.43	0.4384	5.61E+07
1.80	1.900	4.4953E+05	-4.8884E+05	1.0500E+05	93.00	10.333	3.72	0.4384	8.12E+06
		4.7300E+05	-6.3683E+05	2.1687E+05	20.97	4.361	2.99	0.4686	8.00E+06
1.80	2.900	2.4246E+05	-3.1548E+05	1.5030E+05	42.00	4.667	1.68	0.4384	3.65E+06
		2.4078E+05	-2.8912E+05	2.5287E+05	18.16	8.153	2.47	0.5091	3.62E+06
1.80	0.420	2.8021E+06	-2.2720E+06	-9.1904E+05	271.00	30.111	10.84	0.4384	3.76E+07
		4.8350E+06	-3.0964E+06	-1.7284E+06	303.16	7.401	3.37	0.4384	3.73E+07
2.00	3.900	8.1788E+04	5.3848E+04	1.5400E+05	11.00	1.222	0.44	0.3693	1.43E+05
		8.5606E+06	4.5383E+06	1.2057E+06	4.66	3.884	2.31	0.3693	1.44E+05
2.00	3.910	4.0110E+04	-6.7985E+04	-2.2183E+04	10.90	1.211	0.44	0.3693	3.27E+05
		1.0113E+07	5.8122E+06	1.6545E+06	7.26	6.334	4.85	0.3693	3.27E+05
2.00	3.920	6.5738E+04	1.9126E+04	1.1436E+05	10.80	1.200	0.43	0.3693	1.61E+05
		8.8099E+06	5.2541E+06	1.6892E+06	5.01	3.993	2.59	0.3693	1.61E+05
2.00	0.500	2.6249E+06	-3.9188E+06	8.3740E+06	170.00	18.889	6.80	0.3693	4.31E+07
		1.8546E+07	-9.6075E+06	8.8303E+06	141.13	61.472	27.10	0.3693	4.31E+07
2.00	1.900	3.9940E+05	-6.2649E+05	7.4804E+05	32.00	3.556	1.28	0.3693	3.65E+06
		5.7150E+05	-6.7824E+05	3.7525E+05	5.03	3.136	2.58	0.4082	3.03E+06

(First line of pair is initial iteration: second line is result.)

(continued)

Table XVII (continued)

L	E(MeV)	A_0	A_1	A_2	Tau_0	Tau_1	Tau_2	Y_{cut}	S.D.
2.00	2.900	1.4976E+05	-1.9772E+05	1.6896E+05	21.00	2.333	0.84	0.3693	9.64E+05
		1.8532E+05	-1.6471E+05	5.9143E+04	6.17	3.922	2.88	0.4224	9.07E+05
2.00	0.220	9.9176E+06	-2.2910E+07	0.0000E+00	181.00	20.111	0.00	0.3693	1.23E+08
		1.0555E+07	-2.1520E+07	0.0000E+00	181.00	20.111	0.00	0.3226	1.21E+09
2.00	0.420	2.6218E+06	-9.3337E+06	0.0000E+00	182.00	20.222	0.00	0.3693	6.09E+07
		2.9026E+06	-8.8407E+06	0.0000E+00	182.00	20.222	0.00	0.3221	6.02E+08
2.20	3.900	8.7202E+04	5.6308E+04	7.0096E+04	18.00	2.000	0.72	0.3149	1.20E+04
		1.7603E+07	9.3106E+06	2.0912E+06	2.88	2.688	2.37	0.2937	1.05E+04
2.20	3.910	6.1391E+04	2.0451E+04	5.2578E+04	18.04	2.004	0.72	0.3149	8.47E+03
		3.9508E+06	1.8303E+06	3.3392E+05	4.40	3.826	2.60	0.3013	8.47E+03
2.20	3.920	7.0112E+04	3.0852E+04	7.2719E+04	18.08	2.009	0.72	0.3149	1.06E+04
		6.9407E+06	3.4812E+06	7.3471E+05	3.72	3.290	2.52	0.3007	1.02E+04
2.20	0.500	5.9769E+06	-6.8187E+06	8.3611E+06	38.00	4.222	1.52	0.3149	2.44E+07
		6.0411E+06	-6.2110E+06	6.3442E+06	22.75	5.053	3.19	0.3988	2.60E+07
2.20	1.900	7.7356E+05	-8.2268E+05	8.2759E+05	10.00	1.111	0.40	0.3149	2.56E+06
		1.0534E+06	-5.3080E+05	1.5162E+05	3.22	2.377	2.33	0.3921	1.74E+06
2.20	2.900	2.2282E+05	-2.0626E+05	9.7531E+04	14.00	1.556	0.56	0.3149	5.20E+05
		2.6539E+05	-1.6454E+05	3.1055E+04	5.01	2.593	2.34	0.3771	4.10E+05
2.20	0.220	6.1116E+06	-2.4959E+07	-2.2511E+06	60.00	6.667	2.40	0.3149	1.51E+08
		5.5814E+07	7.8556E+06	1.9033E+07	7.02	5.559	3.36	0.4013	1.36E+08
2.20	0.420	-5.7658E+06	-1.7488E+07	-6.4506E+06	47.60	5.289	1.90	0.3149	8.32E+07
		3.1618E+07	1.7626E+07	1.2355E+07	9.43	6.730	2.78	0.3149	7.64E+07
2.40	3.900	5.1282E+04	1.2427E+04	3.0982E+04	12.90	1.433	0.52	0.2716	3.05E+03
		2.2815E+06	1.2315E+06	2.9951E+05	3.70	3.135	2.38	0.2620	3.00E+03
2.40	3.910	6.0033E+04	2.4441E+03	1.9106E+04	12.94	1.438	0.52	0.2716	4.11E+03
		7.5281E+06	3.0865E+06	3.5984E+05	3.10	2.923	2.28	0.2604	3.80E+03
2.40	3.920	5.9525E+04	1.6058E+03	2.0097E+04	12.98	1.442	0.52	0.2716	4.06E+03
		1.6761E+06	7.8644E+05	1.5030E+05	3.80	3.289	2.37	0.2581	3.56E+03

(First line of pair is initial iteration; second line is result.)

(continued)

Table XVII (continued)

Burst: Russian 3 Satellites: Explorer 15 Run: [illegible]

L	E(MeV)	A_0	A_1	A_2	Tau_0	Tau_1	Tau_2	Y_{cut}	S.D.
2.20	0.500	2.2976E+06	-1.2529E+06	4.5277E+06	38.00	4.222	1.52	0.3149	1.60E+07
		2.8402E+06	-2.4271E+06	-7.2669E+04	14.47	1.754	0.92	0.3149	1.09E+07
2.20	1.900	3.7357E+05	-7.5561E+04	9.5917E+03	10.00	1.111	0.40	0.3149	8.05E+06
		2.7536E+05	2.1156E+04	1.7945E+05	33.02	5.710	3.08	0.3655	7.98E+06
2.20	2.900	1.2372E+05	-4.2136E+04	4.2516E+04	14.00	1.556	0.56	0.3149	2.50E+05
		1.9683E+05	-3.3109E+04	2.4729E+04	8.22	4.538	4.25	0.3149	1.47E+05

Run: [illegible]

2.40	0.500	1.1827E+06	2.1242E+05	3.3313E+06	30.00	3.333	1.20	0.2716	7.07E+06
		1.6624E+06	4.1216E+05	1.0906E+06	10.14	6.818	2.04	0.2716	4.72E+06
2.40	1.900	3.6172E+05	-4.0115E+04	-2.2962E+05	4.60	0.511	0.18	0.2716	1.07E+06
		3.5621E+05	-3.1494E+04	7.5426E+04	6.02	1.879	0.90	0.2716	1.02E+06
2.40	2.900	1.1311E+05	-1.7127E+04	2.2579E+04	8.90	0.989	0.36	0.2716	1.90E+05
		1.4319E+05	-1.1322E+04	1.9251E+04	7.38	5.695	3.30	0.2716	1.72E+05

(First line of pair is initial iteration; second line is result.)

The short time-spans covered by most of the data sets in the Trapped Electron Data Base have not allowed adequate determination of τ_0. The values of τ_0 presented in Table XVII are suspect for this reason. However, more confidence is held in the values of τ_1 and τ_2 computed by this study. In most data sets studied, the time period of the data was long enough compared to the values of τ_1 and τ_2 to compute reasonable values. More consistency between data sets was found for τ_1 and τ_2 than was found for τ_0. Of course, then τ_0 may be simply computed by multiplying τ_1 by the theoretical ratio corresponding to the solution.

VI. CONCLUSIONS AND RECOMMENDATIONS

Conclusions

The pitch-angle diffusion theory and flux calculation method developed in this study are reasonably consistent with experimental data in most cases. The method shows promise as a way of calculating improved decay times over a broad region of the magnetosphere, particularly for higher energy electrons. Additionally, a comprehensive summary table of the best available literature values for τ_0 has been prepared (Table XV). A complete table covering such a broad range of energy and L has not heretofore been compiled.

Time and computer limitations have precluded examination of the entire data base. However, the overall efficiency of the model developed in this study has been demonstrated. It is expected that improved predictions of fluxes and improved inputs to the AFWL SPECTER Codes (Ref. 7–9) will be available as a result of this work. This will enhance the capability for calculation of satellite operational environments, and will improve the ability to predict satellite survivability and vulnerability.

Recommendations

The following recommendations for further study are proposed to improve the model developed in this study, and to resolve the problem of non-physical solutions for some data sets. At the direction of this author, several of these recommendations are presently being implemented at the Air Force Weapons Laboratory.

(1) Incorporate an estimation of the error in the magnetic field value, B, of individual data points. This corresponds to a "horizontal" error bar on the plots such as Figure 12. It is known that errors exist in the computation of the B value associated with each data point, and this error would prove significant in the region of the loss cone. Improved weighting of the data points with the combined errors should improve the fit.

(2) Utilize the L-rounding procedure of Chapter IV to add data points to each L-value considered. This should aid in filling gaps in the data, which necessarily will improve the fit.

(3) Discard the highest eigenmode if the fitted value of its decay time is less that 0.25 day, and fit the data with only the fundamental and one higher mode. A value of 0.25 day is not reasonably fitted within the errors in the Trapped Electron Data Base. This mode would be essentially lost within the first day in any case.

(4) Perform an "energy-scaling" of the data to combine data from different satellites. This involves assuming some form of energy spectrum, such as $e^{-(E/E_0)}$, including an estimate of the error in the assumed value of E_0. The new flux would be simply the old flux multiplied by a factor $e^{-(E_{new}-E_{old})/E_0}$. If the error in the old flux were 50 percent (a value consistent with the Data Base) and the error in E_0 were 25 percent, and if $E_0 \approx 1.1$ (a fission spectrum), then the resultant error in the shifted flux would be less than 1 percent different from that of the old flux, when shifting from 660 KeV to 500 KeV. Thus, it should be possible to combine data sets and fill the gaps in data to achieve a better fit. However, the limitation of the assumed spectrum still exists.

(5) Utilize only late-time data where it is available, and fit only the fundamental mode to it, under the assumption that higher modes will have decayed away. Then, with the fundamental mode constrained, go back to early time data and attempt to fit higher modes, if any. This recommendation is of limited value because only two data sets cover a significant period of time: Starfish/Telstar and Russian 3/Explorer 5. However, it may provide a better value of r_0 than is presently available at some L values.

(6) Revise the fitting functions to other Bessel function solutions than the $J_{-1/2}$ solution and compare results. This was performed only on one other functional solution, J_0, with only one small data set, and the results showed no improvement over the present study. However, to be certain that the author has not simply chosen the wrong functional form, more functional forms must be investigated.

(7) In the fitting program, constrain the directional flux to physical reality at each iteration (i.e., compute flux at each iteration and reject non-physical solutions at each iteration, rather than after converging on a final solution). This should converge to a physically real solution if it converges at all; however, significant increases in computer processing time may accrue.

(8) Increase the number of tries for a solution from 96 to 200 and reduce the number of outer loops from 32 to 10 or 15. This may improve the convergence of the least squares error, if non-physical solutions are also rejected at each iteration.

(9) Compare the background subtracted from the flux with the latest available natural environment, to ascertain the correctness of the background subtraction. If significant differences are found, the background should be re-added to the flux and the natural environment subtracted.

(10) A suggestion proposed by Professor D.G. Shankland, Air Force Institute of Technology, involves a significant modification to the fitting method. This method involves an interpolating function, or measure of "roughness" of the fit, which may be made arbitrarily smooth. The advantage of this method is that no limiting assumptions need be made about the data. The chief disadvantage is that the method is a strictly mathematical method, with no physical constraints. Although the method would involve extensive reprogramming, it promises worthwhile information about the flux curves, and should be tried.

BIBLIOGRAPHY

1. Abramowicz, M. and I.A. Stegun (editors). *Handbook of Mathematical Functions*, U.S. Department of Commerce, Applied Mathematics Series 55, Washington, D.C., 1966.

2. Baker, D.N., et. al., "High-Energy Magnetospheric Protons and Their Dependence on Geomagnetic and Interplanetary Conditions," *Journal of Geophysical Research* 84:7838 (1979).

3. Chan, K.W., et. al., "Modelling of Electron Time Variations in the Radiation Belts," *Quantitative Modeling of Magnetospheric Processes*, Geophysical Monograph 21:121–149, W.P. Olson, ed., American Geophysical Union, Washington, D.C., 1979.

4. Cladis, J.B., et. al., *Search for Possible Loss Processes for Geomagnetically Trapped Particles*, DASA 1713, Headquarters, Defense Nuclear Agency, Washington, D.C., December 1965. (AD 477489)

5. Cladis, J.B., et. al., *Trapped Radiation and Magnetospheric Processes*, DASA 2646, Headquarters, Defense Nuclear Agency, Washington, D.C., March 1971. (AD 882756)

6. Cladis, J.B., et. al., (editors), *The Trapped Radiation Handbook*, DNA 2524 H Revision 2, Headquarters, Defense Nuclear Agency, Washington, D.C., November 1973. (AD 738841)

7. Cladis, J.B., et. al., *Improvement of Spector II Code*, AFWL-TR-75-286, Air Force Weapons Laboratory, Kirtland AFB, New Mexico, September 1976.

8. Cladis, J.B., et. al., *Improvement of Specter II Code, Injection and Evolution of An Artificial Radiation Belt*, AFWL-TR-78-236, Air Force Weapons Laboratory, Kirtland AFB, New Mexico, August 1979.

9. Cladis, J.B., et. al., *Improvement of Specter II Codes, Models of Geomagnetic Field, Fission Products Decay, Debris Tube Dynamics, and Evolution of Trapped Electron Distribution*, AFWL-TR-80-117, Vol. I, Air Force Weapons Laboratory, Kirtland AFB, New Mexico, July 1981.

10. Davidson, G.T., "An Improved Empirical Description of the Bounce Motion of Trapped Particles," *Journal of Geophysical Research* 81:4029–4030 (1976).

11. Hess, W.N., *The Radiation Belt and Magnetosphere*, Blaisdell Publishing Co., Waltham, Massachusetts, 1968.

12. Hess. W.N., "The Artificial Radiation Belt Made on July 9, 1962," *Journal of Geophysical Research* 68:667–683 (1963).

13. Higbie, P.R., et. al., "High Resolution Energetic Particle Measurement at 6.6 R_E," *Journal of Geophysical Research* 83:4851 (1978).

14. Imhof, W.L., et. al., "Long-Term Study of Electrons Trapped on Low L Shells," *Journal of Geophysical Research* 72:2371 (1967).

15. Jarrett, C., Programmer, Computer Sciences Corporation, "Program DTABASE," unpublished FORTRAN computer program, Air Force Weapons Laboratory, Kirtland AFB, New Mexico, November 1982.

16. Jensen, D.C. and J.C. Cain, "An Interim Magnetic Field," *Journal of Geophysical Research* **67**:3568–3569 (1962).

17. Kuck, G.A., *Pitch-Angle Diffusion of Relativistic Electrons in the Plasmasphere*, AFWL-TR-73-116, Air Force Weapons Laboratory, Kirtland AFB, New Mexico, June 1973. (AD 762-952)

18. Kivelson, M.G., et. al., "Satellite Studies of Magnetospheric Substorms on August 15, 1968," *Journal of Geophysical Research* **78**:3079 (1973).

19. Lanzerotti, L.J. and A. Wolfe, "Particle Diffusion in the Geomagnetosphere: Comparison of Estimates from Measurements of Magnetic and Electric Field Fluctuations," *Journal of Geophysical Research* **85**:2346 (1980).

20. Lyons, L.R., "A Theory for Energetic Electron Lifetimes within the Plasmasphere," in Folkestad, Kristen, *Magnetosphere-Ionosphere Interactions*, 57–61, Universitetsforlaget, Oslo, 1971.

21. Lyons, L.R., R.M. Thorne and C.F. Kennel, "Electron Pitch-Angle Diffusion Driven By Oblique Whistler-Mode Turbulence," *Journal of Plasma Physics* **6**:589–606 (1971).

22. Lyons, L.R., R.M. Thorne and C.F. Kennel, "Pitch-Angle Diffusion of Radiation Belt Electrons within the Plasmasphere," *Journal of Geophysical Research* **77**:3455–3474 (1972).

23. Lyons, L.R., and R.M. Thorne, "Parasitic Pitch Angle Diffusion of Radiation Belt Particles by Ion Cyclotron Waves," *Journal of Geophysical Research* **77**:5608–5616 (1972).

24. Lyons, L.R., and R.M. Thorne, "Equilibriun Structure of Radiation Belt Electrons," *Journal of Geophysical Research* **78**:2142–2149 (1973).

25. Lyons, L.R., "Comments on Pitch Angle Diffusion in the Radiation Belts," *Journal of Geophysical Research* **78**:6793–6797 (1973).

26. Lyons, L.R., "General Relations for Resonant Particle Diffusion in Pitch Angle and Energy," *Journal of Plasma Physics* **12**:45–49 (1974).

27. Lyons, L.R., "Electron Diffusion Driven by Magnetospheric Electrostatic Waves," *Journal of Geophysical Research* **79**:575–580 (1974).

28. Lyons, L.R., "Pitch Angle and Energy Diffusion Coefficients from Resonant Interactions with Ion-Cyclotron and Whistler Waves," *Journal of Plasma Physics* **12**:417–432 (1974).

29. Mihalov, J.D., "Energetic Trapped Electron Observations During the Fall of 1964," *Journal of Geophysical Research* **72**:1081–1094 (1967).

30. MacDonald, W.M. and M. Walt, "Distribution Function of Magnetically Confined Electrons in a Scattering Atmosphere," *Annals of Physics* **15**:44–62 (1961).

31. Moser, F.S., et. al., "Preliminary Analysis of the Fluxes and Spectrums of Trapped Particles after the Nuclear Test of July 9, 1962," *Journal of Geophysical Research* **68**:641–649 (1963).

32. McCormac, B.M. (Editor), *Radiation Trapped in the Earth's Magnetic Field*, Reidel Publishing Co., Dordrecht, Holland, 1966.

33. McLachlan, N.W., *Bessel Functions for Engineers*, Oxford University Press, London, 1955.

34. Murphy, Harry, "Program Electrofit," unpublished FORTRAN computer program. Air Force Weapons Laboratory, Kirtland AFB, New Mexico, December 1982.

35. Palmer, I.D. and P.R. Higbie, "Magnetosheath Distortion of Pitch Angle Distributions of Solar Protons," *Journal of Geophysical Research* **83**:30 (1978).

36. Pfitzer, K.A., *An Experimental Study of Electron Fluxes from 50 KeV to 4 MeV in the Inner Radiation Belt*, TR-CR-123, School of Physics and Astronomy, University of Minnesota, Minneapolis, Minnesota, August 1968.

37. Pfitzer, K.A., *Summary of Trapped Electron Data*, AFWL-TR-81-223, Air Force Weapons Laboratory, Kirtland AFB, New Mexico, October 1982.

38. Pieper, G.F. and D.J. Williams, "Traac Observations of the Artificial Radiation Belt from the July 9, 1962 Nuclear Detonation," *Journal of Geophysical Research* **68**:635–640 (1963).

39. Roederer, J.G., *Dynamics of Geomagnetically Trapped Radiation*, Springer–Verlag, Berlin, 1970.

40. Roberts, C.S., "On the Relationship Between the Unidirectional and Omnidirectional Flux of Trapped Particles on a Magnetic Line of Force," *Journal of Geophysical Research* **70**:2517–2527 (1965).

41. Roberts, C.S., "Pitch-Angle Diffusion of Electrons in the Magnetosphere," *Reviews of Geophysics* **7**:305–337 (1969).

42. Rossi, B. and S. Olbert, *Introduction to the Physics of Space*, McGraw-Hill, New York, 1970.

43. Rosen, A. and N.L. Sanders, "Loss and Replenishment of Electrons in the Inner Radiation Zone During 1965–1967," *Journal of Geophysical Research* **76**:110–121 (1971).

44. Scott, Edie (Editor), *TRW Space Log*, Redondo Beach, California, TRW Systems Group, TRW Inc., One Space Park, Redondo Beach, California 90278 (1970).

45. Shuls, M. and L.J. Lanzerotti, *Particle Diffusion in the Radiation Belts*, Springer-Verlag, New York-Heidelberg-Berlin, 1974.

46. Shuls, M., "Relation Between Bounce-Averaged Collisional Transport Coefficients for Geomagnetically Trapped Electrons," *Journal of Geophysical Research* **81**:5212-13 (1976).

47. Shuls, M., "Pitch-Angle Diffusion in Canonical Coordinates: A Theoretical Formulation," SD-TR-81-69, The Aerospace Corporation, El Segundo, California, 21 August 1981.

48. Shulz, M. and D.J. Boucher, "Pitch-Angle Diffusion in Canonical Coordinates: Some Numerical Results," The Aerospace Corporationn, El Segundo, California, October 1979, presented at 1979 Fall Meeting of American Geophysical Union, San Francisco, California, 3 December 1979.

49. Smith, R.V. and W.L. Imhof, "Satellite Measurements of the Artificial Radiation Belt," *Journal of Geophysical Research* **68**:629–633 (1963).

50. Stassinopoulos, E.G. and P. Verzariu, "General Formula for Decay Lifetimes of Starfish Electrons," *Journal of Geophysical Research* **76**:1841–1844 (1971).

51. Swider, W., et. al., "Electron Loss During a Nighttime PCA Event," *Journal of Geophysical Research* **76**:4691 (1971).

52. Swider, W. and W.A. Dean, "Effective Electron Loss Coefficient of the Disturbed Daytime D-Region," *Journal of Geophysical Research* **80**:1815 (1975).

53. Teague, M.J. and E.G. Stassinopoulos, *A Model of the Starfish Flux in the Inner Radiation Zone*," X-601-72-487, National Space Science Data Center, NASA Goddard Space Flight Center, Greenbelt, Maryland, December 1972.

54. Tomassian, A.D., T.A. Farley and A.L. Vampola, "Inner-Zone Energetic-Electron Repopulation by Radial Diffusion," *Journal of Geophysical Research* **77**:3441–3454 (1972).

55. Tranter, C.J., *Bessel Functions with Some Physical Applications*, Hart Publishing Company, New York, 1968.

56. Walt, M. and W.M. MacDonald, "Diffusion of Electrons in the Van Allen Radiation Belt," *Journal of Geophysical Research*, **67**:5013–5033 (1962).

57. Walt, M. and W.M. MacDonald, "The Influence of the Earth's Atmosphere on Geomagnetically Trapped Particles," *Reviews of Geophysics*, **2**:543–577 (1964).

58. Walt, M., "Radial Diffusion of Trapped Particles and Some of Its Consequences," *Reviews of Geophysics and Space Physics* **9**:11–25 (1971).

59. Welch, J.A., et. al., "Trapped Electron Time Histories for L = 1.18 to L = 1.30," *Journal of Geophysical Research* **68**:685–699 (1963).

60. Wentworth, R.C., *Lifetimes of Geomagnetically Trapped Particles Determined by Coulomb Scattering*, AFOSR TN-60-288, Physics Department, University of Maryland, College Park, Maryland.

61. West, H.I., R.M. Buck and J.R. Walton, "Electron Pitch Angle Distributions Throughout the Magnetosphere as Observed on Ogo 5," *Journal of Geophysical Research* 78:1064 (1973).

62. West, H.I., et. al., "Ogo 5 Energetic Electron Observations—Pitch Angle Distributions in the Nighttime Magnetosphere," *Journal of Geophysical Research* 78:3093 (1973).

63. West, H.I., et. al., *Study of Energetic Electrons in the Outer Radiation-Belt Regions Using Data Obtained by the LLL Spectrometer in OGO-5 in 1968*, UCRL-52807, Lawrence Livermore Laboratory, Livermore, California, July 26, 1979.

64. Williams, D.J., et. al., "Observations of Trapped Electrons at Low and High Altitudes," *Journal of Geophysical Research*, 73:5673-5696 (1968).

65. Zmuda, A.J., et. al., "Very Low Frequency Disturbances and the High-Altitude Nuclear Explosion of July 9, 1962," *Journal of Geophysical Research*, 68:745 (1963).

APPENDIX A

Demonstration of Zero Diffusion Current at the Magnetic Equator for Half-Integer Bessel Function Solution

To demonstrate zero diffusion current, one must show that

$$\lim_{z \to 0} D_{zz}\, \mathcal{J}_n'(z) = 0$$

for the $\sigma = 0$ case. We Know that from (31):

$$J_{-1/2}(z) = \sqrt{2/(\pi z)}\ \cos(z)$$

and from (16):

$$D_{zz} = D_{zz_e}$$

and from (18):

$$\mathcal{J}_n(z) = \frac{\sqrt{2/z_e}}{J'(\kappa_n)}\ \sqrt{z/z_e}\ \sqrt{\frac{2}{\pi(2n+1)(\pi/2)(z/z_e)}}\ \cos\left((2n+1)\,\frac{\pi}{2}\,\frac{z}{z_e}\right)$$

$$= \left[\frac{\sqrt{2/z_e}\,\sqrt{4/(\pi^2(2n+1))}}{J'(\kappa_n)}\right] \cos\left((2n+1)\,\frac{\pi}{2}\,\frac{z}{z_e}\right).$$

Hence, the derivative of the eigenfunction:

$$\mathcal{J}_n'(z) = -\left[\frac{\sqrt{2/z_e}\sqrt{4/(\pi^2(2n+1))}}{J'(\kappa_n)}\right]\left[(2n+1)\frac{\pi}{2z_e}\right] \sin\left((2n+1)\,\frac{\pi}{2}\,\frac{z}{z_e}\right).$$

Finally, the quantity which must go to zero is:

$$D_{zz}\mathcal{J}_n' = -\left[\frac{D_{zz_e}\,\sqrt{2/z_e}\,\sqrt{4/(\pi^2(2n+1))}\,((2n+1)\,\pi/(2z_e))}{J'(\kappa_n)}\right] \sin\left((2n+1)\frac{\pi}{2}\,\frac{z}{z_e}\right)$$

The term in square brackets is a finite constant for any n, and clearly the sine goes to zero as z goes to zero. Hence, the limit is zero.

APPENDIX B

Derivation of Eigenfunction Derivatives $\bar{f}'_\infty$ and $\bar{g}'_n$

To find the derivative of the steady state function, $\bar{f}_\infty$, one starts with (21):

$$\bar{f}_\infty = \sum_{n=0}^{\infty} \frac{\bar{g}_n}{\lambda_n} \int_0^{z_c} \bar{S}(z')\, \bar{g}_n(z')\, d(z')$$

If the λ_n are assumed (from (19)) independent of z, then the series can simply be differentiated term-by-term, since the definite integral is simply a constant for each value of n.

$$\bar{f}'_\infty(z) = \frac{d}{dz}\left[\sum_{n=0}^{\infty} \frac{g_n(z)}{\lambda_n} \int_0^{z_c} \bar{S}\, \bar{g}_n(z')\, d(z')\right]$$

$$= \sum_{n=0}^{\infty} \frac{\bar{g}'_n(z)}{\lambda_n} \int_0^{z_c} \bar{S}\, \bar{g}_n(z')\, d(z').$$

To find the derivative of the eigenfunction $\bar{g}_n$, one starts with (18):

$$\bar{g}_n(z) = \frac{\sqrt{(2-\sigma)/z_c}}{J'_\nu(\kappa_{\nu n})} \left(\frac{z}{z_c}\right)^{(1-\sigma)/2} J_\nu\left(\kappa_{\nu n}\left(\frac{z}{z_c}\right)^{(1-(\sigma/2))}\right)$$

Using the product rule for differentiation:

$$\bar{g}'_n = \frac{d}{dz}(\bar{g}_n(z))$$

$$= \left[\frac{\sqrt{(2-\sigma)/z_c}}{J'_\nu(\kappa_{\nu n})}\right]\left\{\left(\frac{1-\sigma}{2}\right)\left(\frac{1}{z_c}\right)\left(\frac{z}{z_c}\right)^{-(\sigma+1)/2} J_\nu\left(\kappa_{\nu n}\left(\frac{z}{z_c}\right)^{(1-(\sigma/2))}\right)\right.$$

$$\left. + \left(\frac{z}{z_c}\right)^{(1-\sigma)/2} J'_\nu\left(\kappa_{\nu n}\left(\frac{z}{z_c}\right)^{(1-(\sigma/2))}\right)\left[\frac{\kappa_{\nu n}}{z_c}\left(1-\frac{\sigma}{2}\right)\left(\frac{z}{z_c}\right)^{-\sigma/2}\right]\right\}$$

APPENDIX C

The Specific Solution of the Integral-Energy Omnidirectional Flux Equation for the Half-Integer Bessel Function Solution

The integral-energy omnidirectional flux Equation (43), which is the energy-integrated form of Equation (37), is represented as the steady state term, f_∞, plus the sum of exponentially decaying eigenmodes f_0 through f_3:

$$J_{>E}\left(y = \sqrt{B_0/B}\right) = f_\infty + f_0 + f_1 + f_2 + f_3$$

In this appendix, each term is shown, as derived from Equations (37) and (43). Note that the eigenmode sum should be infinite, but only the fundamental mode and three higher modes are shown.

The constants in each term are defined as follows (Ref. 39:55):

$$y_c = \sqrt{1/\left(L^3\sqrt{4-(3/L)}\right)}$$

$$T_0 = 1 + \left\{\left(\ln\left[2+\sqrt{3}\right]\right)/\left(2\sqrt{3}\right)\right\} \approx 1.3801730$$

$$T_1 = \left(\pi\sqrt{2}\right)/6 \approx 0.7404805$$

$$K = (4/11)[T_0 - T_1] \approx 0.2326155$$

$$Z_c = T_0(1-y_c^2) - K\left(1-y_c^{11/4}\right)$$

The "fitting constants" are defined as in Equation (43) or in Appendix D:

$$S = \int_E^\infty p^2 f_{\infty_1}(E)\,dE$$

$$a_n = \int_E^\infty p^2 a_n(E)\,dE$$

$$f_\infty = 2\pi S \int_{y=y_c}^{y=\sqrt{(B_c/B)}} \frac{\left[(4/Z_c)(\pi/Z_c)\left[\sqrt{1-y^2(B/B_0)}\right]\left[T_0-(T_0-T_1)y^{3/4}\right]y\right]}{(\pi/2Z_c)^2}$$

$$\left\{\left(\frac{\sin\left[(\pi/2Z_c)\left(\left[(1-y^2)T_0\right]/2 - K\left(1-y^{11/4}\right)\right)\right]}{1}\right)\right.$$

$$-\frac{\left(\sin\left[(3\pi/2Z_c)\left(\left((1-y^2)T_0\right)/2 - K\left(1-y^{11/4}\right)\right)\right]\right)}{9}$$

$$\left.+\frac{\left(\sin\left[(5\pi/2Z_c)\left(\left((1-y^2)T_0\right)/2 - K\left(1-y^{11/4}\right)\right)\right]\right)}{25}\right.$$

$$\left.\frac{\left(\sin\left[(7\pi/2Z_e)(((1-y^2)T_0)/2 - K\left(1-y^{11/4}\right))\right]\right)}{49}\right\} dy$$

$$f_0 = -2\pi a_0 e^{-(t/\tau_0)} \int_{y=y_e}^{y=\sqrt{B_e/B}} \left[\sqrt{2/Z_e}(\pi/Z_e)\left[\sqrt{1-y^2(B/B_0)}\right]\left[T_0 - (T_0 - T_1)y^{3/4}\right]y\right] \left(\sin\left[(\pi/(2Z_e))\left(((1-y^2)T_0)/2 - K\left(1-y^{11/4}\right)\right)\right]\right) dy$$

$$f_1 = +2\pi a_\pi e^{-(t/\tau_1)} \int_{y=y_e}^{y=\sqrt{B_e/B}} \left[\sqrt{2/Z_e}(3\pi/Z_e)\left[\sqrt{1-y^2(B/B_0)}\right]\left[T_0 - (T_0 - T_1)y^{3/4}\right]y\right] \left(\sin\left[(3\pi/(2Z_e))\left(((1-y^2)T_0)/2 - K\left(1-y^{11/4}\right)\right)\right]\right) dy$$

$$f_2 = -2\pi a_2 e^{-(t/\tau_2)} \int_{y=y_e}^{y=\sqrt{B_e/B}} \left[\sqrt{2/Z_e}(5\pi/Z_e)\left[\sqrt{1-y^2(B/B_0)}\right]\left[T_0 - (T_0 - T_1)y^{3/4}\right]y\right] \left(\sin\left[(5\pi/(2Z_e))\left(((1-y^2)T_0)/2 - K\left(1-y^{11/4}\right)\right)\right]\right) dy$$

$$f_3 = +2\pi a_3 e^{-(t/\tau_3)} \int_{y=y_e}^{y=\sqrt{B_e/B}} \left[\sqrt{2/Z_e}(7\pi/Z_e)\left[\sqrt{1-y^2(B/B_0)}\right]\left[T_0 - (T_0 - T_1)y^{3/4}\right]y\right] \left(\sin\left[(7\pi/(2Z_e))\left(((1-y^2)T_0)/2 - K\left(1-y^{11/4}\right)\right)\right]\right) dy$$

These fitting constants are really fuctions of energy and L-shell.

The ratios of τ_0, τ_1, τ_2, and τ_3 should be (as computed from the eigen value ratio of the zeroes of the function):

$\tau_0 \approx 9\tau_1$		$\tau_1 = (1/9)\tau_0$
$\tau_0 \approx 25\tau_2$	or alternatively	$\tau_2 = (1/25)\tau_0$
$\tau_0 \approx 49\tau_3$		$\tau_3 = (1/49)\tau_0$

APPENDIX D

The General Solution of the Integral-Energy Omnidirectional Flux Equation for Bessel Functions of Arbitrary Order, as a Function of Sigma

Substitution of (18), (28), and (29) into (27) completes the general expression for the differential energy omnidirectional flux, J, with Bessel functions of order

$$\nu = \frac{\sigma - 1}{2 - \sigma}$$

where σ is some number less than two:

$$J = 2\pi p^2 \left\{ \left(-\int_{y_c^2}^{(B_0/B)} \sum_{n=0}^{\infty} \frac{\bar{S}}{\bar{\lambda}_n} \int_{z'=0}^{z'=z_c} \frac{\sqrt{(2-\sigma)/z_c}}{J'_\nu(\kappa_{\nu n})} \left(\frac{z'}{z_c}\right)^{(1-\sigma)/2} J_\nu\left(\kappa_{\nu n}\left(\frac{z'}{z_c}\right)^{1-(\sigma/2)}\right) dz' \right.\right.$$

$$\bullet \frac{\sqrt{(2-\sigma)/z_c}}{J'_\nu(\kappa_{\nu n})} \left[\left(\frac{1-\sigma}{2z_c}\right)\left(\frac{z}{z_c}\right)^{-(\sigma+1)/2} J_\nu\left(\kappa_{\nu n}\left(\frac{z}{z_c}\right)^{1-(\sigma/2)}\right) \right.$$

$$\left. + \left(\frac{z}{z_c}\right)^{(1-\sigma)/2} J'_\nu\left(\kappa_{\nu n}\left(\frac{z}{z_c}\right)^{1-(\sigma/2)}\right)\left(\frac{\kappa_{\nu n}}{z_c}\left(1-\frac{\sigma}{2}\right)\left(\frac{z}{z_c}\right)^{-(\sigma/2)}\right)\right]$$

$$\left. \bullet \sqrt{1 - y^2(B/B_0)}\ T(y)\, d(y^2) \right)$$

$$- \left(\sum_{n=0}^{\infty} \Lambda_n(E, L; t) \int_{y_c^2}^{(B_0/B)} \frac{\sqrt{(2-\sigma)/z_c}}{J'_\nu(\kappa_{\nu n})} \right.$$

$$\bullet \left[\left(\frac{1-\sigma}{2z_c}\right)\left(\frac{z}{z_c}\right)^{-(\sigma+1)/2} J_\nu\left(\kappa_{\nu n}\left(\frac{z}{z_c}\right)^{1-(\sigma/2)}\right) \right.$$

$$\left. + \left(\frac{z}{z_c}\right)^{(1-\sigma)/2} J'_\nu\left(\kappa_{\nu n}\left(\frac{z}{z_c}\right)^{1-(\sigma/2)}\right)\left(\frac{\kappa_{\nu n}}{z_c}\left(1-\frac{\sigma}{2}\right)\left(\frac{z}{z_c}\right)^{-(\sigma/2)}\right)\right]$$

$$\left. \left. \bullet \sqrt{1 - y^2(B/B_0)}\ T(y)\, d(y^2) \right) \right\}$$

The analogy between the above equation and Equation (43) is seen if:

$$\left[\int_E^{\infty} p^2 \bar{J}_{\infty_1}(E)\, dE \right]_L = \int_E^{\infty} p^2 \bar{S}/\bar{D}_{zz_c}\, dE$$

and if:

$$\left[\int_E^{\infty} p^2 a_n(E) \right]_L \langle c - t/(\tau_n) \rangle_L = \int_E^{\infty} p^2\, dE\, \Lambda_{n_L}(E)$$

$$= \int_E^{\infty} p^2\, a_n(E) e^{-t/(\tau_n(E))}\, dE$$

Hence, (43) is simply the energy-integrated form of (37).

APPENDIX E

Flow Chart for Program Electrofit

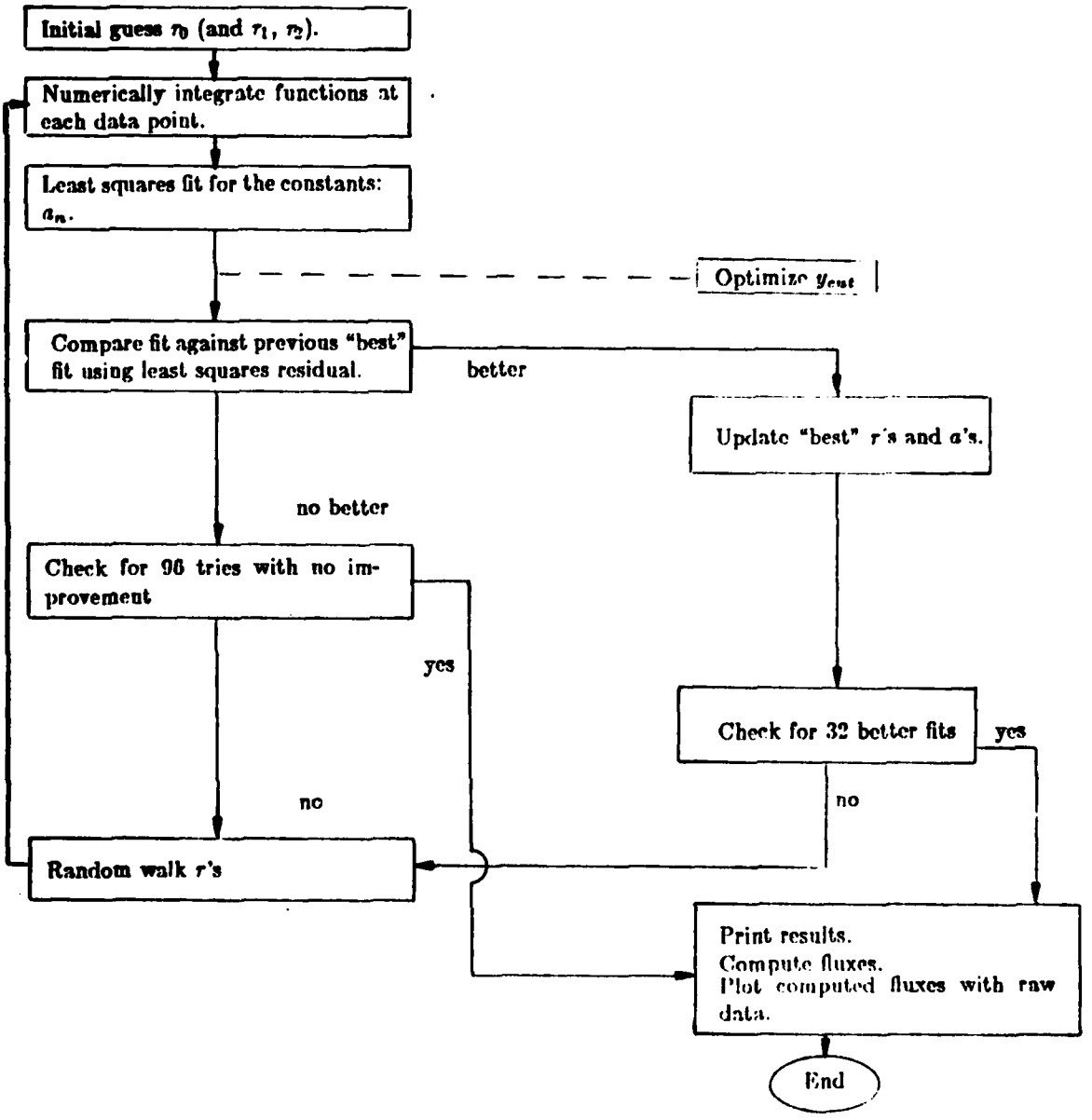

VITA

Roger Scott Dewey was born on August 15, 1947 in Akron, Ohio. He graduated from Tallmadge High School, Tallmadge, Ohio, in 1965 and attended Brown University, from which he received the Degree of Bachelor of Science in Chemistry in January 1970. Upon graduation, he received a commission in the USN through the NROTC program. He completed flight training and received his wings in April 1971. He has served as an SH-3 pilot and flight instructor in Helicopter Antisubmarine Squadrons at Naval Air Stations Quonset Point, Rhode Island and Jacksonville, Florida. He served as Assistant Air Operations Officer and UH-1N pilot aboard the USS Guadalcanal, LPH-7, out of Norfolk, Virginia, until entering the School of Engineering, Air Force Institute of Technology in August 1981.

Permanent Address:

c/o Robert A. Dewey
RD 1
Bemus Point, New York 14712

UNCLASSIFIED

SECURITY CLASSIFICATION OF THIS PAGE (When Data Entered)

REPORT DOCUMENTATION PAGE	READ INSTRUCTIONS BEFORE COMPLETING FORM
1. REPORT NUMBER: AFIT/GNE/PH/83M-4	2. GOVT ACCESSION NO.: AD-A127324
3. RECIPIENT'S CATALOG NUMBER:	
4. TITLE (and Subtitle): ELECTRON LOSSES FROM THE MAGNETOSPHERE	5. TYPE OF REPORT & PERIOD COVERED: MS Thesis
	6. PERFORMING ORG. REPORT NUMBER:
7. AUTHOR(s): Roger S. Dewey, LCDR USN	8. CONTRACT OR GRANT NUMBER(s):
9. PERFORMING ORGANIZATION NAME AND ADDRESS: Air Force Institute of Technology(AFIT-EN) Wright-Patterson AFB, Ohio 45433	10. PROGRAM ELEMENT, PROJECT, TASK AREA & WORK UNIT NUMBERS: 88091901
11. CONTROLLING OFFICE NAME AND ADDRESS: Air Force Weapons Laboratory(AFWL/NTCTS) Kirtland AFB, N.M. 87117	12. REPORT DATE: March, 1983
	13. NUMBER OF PAGES: 134
14. MONITORING AGENCY NAME & ADDRESS(if different from Controlling Office)	15. SECURITY CLASS. (of this report): Unclassified
	15a. DECLASSIFICATION DOWNGRADING SCHEDULE

16. DISTRIBUTION STATEMENT (of this Report)

Approved for Public Release; distribution unlimited

17. DISTRIBUTION STATEMENT (of the abstract entered in Block 20, if different from Report)

Approved for public release; IAW AFR 190-17

18. SUPPLEMENTARY NOTES

Approved for public release: IAW AFR 190-17.

LYNN E. WOLAVER
Dean for Research and Professional Development
Air Force Institute of Technology (ATC)
Wright-Patterson AFB OH 45433

7 APR 1983

19. KEY WORDS (Continue on reverse side if necessary and identify by block number)

electron flux
magnetosphere
pitch-angle diffusion
trapped radiation
electron loss time
electron decay time

20. ABSTRACT (Continue on reverse side if necessary and identify by block number)

A semi-empirical method for modelling loss of electron fluxes in the earth's magnetosphere was developed. An equation for integral-energy omnidirectional electron flux as a function of time and magnetic field strength was derived from pitch-angle diffusion theory. The flux equation was the basis for a computer data-fitting program written at the Air Force Weapons Laboratory(AFWL) to fit the AFWL Trapped Electron Data Base. The program utilized a least-squares fit and incorporated random

DD FORM 1 JAN 73 1473 EDITION OF 1 NOV 65 IS OBSOLETE

UNCLASSIFIED

SECURITY CLASSIFICATION OF THIS PAGE (When Data Entered)

variations of the characteristic exponential loss times about their initial values. An improved table of initial loss times was compiled for use with the program. The derived flux model showed substantial agreement with the empirical data base.

Representative plots of computed flux over raw data are shown for L-values of 2.3 and 2.4.


FILM